

PHYSICAL AND QUANTITATIVE INTERPRETATION OF
SEISMIC ATTRIBUTES FOR ROCKS AND FLUIDS
IDENTIFICATION

A DISSERTATION

SUBMITTED TO THE DEPARTMENT OF GEOPHYSICS

AND THE COMMITTEE ON GRADUATE STUDIES

OF STANFORD UNIVERSITY

IN PARTIAL FULFILLMENT OF THE REQUIREMENTS

FOR THE DEGREE OF

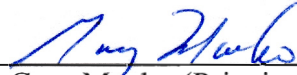
DOCTOR OF PHILOSOPHY

Ezequiel F. González

June 2006

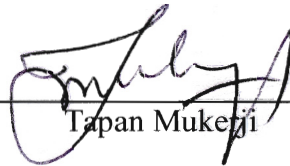
© Copyright by Ezequiel F. González 2006
All Rights Reserved

I certify that I have read this dissertation and that, in my opinion, it is fully adequate in scope of and quality as a dissertation for the degree of Doctor of Philosophy.



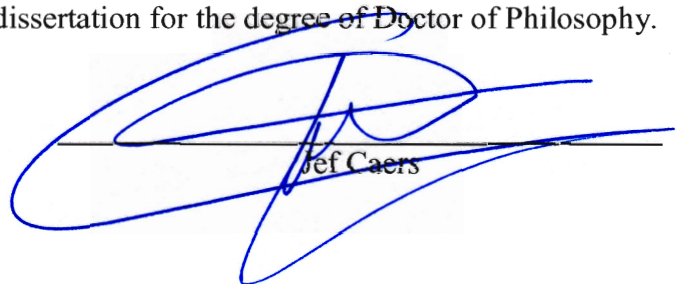
Gary Mavko (Principal Adviser)

I certify that I have read this dissertation and that, in my opinion, it is fully adequate in scope of and quality as a dissertation for the degree of Doctor of Philosophy.



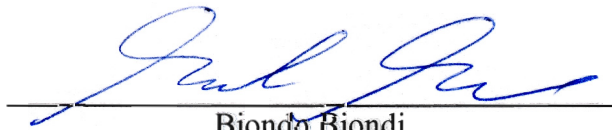
Tapan Mukerji

I certify that I have read this dissertation and that, in my opinion, it is fully adequate in scope of and quality as a dissertation for the degree of Doctor of Philosophy.



Jef Caers

I certify that I have read this dissertation and that, in my opinion, it is fully adequate in scope of and quality as a dissertation for the degree of Doctor of Philosophy.



Biondo Biondi

Approved for the University Committee on Graduate Studies.

Abstract

This dissertation focuses on the link between seismic attributes and reservoir properties like lithology, porosity, and pore-fluid saturation. *The key contribution of this dissertation is a novel inversion technique, which combines rock physics and multiple-point geostatistics.* The inversion of seismic data is only one particular application of the technique.

In general, seismic attributes are all the information that can be obtained from seismic data. Using statistical rock-physics, the type of seismic attributes that are direct functions (analytically defined) of the elastic properties, can be probabilistically transformed sample-by-sample, independently one of each other, into reservoir properties. For these *wavelet-independent* seismic attributes, the wavelet or scale effects are removed during calculation; hence, they can be interpreted as the response from a well-localized reservoir zone.

In contrast, wavelet-dependent seismic attributes directly describe some characteristic of the seismic trace (e.g. amplitude, shape); thus, the wave-propagation effects must be included in any quantitative interpretation attempt. *Elastic properties and their spatial arrangement (geometric distribution) must be considered.* Fundamentally, the interpretation of wavelet-dependent attributes is an inverse problem with non-unique solution.

This dissertation presents contributions to the understating and interpretation of both types of seismic attributes. Converted P-to-S elastic impedance (PSEI) as a

wavelet-independent attribute is introduced. The benefits of using PSEI are discussed, particularly in situations that the key elastic properties, needed for discriminating lithology and/or pore-fluids, are not captured with enough accuracy by attributes derived from P-to-P seismic data.

A novel inversion technique for wavelet-dependent attributes, which combines rock physics and multiple-point geostatistics, is presented. The rock-physics component makes it possible to predict situations not sampled by log data. The multiple-point geostatistics component uses geological knowledge to guide the search for solutions. The method can be extended to satisfy multiple physical constraints simultaneously. Therefore, the solutions can be conditioned with different types of geophysical data. *This inversion technique, which is the primary contribution of this dissertation, lays the foundation for innovative, multi-physics, multipoint inversions of geophysical data.*

Acknowledgements

First, I want to express my gratitude to my advisor, Gary Mavko, not only for his outstanding scientific insight, guidance and teaching, but also for his friendship and encouragement. He proposed many of the ideas that founded this dissertation. Gary and Barbara were always ready to give to my family and to me all the support we could need. *Thank you Gary!*

I thank my committee members, Tapan Mukerji, Jef Caers, and Biondo Biondi, for all the guidance during my research. Biondo helped me to make some decisions about the coding of the inversion algorithm. Jef initiated me in multiple-point geostatistics. His comments and suggestions were crucial to define and implement the inversion method.

I especially thank my *two great friends Tapan Mukerji and Youngseuk Keehm*. I thank Tapan for the countless scientific (and philosophical) discussions that not only helped me to complete my Ph.D. but also to increase my knowledge in a broad set of interesting topics. It has been an honor to work with Tapan all these years. His ideas, especially *his certainty about uncertainty*, definitely marked my way of thinking. Tapan also helped me a lot with editing all my papers (included this dissertation). I thank Youngseuk for his unselfish and continuous help, support, and encouragement, for all the patience listening to my problems (not few), for being a great golf companion (we even crossed the “Rubicon”), and for having so many great Thai lunches together (although he complained most of the times, he always agreed to go).

I thank Amos Nur for opening to me the doors to Stanford and waking my interest in a variety of interesting topics, and Jack Dvorkin for all the interesting discussions we had and making me realize about some truths of the scientific world. I learned a lot from both of them.

I am indebted to all the professors at Stanford that I had the honor to meet, especially to Andre Journel for introducing me to the world of geostatistics, and to Albert Tarantola for showing me the beauty of the Monte Carlo ways for inversion problems. It was a real honor to meet and learn from both of you.

I have no words to thank enough Margaret Muir for her friendship and for ALL what she did for my family and for me. Her degree of commitment and responsibility towards the work (i.e. SRB), and her capability for predicting situations (hence, to be ready) are just a sample of the things that I learned from Margaret. *Ta Margaret.*

I am especially grateful to PDVSA-Intevep for all the support I received to come to Stanford. I also would like to thank all the sponsors of the SRB project, especially to Hezhu Yin, Michael A. (Mike) Payne, and Nader Dutta for their support and confidence in my work. I thank Reynaldo Cardona and Sebastien Strebelle from Chevron for their support to obtain the data set used in Chapter 7, Burc Arpat for all the insights with SIMPAT, Scarlet Castro for her assistance with the Stanford VI synthetic reservoir used in Chapter 6, and Reinaldo Michelena for his support that allowed me to come to Stanford and his suggestions related with the converted waves analysis. I want to express my gratitude to Dawn Burgess for helping me with the editing of this dissertation.

I thank my officemates Isao Takahashi, Carlos Cobos, Diana Sava, Andrés Mantilla, Sandra Vega, Juan M. Florez, Laura Chiamonte, Futoshi Tsuneyama, Kyle Spikes, and Kevin Wolf, for all the support and great time we had together. They were always ready to listen and willing to give ideas related with my research. Juan Mauricio helped me a lot with geology, in particular defining the groups for the real data application (Chapter 7). I particularly thank Laura, Kevin and Kyle for reminding me that, although we came to Stanford to work for the Ph.D., there are

other important things that should be done (like being a regular at the Friday beer, and watching a soccer game at Rose and Crown –specially this year that the Barça played really well–).

I thank all the people with whom I had the privilege to share great times at Stanford. The list is large, but some of the names that come right now to my mind are Jan, Jeeyoung, Madhumita, Ran, Per, Mario, Manika, Tiziana, Anyela, Tanima, Richa, Kaushik, Pinar, Franklin, Carmen, Ratna, Lourdes, Alejandro, Gabriel, Daniel, Brad, Jef...

I also want to thank some people that during different periods of my life were crucial for developing my taste for science: Hno. Isaac Melgosa, Hno. Ovidio Galarraga, Omar Weffer, Julian Chela-Flores, and Victor Varela. I thank you.

I express my gratitude to Carmen Mora and Antonio Gomez for being such a good friends. Thank you for taking care of all those things we had to leave unfinished when we came back to Stanford.

I am indebted to my parents, Elena and Ezequiel, my sisters, Elena and Monica, and my brother, Francisco, for their unconditional and continuous support and encouragement. The devotion of my parents towards the family and their capability for maintaining optimism even in the worst situations, definitely have been a main source of motivation always to go forward. They have the ability (especially my father) to see the glass partially filled, even when only a couple of drops were present. They taught me the true meaning of never give up... *este año si!*

I deeply thank my wife, Maria (my dear Pili), for her continuous support, understanding, patience and encouragement. She has been the source of my strength during all these years. Without her at my side, there is no way I would be able to finish my Ph.D. I am really fortunate to have Maria as companion in this amazing adventure of living the life. I dedicate this dissertation, with all my heart, and with all my soul, and with all my mind, to Maria and to our two daughters, Cloe and Briana.

Contents

Abstract	iv
Acknowledgements	vi
Contents	ix
List of Tables	xii
List of Figures	xiii
Chapter 1 Introduction	1
1.1 Motivation and objectives	1
1.2 Chapter Description	4
Chapter 2 Converted P-to-S waves “elastic impedance”	6
2.1 Abstract	6
2.2 Introduction	7
2.3 P-to-S “elastic impedance” derivation	9
2.4 Conclusions	16
Chapter 3 PSEI for identifying lithology and partial gas saturation	17
3.1 Abstract	17
3.2 Introduction	18
3.3 Lithology discrimination	19

3.3.1	Feasibility analysis: Statistical rock physics	20
3.3.2	Classification test using PSEI	28
3.4	Partial gas saturation: fizz water versus commercial gas.....	30
3.5	Conclusions	34
Chapter 4	Practical procedure for P-to-S seismic data inversion.....	36
4.1	Abstract	36
4.2	Introduction	37
4.3	Example 1: Three layers models	38
4.4	Example 2: PSEI from PS data using PP stratigraphic-inversion software for discriminating lithology	43
4.5	Example 3: PSEI from PS data using PP stratigraphic-inversion software for identifying partial gas saturation.....	47
4.6	Conclusions	49
Chapter 5	Inversion method combining rock physics and multiple-point geostatistics	50
5.1	Abstract	50
5.2	Introduction	51
5.3	Proposed algorithm for seismic inversion.....	57
5.3.1	Pre-processing step	59
5.3.2	Inversion step: Seismic (acoustic) inversion.....	65
5.4	Future work	77
5.5	Conclusions	78
Chapter 6	Inversion method: Synthetic tests.....	79
6.1	Abstract	79
6.2	Introduction	80
6.3	Test 1: The model itself as the training image	85
6.4	Test 2: composed training image	91
6.5	Test 3: two groups with overlapping elastic properties	93

6.6	Test 4: Gas sand	95
6.7	Test 5: Starting with an initial <i>guess</i>	103
6.8	Conclusions	104
Chapter 7	Inversion method: Real data application.....	106
7.1	Abstract	106
7.2	Introduction	107
7.3	Data preparation	108
7.4	Inversion.....	110
7.4.1	Pre-processing.....	110
7.4.2	Inversion.....	114
7.4.3	Single well inversions	117
7.5	Conclusions.....	122
References	124

List of Tables

Table 3.1: Cutoff log values used to identify the <i>a-priori</i> defined lithologic groups.	23
Table 6.1: Values of the input parameter used in the first test.....	86
Table 6.2: Parameters used for the fluid substitution.....	96
Table 6.3: Values of the input parameter used in the fourth test.	98
Table 7.1: Parameters to specify the bivariate Gaussian distribution of each group's elastic properties, computed using wells A and B.	111
Table 7.2: Values of the input parameters used for the real seismic data inversion.	114

List of Figures

Figure 2.1: Ray representation of incident P and resulting reflected P and S waves.	10
Figure 2.2: Values of V_s (a) and ρ (b) exponents in the PSEI definition as a function of reflection angle (θ_s in Figure 2.1) for $K=0.4$ (left) and $K=0.5$ (right). In both plots, the magenta star indicates the reflection angle at which PSEI gives the density.	11
Figure 2.3: Values of the Values of V_s (a) and ρ (b) of the PSEI definition as a function of incidence angle (θ_p in Figure 2.1) for $K=0.4$ (left) and $K=0.5$ (right). In both plots, the magenta star indicates the incidence angle at which PSEI gives the density.	13
Figure 2.4: Density values from well logs (red lines) and calculated with the PSEI formula at different incidence angles: (from left to right) -68.2 (θ_{pd}), -69 , and -66 degrees.	14
Figure 2.5: Rho-Vp and PSEI(-10)-PSEI(-50) plots. Points are well log values, color-coded with the volume of shale. Contours correspond to the sands with $Sw=0.8$ (black), 0.5 (green), 0 (red) simulated with Gassmann. <i>mUHS</i> : modified Hashin-Shtrikman upper curve for Quartz-Gas (magenta) and Quartz-Brine (cyan). Black lines indicate the apparent lithology change trend (similar to the bimodal-mixture model).	15
Figure 3.1: Flowchart of the methodology applied to compare the capability of discriminating lithologies between a set of pairs of attributes.	21
Figure 3.2: Log data of the reference well before (gray) and after (blue) editing.	22
Figure 3.3: Log data of the reference well after editing, indicating with color dots the assigned lithologic group.	23
Figure 3.4: Histograms of P-wave velocity (V_p), S-wave velocity (V_s), density (ρ), and acoustic impedance (I_p) for reference well, color-coded by the <i>a-priori</i> groups.	24

Figure 3.5: Vp-Vs and ρ -Vp plots of log data (up) and drawn correlated Monte-Carlo simulations (down), color-coded by the <i>a-priori</i> group. For reference, Castagna <i>et al.</i> (1993) and Castagna's Mudrock (Castagna <i>et al.</i> , 1985) are included in Vp-Vs plots. Similarly, Gardner's relations for sandstone and shale, and the modified Hashin-Shtrikman upper curve are shown in ρ -Vp plots.....	25
Figure 3.6: Normalized histograms of Vp (left column), Vs (center column), and ρ (right column), from log data (left histogram of each subplot) and drawn correlated Monte Carlo simulations (right histogram of each subplot), for each <i>a-priori</i> group (rows from top to bottom: sand, shale, lignite).	26
Figure 3.7: Analyzed pairs of attributes computed using CMC Vp, Vs, and ρ data points. A zoomed window (right) is presented for the PSEI(10)-PSEI(50) plot showing the separation between sand and shale points.	27
Figure 3.8: Conditional probability of the true lithologic group given the correct prediction of lithology (diagonal elements of the Bayesian confusion matrix) for the four pairs of analyzed attributes.	28
Figure 3.9: Reference well. Left: <i>a-priori</i> classification of each depth level based on GR and ρ thresholds, and the resulting Bayesian classification using PSEI(10) and PSEI(50) logs. Right: corresponding Bayesian confusion matrix.....	29
Figure 3.10: <i>Well 2</i> log data (40 km from the reference well). Colors indicate the assigned lithology based on same threshold log values of GR and ρ used for the reference well.	30
Figure 3.11: Lithologic group classification for <i>well 2</i> . Left: classification based on GR and ρ logs thresholds (<i>a-priori</i>), and the obtained Bayesian classification using PSEI(10) and PSEI(50) logs (<i>Pdfs</i> were estimated with training data from only the reference well). Right: corresponding Bayesian confusion matrix.	30
Figure 3.12: Logs from the utilized well (blue lines), and the resulting logs after fluid substitution (Gassmann) with different homogeneous mixtures of brine and gas.....	31
Figure 3.13: PSEI for incidence angles of (-15) and (-50) degrees computed with the well log values from shale and sand with $S_w = 0, 0.3, 0.5, 0.7, \text{ and } 1$	32
Figure 3.14: Bayesian confusion matrix values (top) and their representation in vertical bars (bottom). Each bar corresponds to a row of the confusion matrix, i.e. the probability of predicting any of the groups (colors) when the true group is the one indicated in the abscissa.....	33
Figure 3.15: Conditional probability of the true group (fizz water, commercial gas) given the prediction (diagonal elements of the Bayesian confusion matrix) for the four pairs of attributes studied.....	34

Figure 4.1: Elastic properties and derived PSEI(-50°) for the variations of Sw in the reservoir with thickness of 100 meters.....	39
Figure 4.2: Synthetic traces ($\theta=-50^\circ$) for the models with reservoir Sw=0 (left) and Sw=1 (right), and the picked horizons used as input information for the inversion.....	39
Figure 4.3: Traces computed using full wave modeling (blue) and convolution (red) of the reflectivity derived from PSEI, and the two wavelets: 40 Hz Ricker wavelet (center-left), and wavelet extracted from the full wave modeled trace (center-right).	42
Figure 4.4: One possible solution (maximum <i>a-posteriori</i>) or model for each trace selected from the <i>posterior pdf</i>	43
Figure 4.5: Synthetic PS traces (ray tracing algorithm) for offsets between 0 and 2000 m. Color lines are contours for constant incidence angle (P-wave incidence angle).	44
Figure 4.6: PSEI calculated logs, and pseudo-velocity and pseudo-density, sampled in pseudo-depths, for incidence angles of 10 and 50 degrees.	45
Figure 4.7: PSEI for incidence angles of 10 (left) and 50 (right) degrees calculated using log data (blue) and obtained from the inversion of the PS synthetic traces.	46
Figure 4.8: Bayesian classification results for <i>reference well</i> inverted synthetic seismic, using the conditional <i>pdfs</i> obtained from the logs. Left: <i>a-priori</i> and the result from the Bayesian classification lithologic indicator for each time level. Right: Resulting Bayesian confusion matrix.....	47
Figure 4.9: Original logs (blue lines) and computed logs (Gassmann) simulating fluid substitution with four different water (Sw) and gas (1-Sw) saturations....	48
Figure 4.10: Computed pseudo-logs sampled at pseudo-depths for $\theta=(-25)$ deg. (left) and $\theta=(-50)$ deg. (right). Colors indicate Sw.	48
Figure 4.11: Inverted PSEI (reservoir level) for $\theta_p=(-25)$ degrees (left) and (-50) degrees (right), color-coded by Sw (as Sg increases, i.e. Sw decreases, PSEI values tend to decrease).	49
Figure 5.1: The two main steps of the seismic inversion method proposed –pre-processing and inversion itself– specifying the principal processes in each one.	58
Figure 5.2: Typical groups defined for the simplest case of lithology identification in a clastic reservoir, inverting seismic (acoustic) data. For inverting acoustic data, each defined group has an associated distribution of P-wave velocity and density.	60

Figure 5.3: A rock-physics-based extension of the groups presented in Figure 5.2. The arrows indicate the rock-physics model used in each case: Gassmann fluid substitution (yellow arrow), Dvorkin’s cementation model (green arrow), Marion-Yin-Nur “V” model (red arrows). Details of all the mentioned rock-physics models can be found in Mavko <i>et al.</i> (1998).	60
Figure 5.4: Two-dimensional training image resembling a vertical section of a set of channels (gray cells) encased in a homogeneous background (white cells), and a 3-by-3 reference template.	62
Figure 5.5: Three positions of a 3-by-3 template (orange cells) scanning the training image, and the corresponding extracted patterns.	62
Figure 5.6: Pattern database for the first grid level generated using the template and training image of Figure 5.4.	63
Figure 5.7: Two positions in the second level grid ($g=1$) of a 3-by-3 template (orange cells) scanning the training image and the corresponding extracted patterns.	63
Figure 5.8: Two positions of a second grid level (3-by-3 template), showing the extracted patterns and the corresponding associated patterns.	64
Figure 5.9: Input data used in the example for describing the inversion step: defined grid (cyan cells = empty) with the given well log of group indices, the elastic property distributions of the two defined groups (channel, background shale), and the seismic data.	65
Figure 5.10: Schematic representation of the inversion step in the compact approach version. The components of the elastic loop are highlighted in red. An iteration is completed when all x positions defined in the pseudo-random path are visited.	66
Figure 5.11: Main components of a single SIMPAT* step (step one in this case): selecting cells to be compared ($g = 1$, i.e. second grid level), searching in the pattern database for the best match, and pasting the selected associated pattern.	68
Figure 5.12: The result of four SIMPAT* realizations, completing the first visited x location (well position), i.e. simulating all z for all grid levels (two in this case).	68
Figure 5.13: Multiple realizations of pseudo-logs of elastic properties for the first SIMPAT* realizations of Figure 5.12, the synthetic seismic traces computed for each one, and the collocated seismic data traces (red lines).	70
Figure 5.14: Selection of the elastic properties (V_p , ρ) pseudo-logs that generates the synthetic trace which better reproduce the collocated seismic data trace.	70

Figure 5.15: Results of the elastic loop for the four SIMPAT* realizations of Figure 5.12, and the collocated seismic data traces (red lines).	72
Figure 5.16: Result of the inversion step (compact approach) for the first x -position visited, i.e. the well location.....	72
Figure 5.17: A result of two iterations of the presented inversion method on the synthetic example used for describing the technique. The blue rectangle indicated the well location.	73
Figure 5.18: Flowchart of a single iteration of the inversion step (extended approach). Two loops are completed for every SIMPAT* realization.....	74
Figure 5.19: The two main loops in the inversion step (extended approach). First, a SIMPAT* realization is generated. Then, the elastic loop is completed selecting the synthetic traces that best match the seismic data, within a tolerance range. The selected traces and the corresponding elastic and group indices pseudo-logs are retained and used as the initial state for a following SIMPAT* simulation.	74
Figure 5.20: Illustration of the elastic loop, showing four realizations of pseudo-logs of acoustic impedance for a given SIMPAT* realization, the synthetic seismic traces computed from each one, and the selection of best traces.....	75
Figure 5.21: Last components of the inversion step (extended approach) for each visited x location. Best traces are selected from all the SIMPAT*-elastic loop realizations, forming an ensemble that is compared with the seismic data and previous accepted traces. If a better match, greater than a used-defined value is obtained, the corresponding ensemble of pseudo-logs is pasted into the solution.	76
Figure 6.1: Geological framework of the model used for the first and second tests (top left). Cross-plot of all P-wave velocity (V_p) and density (ρ) values in the model, color-coded by the group (top right). Spatial distribution of V_p and ρ in the model (bottom). The wells (W1, W2) were located at CDP 40 and 120.	82
Figure 6.2: Synthetic seismic computed with Kennett's algorithm using a Ricker wavelet with 15 Hz of central frequency. All seismic traces were included for the color image, but only every fourth trace is plotted with a wiggle trace. W1 and W2 indicate the locations of the two given wells.....	82
Figure 6.3: Acoustic impedance sections (depth) obtained by inverting the synthetic seismic of Figure 6.2 with model-based (left) and sparse-spike (right) algorithms. V_p and ρ information at CDP 40 (W1) and 120 (W2) were used as input data.....	83

Figure 6.4: Well-log data used for the first test, extracted from CDP 40 (W1) and 120 (W2) of the model shown in Figure 6.1. Group-index logs (left) and a plot of P-wave velocity (V_p) and density (ρ) values, color-coded by the group (right).	86
Figure 6.5: (First test) Initial state of the solution grid with only the information from the wells, four intermediates, and the result of a first iteration obtained using the compact approach of the proposed inversion algorithm.	87
Figure 6.6: (First test) Results of one set of six iterations obtained using the compact approach of the proposed inversion technique.	88
Figure 6.7: (First test) Input seismic data, synthetic seismic (output) after six iterations of the inversion compact approach, and the residual (difference sample-by-sample between input and synthetic). All traces are colored and scaled to the same value, but for clarity, the wiggles are plotted only at every other CDP.	88
Figure 6.8: (First test) Probability map for sand (left) and shale (right) groups computed with 30 realizations of the proposed inversion's compact (top) and extended (bottom) approaches. Red vertical lines indicate the locations of the wells (CDP 40 and 120).	89
Figure 6.9: (First test) Probability map for sand (left) and shale (right) groups computed with 30 realizations of the proposed inversion's compact (top) and extended (bottom) approaches, with 30 draws in the elastic loop. Red vertical lines indicate the locations of the wells (CDP 40 and 120).	90
Figure 6.10: (First test) Seismic data (input) and synthetic data (an output) resulting from six iterations of the inversion's compact approach, and the residual (difference sample by sample between input and output data). All traces are scaled to the same value and colored, but for clarity, the wiggles are plotted only at every other CDP.	90
Figure 6.11: Training image used for the second test, formed by twelve cross-sections with the same size as the solution grid. None has the same spatial arrangement of channels as the model used to generate the input data.	91
Figure 6.12: Results from a set of SIMPAT* iterations completed without seismic data to obtain one solution or realization.	92
Figure 6.13: Three realizations (six iterations for each one) generated using SIMPAT* (without seismic) and the well-log data.	92
Figure 6.14: (Second test) Probability maps for sand (left) and shale (right) groups computed with thirty SIMPAT* realizations <i>without conditioning to the seismic data</i> . Red vertical lines indicate the locations of the wells (CDP 40 and 120).	92

Figure 6.15: (Second test) Probability map for sand (left) and shale (right) groups computed with 30 realizations of the proposed inversion’s compact (top) and extended (bottom) approaches. Red vertical lines indicate the locations of the wells (CDP 40 and 120).	93
Figure 6.16: Model used for the third test: spatial distributions of V_p (top left) and ρ (top right), plot of all of V_p and ρ values, color-coded by group (lower left), and the computed seismic data (lower right). The third model was characterized by the overlap between the elastic properties of the two groups.	94
Figure 6.17: Well-log data used for the third test, extracted from CDP 40 (W1) and CDP 120 (W2) of the model shown in Figure 6.16: group-index logs (left) and plot of ρ - V_p log values color-coded by the group index (right).	94
Figure 6.18: (Third test) Probability map for sand (left) and shale (right) groups computed with 30 realizations of the proposed inversion’s compact (top) and extended (bottom) approaches. Red vertical lines indicate the locations of the wells (CDP 40 and 120).	95
Figure 6.19: Model used for the fourth test: spatial distributions of group indices (top left), V_p (top center) and ρ (top right), plot of all of V_p and ρ values color-coded by the group (lower left), and the generated seismic data.	97
Figure 6.20: The twelve variations of one cross-section used as part of the training image in the fourth test. Although the geologic framework remains constant, each image shows a unique distribution of fluids in the geological bodies (connected channels) given by a distinct assignment of groups.	97
Figure 6.21: Well log data used for the fourth test, extracted from CDP 40 (W1) and 120 (W2) of the model shown in Figure 6.19: group-index logs (left) and a plot of V_p and ρ log values, color-coded by the group index (right).	98
Figure 6.22: (Fourth test) Probability map for gas sand (left), brine sand (center), and shale (right) groups computed with 10 realizations of the proposed inversion’s compact approach (top) and extended approach (bottom). Red vertical lines indicate the locations of the wells (CDP 40 and 120).	99
Figure 6.23: Well-log data used for the variation of the fourth test (moved wells), extracted from CDP 50 (WA) and 75 (WB) of the model shown in Figure 6.19: group-index logs (left) and plot of V_p and ρ log values, color-coded by the group index (right).	100
Figure 6.24: (Fourth test – variation of well locations) Probability map for gas-sand (left), brine-sand (center), and shale (right) groups computed with 10 realizations of the proposed inversion’s compact approach (top) and extended approach (bottom). Red vertical lines indicate the well locations (CDP 50, 75).	101

Figure 6.25: Results of the inversion (<i>compact approach</i>) of the seismic data generated from the fourth test model, with the given wells at CDP 50 and 75. Each column corresponds to a particular solution. Rows top to bottom: realizations of group indices, residuals (scaled to the input data), and gL for each iteration of the solution.	102
Figure 6.26: Results of the inversion (<i>extended approach</i>) of the seismic data generated from the fourth test model, with the given wells at CDP 50 and 75. Each column corresponds to a particular solution. Rows top to bottom: realizations of group indices, residuals (scaled to the input data), and gL for each iteration of the solution.	103
Figure 6.27: (Fifth test) Initial stage of the solution grid with only the information from the wells, four intermediates, and the result of a first iteration obtained using the proposed inversion's extended approach.	104
Figure 7.1: Gamma ray (GR), P-wave velocity (V_p), and density (ρ) logs from the two wells used in the study.	107
Figure 7.2: 3D geologic model used to build the training image, and four cross-sections, part of the training image, extracted parallel to the face of the model with a length of 13 km. The complete training image was formed from the cross-sections (x - z planes) at all y values.	108
Figure 7.3: 2D near-offset seismic data extracted from the Chevron's seismic volume, showing the locations of the used well.	109
Figure 7.4: Well-logs of the two wells used in the study, color-coded by the group index assigned to each depth level.	109
Figure 7.5: V_p - ρ values, color-coded by group index from well logs (left) and drawn (300 points per group) (right) from the bivariate Gaussian with mean, variance, and covariance computed from the well logs and represented by the ellipses.	111
Figure 7.6: Amplitude as function of time (left) and amplitude spectrum (right) of the wavelet extracted from the seismic data and used for the convolution in the inversion.	112
Figure 7.7: For Well A (left) and Well B (right), group-index well logs with the original (0.2 meters) and upscaled (5.6 meters) sampling depth interval, synthetic seismic traces computed from 30 V_p and ρ pseudo-well realizations (green), synthetic trace from original logs (red), and real seismic data trace (blue).	113
Figure 7.8: Input seismic data (top), output synthetic data (middle row) of three solutions obtained with compact approach, and the residual or difference sample-by-sample between input and output data (bottom row). All plots are scaled to the same value.	115

Figure 7.9: Four solutions (seven iterations each one) obtained using the compact approach. Red vertical lines indicate the locations of the wells used as input data (CDP 12 and 35).....	116
Figure 7.10: Four solutions (seven iterations each one) obtained using the extended approach. Red vertical lines indicate the locations of the wells used as input data (CDP 12 and 35).....	116
Figure 7.11: Probability map for sand (left), overbank (center), and shale (right) groups computed with 10 realizations of the proposed inversion’s compact (top) and extended (bottom) approaches. Red vertical lines indicate the locations of the wells used as input data (CDP 12 and 35).....	117
Figure 7.12: Values of the degree-of-fitting parameter, gL , for the seven iterations of the 10 solutions obtained with the proposed inversion’s compact (red triangles) and extended (blue circles) approaches.....	117
Figure 7.13: Probability map for sand (left), overbank (center), and shale (right) groups computed with 10 realizations of the proposed inversion’s compact (top) and extended (bottom) approaches. Red vertical line indicates the location of Well B (CDP 12), used as input data.	118
Figure 7.14: Solutions at the Well A location (CDP 35) obtained with the inversion’s compact (left) and extended (right) approaches. Only Well B was used as input data for the inversion.....	118
Figure 7.15: Probability map for sand (left), overbank (center), and shale (right) groups computed with 10 realizations of the proposed inversion’s compact (top) and extended (bottom) approaches. Red vertical line indicates the location of Well A (CDP 35), used as input data.	119
Figure 7.16: Solutions at the Well B location (CDP 12) obtained with the inversion’s compact (left) and extended (right) approaches. Only Well A was used as input data for the inversion.....	120
Figure 7.17: V_p - ρ values, color-coded by the group index from Well A (left) and Well B (right). The ellipses were computed with each group mean, variance, and covariance.....	120
Figure 7.18: Probability map for sand (left), overbank (center), and shale (right) groups computed with 10 realizations of the proposed inversion’s extended approach. Red vertical line indicates the location of Well A (CDP 35), used as input data. Mean, variance and covariance to define the elastic properties of each group were computed using Well B information.....	121
Figure 7.19: Solutions at the Well B location (CDP 12) obtained using Well A as input data for the inversion. Mean, variance and covariance to define the elastic properties of each group were computed using Well B information.	122

Chapter 1

Introduction

“The important thing is not to stop questioning. Curiosity has its own reason for existing. One cannot help but be in awe when he contemplates the mysteries of eternity, of life, of the marvelous structure of reality. It is enough if one tries merely to comprehend a little of this mystery every day. Never lose a holy curiosity” (Albert Einstein)

1.1 Motivation and objectives

The final goal of seismic attribute interpretation is to predict reservoir properties such as lithology, porosity, and fluid saturation from seismic data. Rock physics has been successful establishing point-by-point links between reservoir properties and their elastic responses. However, in real applications it is nearly impossible to find a unique relationship between seismic response and reservoir properties. One could argue that conventional rock physics does not apply at the seismic scale. Among the causes of that non-uniqueness, the earth’s heterogeneity and complexity, and the limited resolution of the seismic waves are indubitably among the most important.

Attempting to list all the seismic attributes that have been used, or even just the ones that most of the commercial seismic-interpretation software can compute, is a difficult task because of the large number and non-standardized names given to them.

Various ways to group or classify seismic attributes have been presented (e.g. Brown, 1996; Taner, 2001) based on different criteria, including the way attributes are computed or the seismic-data domain in which they are calculated. I propose to classify the seismic attributes in two groups: wavelet-independent and wavelet-dependent. The motivation of this form of grouping is that, in my opinion, the methods to interpret each one must be different.

The *wavelet-independent* seismic attributes are those seismic attributes that can be interpreted as the response of a well-defined reservoir range of times or depths. A distinctive characteristic of this category of attributes is that wavelet or scale effects have been removed during the attributes' calculation. Acoustic impedance inverted from a seismic trace is an example of this type of attribute, given that an impedance value is obtained for each sample of the input seismic traces. The uncertainty in the elastic-to-reservoir-properties transformations has to be considered when wavelet-independent seismic attributes are interpreted; that is, the elastic-reservoir-properties equivalence must be established not with single values, but with *distributions* of values. One of the common pitfalls in seismic-attribute interpretation is to oversimplify the problem, disregarding the variability of the elastic response of "similar" reservoir rocks and fluids observed in nature. Statistical rock-physics methods (Mukerji *et al.*, 2001) have been developed as a way to account for the uncertainty due to the multi-valued point-by-point relations between elastic (in the seismic case) and reservoir properties.

The *wavelet-dependent* seismic attributes are the seismic attributes that directly describe some characteristic of the seismic trace as its amplitudes or shape in an interval; hence, the wave-propagation effects must be included in any quantitative interpretation attempt. This means that not only the elastic properties of rocks, but also how they are spatially organized (geometric distribution) must be considered. Fundamentally, the interpretation of the wavelet-dependent attributes is an inverse problem, the solutions of which are reservoir property models with seismic responses that match the seismic data within a tolerance range. To compute the seismic response of the reservoir models we must first transform it into elastic properties;

thus, defining a reservoir-elastic-properties transformation is a step implicitly included in the inversion process.

This dissertation presents contributions to the understating and interpretation of both types of seismic attributes. The *converted P-to-S elastic impedance (PSEI)* as a wavelet-independent attribute is introduced. I discuss the benefits of using PSEI when the intrinsic, key elastic rock properties, needed for discriminating lithology and/or pore-fluids, are not captured with enough accuracy by attributes derived from reflection P-to-P seismic data.

The key innovation of this dissertation is a novel inversion technique related to wavelet-dependent attributes, which combines rock physics and multiple-point geostatistics. Understanding and including rock physics at the beginning of the process makes it possible to predict situations not sampled by log data, and to attempt to answer “What if?” questions. Through the multiple-point geostatistics component, the geological knowledge is incorporated in the search for solutions. Moreover, the method can be extended to satisfy multiple physical constraints simultaneously; in other words, the solutions can be conditioned with different types of geophysical data. My principal references for developing the proposed inversion technique included the statistical rock-physics principles and methods introduced by Mukerji *et al.* (2001), the value of rock physics for establishing links between elastic and reservoir properties concisely presented in Mavko *et al.* (1998), Tarantola’s ideas about the stochastic formulation of the geophysical inverse problem (Tarantola, 2005), the links between depositional environments and rock physics explored by Avseth (2000), Gutierrez (2001), and Florez (2005), Takahashi’s (2000) results about scale effects in rock property estimation, the proposal by Bortoli *et al.* (1993) and Haas and Dubrule (1994) for using geostatistics for seismic inversion, and the multiple-point geostatistics concepts and algorithms presented by Strebelle (2000), Arpat (2005) and Zhang (2006).

1.2 Chapter Description

Chapter 2 introduces a formulation of the “elastic impedance” of incidence-angle-dependent P-to-S converted waves (P-to-S Elastic Impedance, or PSEI), and illustrates how changes in fluid saturation and lithology are translated into well-defined trajectories when the PSEI for two incident angles are plotted versus each other.

Chapter 3 presents two practical, statistical rock-physics applications of PSEI using well-log data. First, it shows how PSEI better discriminates lithology in elastic sequences with small acoustic impedance (I_p) contrasts. Second, it shows how, through PSEI, it is possible to distinguish fizz water from commercial gas concentrations.

Chapter 4 provides a method for obtaining PSEI from P-to-S seismic data using PP stratigraphic inversion software, and discusses the validity of some of the approximations assumed. Three examples with synthetic are presented, to show the feasibility of obtaining PSEI values using the same principles as those of PP data inversion. In the first example, PS synthetic traces from a set of three-layer models are inverted to obtain PSEI using a probabilistic approach. The second and third synthetic examples illustrate the proposed methodology to derive PSEI from PS data using commercial PP stratigraphic-inversion software. The method is based on generating a pseudo-velocity and a pseudo-density log, sampled at pseudo-depth units. The technique exploits the similar functional expression of acoustic impedance and PSEI. Rather than developing new inversion algorithms, the objective of this chapter is to show the viability of a practical procedure to compute PSEI from PS seismic data.

Chapter 5, which I consider the most important of this dissertation, introduces a new inversion technique that combines rock physics and multiple-point geostatistics in a Bayesian framework. I present the proposed method for inverting seismic data in reservoir characterization situations, but in general, it can be applied to any inverse problem that can be approximated as a series of unidimensional forward-modeling operators. The solutions given by the inversion technique proposed are

multiple realizations of spatial distributions of *groups* consistent with the available well data, seismic data, and the geological interpretation. The method can be extended to satisfy multiple physical constraints simultaneously; in other words, the solutions can be conditioned with different types of geophysical data.

Chapter 6 shows and analyzes the results of a set of tests applied to the proposed inversion techniques. Synthetic, normal-incidence seismic (acoustic) data is inverted to predict the spatial arrangement of groups in a reservoir. For all tests, the model itself is clearly depicted by the zones with high values in the computed probability maps. The models used are 2D cross-sections extracted from a modified version of the Stanford VI synthetic reservoir, created by the geostatistics group (Petroleum Engineering department, Stanford University).

Finally, Chapter 7 presents the first inversion of real seismic data using the proposed technique, demonstrating its applicability to real situations. The data used was provided by Chevron. The rocks in the studied reservoir were deposited in a clastic marine environment located on the continental slope, where turbidites are the main type of reservoir rock. The way in which the implemented algorithms handle the common situation of data with different sampling intervals is also described in the last chapter.

Chapter 2

Converted P-to-S waves “elastic impedance”

“All truths are easy to understand once they are discovered; the point is to discover them.” (Galileo Galilei)

2.1 Abstract

In this chapter, a formulation of the “elastic impedance” of incidence-angle-dependent P-to-S (PS) converted waves (P-to-S Elastic Impedance, or PSEI) is presented. The main assumptions for PSEI derivation are the validity of the convolutional model for PS converted waves and weak contrast between layers. As is shown, for an analytically defined angle, PSEI gives a direct density estimator. However, as is demonstrated, obtaining in practice a single density value using seismically derived PSEI is a very difficult task, principally because of the precision required in the incidence or reflected angle. Moreover, the validity of the density derivation from PSEI can be compromised by inexact knowledge of the ratio between shear and compressional velocities (V_s/V_p), noise in seismic data, processing artifacts, and imperfections of PS seismic inversion to obtain PSEI. Nevertheless, these facts only limit the possibility of deriving absolute values of density. They do not preclude the potential use of PSEI for discriminating between

reservoir conditions where density is the key elastic property. In other words, though it will be difficult to *estimate* directly absolute densities through PSEI, it will still be possible to *classify* based on relative density variations. Finally, how changes in fluid saturation and lithology are translated into well-defined trajectories when the PSEI for two incident angles are plotted versus each other is illustrated.

2.2 Introduction

In some hydrocarbon exploration and production situations, attributes derived from P-to-P reflection seismic data (PP) do not capture with enough accuracy the key elastic rock properties for identifying the reservoir lithology, pore fluids, and/or pressure-temperature conditions. Converted P-to-S (PS) waves have been proposed and used as a source of valuable information in those instances. Stewart *et al.* (2003) summarize a broad spectrum of successful applications of PS converted waves, from imaging improvements to lithology estimation, fluid description, and reservoir monitoring.

Different approaches have been presented for using PS waves to obtain information about reservoir properties. Some techniques aim to take advantage of PS reflectivity (R_{ps}) variations as a function of the incidence angle, either through weighted stacking methods (Larsen *et al.*, 1999; Kelly *et al.*, 2000; Margrave *et al.*, 2001; Veire *et al.*, 2001), or using R_{ps} approximations for applying the well-established PP amplitude versus offset (AVO) type of analysis (Engelmark, 2000; González, *et al.*, 2000; Jin, *et al.*, 2000; Wu, 2000; Zhu, *et al.*, 2000; Ramos and Castagna, 2001). All those reflectivity-based methods are particularly useful for qualitative analysis or for analyzing a specific seismic reflection.

Another group of techniques aims to compute elastic properties at every depth or time sampling interval. Mallick (2001) describes a procedure for prestack waveform inversion of multi-component seismic data (vertical and in-line components) to obtain compressional-wave velocity (V_p), density (ρ), and Poisson's ratio, using genetic algorithms. This may be one of the most complete approaches, but it is also computationally very expensive. Moreover, obtaining the values of the elastic

properties is not the primary goal in most real cases. On the contrary, the main objective is commonly limited to discriminating between variations of *a-priori* defined groups of reservoir properties. Valenciano and Michelena (2000) present a methodology to invert poststack PS-converted-wave data, linearizing R_{ps} . The linearization is done in a way that the derived expression is functionally similar to the PP reflectivity (R_{pp}); therefore, pseudo-S-wave impedance can be obtained through conventional stratigraphic inversion of PS data. They combine PP and the proposed pseudo-S-wave impedance to obtain an estimation of reservoir-rock density. Landro *et al.* (1999) derive an expression for a quantity that they name “shear-wave elastic impedance” (SEI), assuming the validity of the convolutional model for non-normal incidence angle, weak elastic contrast, and small incidence angles. Duffant *et al.* (2000) extract SEI from North Sea data and show how instantaneous V_p/V_s can be obtained by combining SEI and PP elastic impedance. As can be noticed, the PS data-inversion methods referenced are based on linear approximations of R_{ps} , and their authors propose to use the results combined with some type of PP data inversion.

In this chapter, the derivation of PS elastic impedance (PSEI) is presented and some properties of this seismic attribute are analyzed. PSEI can be a decisive attribute for solving reservoir-property discrimination problems where density contains most of the information. Unlike SEI, PSEI does not have the small-angle restriction, a fact that opens a series of new possibilities for identifying reservoir characteristics with partial PS stack data (with a limited range of incidence angles). Although the work of Duffant *et al.* (2000) suggests the possible use of a nonlinear approximation of R_{ps} for SEI derivation, this chapter shows additionally that it is theoretically possible to obtain a direct estimation of reservoir-rock densities from PSEI, though this is a very difficult task in practice. Finally, how changes in fluid saturations and lithology are reflected as consistent trajectories when PSEI for two incident angles are plotted versus each other is illustrated.

2.3 P-to-S “elastic impedance” derivation

In a way similar to how Mukerji *et al.* (1998) and Connolly (1999) derived the P-to-P (PP) “elastic impedance” (EI), an analytical expression for the P-to-S “elastic impedance” (PSEI) was obtained. The term *elastic* is used not in the sense of full waveform inversion, but to mean inversion for different offsets.

The normal-incidence reflectivity of P waves, $R_{pp}(0)$, for relative small changes of elastic properties across the interface between two isotropic and homogenous half-spaces, can be written as follows (e.g. Aki and Richards, 1980):

$$R_{pp}(0) \approx \frac{1}{2} \left(\frac{\Delta V_p}{\bar{V}_p} + \frac{\Delta \rho}{\bar{\rho}} \right) \approx \frac{1}{2} \Delta(\ln I_p), \quad (2.1)$$

with

$$\bar{V}_p = \frac{V_{p1} + V_{p2}}{2}; \quad \bar{\rho} = \frac{\rho_1 + \rho_2}{2}; \quad \Delta V_p = V_{p2} - V_{p1}; \quad \Delta \rho = \rho_2 - \rho_1. \quad (2.2)$$

Subindices 1 and 2 reference the upper and lower media properties respectively. Then the normal-incidence P impedance, or acoustic impedance, can be written as follows:

$$I_{pp}(0) = I_p = e^{2 \int R_{pp}(0) dt}. \quad (2.3)$$

In a similar way, assuming the validity of the convolutional model for non-zero and small incidence angles, and weak contrast between layers, the “elastic impedance” is defined as follows (Connolly, 1999):

$$I_{pp}(\theta_p) = EI(\theta_p) = e^{2 \int R_{pp}(\theta) dt} = V_p^{1+\tan^2 \theta} \rho^{1-4K \sin^2 \theta} V_s^{-8K \sin^2 \theta}, \quad (2.4)$$

where

$$K = \frac{1}{2} \left(\frac{V_{s1}^2}{V_{p1}^2} + \frac{V_{s2}^2}{V_{p2}^2} \right), \quad (2.5)$$

and θ_p is the incidence angle as defined in Figure 2.1.

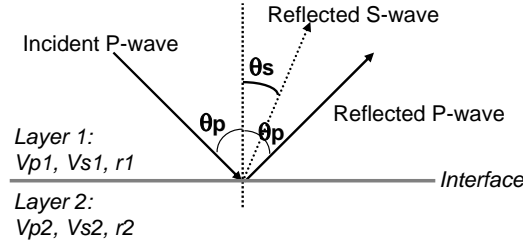


Figure 2.1: Ray representation of incident P and resulting reflected P and S waves.

Equivalently, the reflectivity for PS waves as a function of the reflected (S-wave) angle, assuming weak contrast and following the notation illustrated in Figure 1 (positive offsets), can be written as follows (Aki and Richards, 1980):

$$\begin{aligned}
 R_{ps}(\theta_s) \approx & \frac{-\tan \theta_s}{2\left(\frac{\bar{V}_s}{\bar{V}_p}\right)} \left(1 - 2\sin^2 \theta_s + 2\cos \theta_s \sqrt{\left(\frac{\bar{V}_s}{\bar{V}_p}\right)^2 - \sin^2 \theta_s} \right) \frac{\Delta \rho}{\bar{\rho}} + \\
 & + \frac{\tan \theta_s}{2\left(\frac{\bar{V}_s}{\bar{V}_p}\right)} \left(4\sin^2 \theta_s - 4\cos \theta_s \sqrt{\left(\frac{\bar{V}_s}{\bar{V}_p}\right)^2 - \sin^2 \theta_s} \right) \frac{\Delta V_s}{\bar{V}_s}
 \end{aligned} \tag{2.6}$$

Rigorously, the angle used in equation 2.6 is the average between the S-wave reflected and transmitted angles. However, it can be taken as the reflected S-wave angle because of the assumed weak contrast between the elastic properties of the layers.

Solving an integral similar to equation 2.3, the elastic impedance for P-to-S converted waves is given by

$$I_{ps}(\theta_s) = PSEI(\theta_s) = \rho^a V_s^b, \tag{2.7}$$

with

$$a = \frac{\tan \theta_s}{K} \left(2\sin^2 \theta_s - 1 - 2\cos \theta_s \sqrt{K^2 - \sin^2 \theta_s} \right), \tag{2.8}$$

$$b = \frac{4 \tan \theta_s}{K} \left(\sin^2 \theta_s - \cos \theta_s \sqrt{K^2 - \sin^2 \theta_s} \right). \tag{2.9}$$

K is the average V_s/V_p (constant). It must be assumed constant in order to take

it outside the reflectivity integration. In practice, K is commonly calculated using the averages (between layers) of V_s and V_p .

Figure 2.2 displays the values of the exponents a and b as functions of reflected angle, corresponding to negative offsets (or angles) for two different values of K (0.4 and 0.5). Figure 2.2 illustrates that for a certain reflected angle (θ_{sd}), the exponent of V_s (b) is zero, while the ρ exponent (a) is one; hence PSEI precisely gives the density values. The algebra to derive the analytical expression for θ_{sd} is presented below. The idea is to find the non-zero angle at which the exponent b is equal to zero; from equation 2.9, that is,

$$\sin^2 \theta_{sd} - \cos \theta_{sd} \sqrt{K^2 - \sin^2 \theta_{sd}} = 0, \quad (2.10)$$

$$K = \tan \theta_{sd}. \quad (2.11)$$

Then, the angle θ_{sd} is given by

$$\theta_{sd} = \arctan(K). \quad (2.12)$$

Using this analytically derived value of θ_{sd} in equation 2.8, for negative offsets, yields a equal to one. Therefore,

$$\text{PSEI}(\theta_{sd}) = \rho^1 V_s^0 = \rho. \quad (2.13)$$

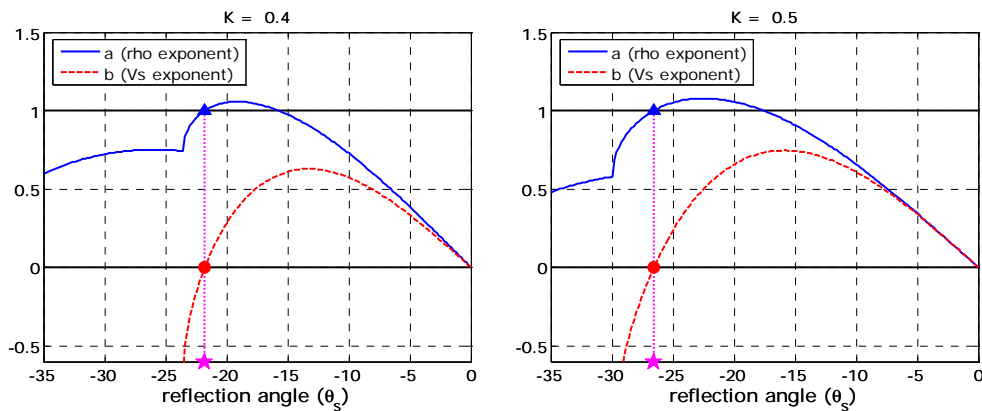


Figure 2.2: Values of V_s (a) and ρ (b) exponents in the PSEI definition as a function of reflection angle (θ_s in Figure 2.1) for $K=0.4$ (left) and $K=0.5$ (right). In both plots, the magenta star indicates the reflection angle at which PSEI gives the density.

PSEI can also be defined as a function of the incidence (P-wave) angle. Simple algebraic calculations using Snell’s law, i.e. $V_p \sin \theta_p = V_s \sin \theta_s$, lead to the result that equations 2.6 to 2.13 can be rewritten as follows:

$$R_{ps}(\theta_p) \approx \frac{-\sin \theta_p}{\left(\frac{\bar{V}_p}{\bar{V}_s}\right) \sqrt{\left(\frac{\bar{V}_p}{\bar{V}_s}\right)^2 - \sin^2 \theta_p}} \left[\left[\frac{1}{2} \left(\frac{\bar{V}_p}{\bar{V}_s}\right)^2 - \sin^2 \theta_p + \cos \theta_p \sqrt{\left(\frac{\bar{V}_p}{\bar{V}_s}\right)^2 - \sin^2 \theta_p} \right] \frac{\Delta \rho}{\bar{\rho}} - \left[2 \sin^2 \theta_p - 2 \cos \theta_p \sqrt{\left(\frac{\bar{V}_p}{\bar{V}_s}\right)^2 - \sin^2 \theta_p} \right] \frac{\Delta V_s}{\bar{V}_s} \right]. \quad (2.14)$$

Then,

$$I_{ps}(\theta_p) = \text{PSEI}(\theta_p) = \rho^c V_s^d, \quad (2.15)$$

with

$$c = \frac{K \sin \theta_p}{\sqrt{\frac{1}{K^2} - \sin^2 \theta_p}} \left(2 \sin^2 \theta_p - \frac{1}{K^2} - 2 \cos \theta_p \sqrt{\frac{1}{K^2} - \sin^2 \theta_p} \right), \quad (2.16)$$

$$d = \frac{4K \sin \theta_p}{\sqrt{\frac{1}{K^2} - \sin^2 \theta_p}} \left(\sin^2 \theta_p - \cos \theta_p \sqrt{\frac{1}{K^2} - \sin^2 \theta_p} \right). \quad (2.17)$$

Finally, the incidence angle at which PSEI gives a direct estimation of density is given by:

$$\theta_{pd} = \arctan\left(\frac{1}{K}\right), \quad (2.18)$$

$$\text{PSEI}(\theta_{pd}) = \rho. \quad (2.19)$$

Figure 2.3 shows the behavior of exponents c and d as a function of incidence angle, indicating the angle (θ_{pd}) at which the PSEI exponent of the V_s term is zero, and the exponent of density is one. It can be noticed that at near offsets or small angles, V_s and ρ values have a similar contribution to PSEI. On the other hand, for mid-to-large offsets, there is a *decoupling* between V_s and ρ , a fact that can be utilized for discriminating different reservoir properties. Note that only the constant K

determines the angle at which the effect is maximized. An analogous observation was discussed by Wu (2000), concerning the reflectivity of converted waves for a particular AVO case (type III).

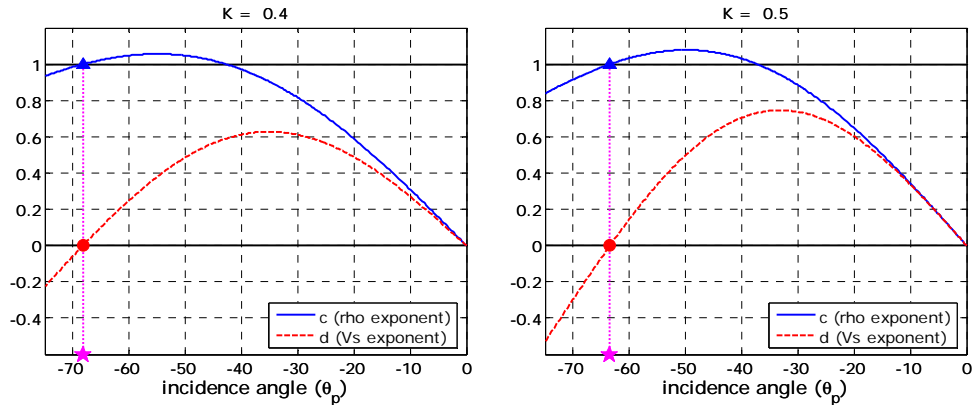


Figure 2.3: Values of the Values of Vs (a) and ρ (b) of the PSEI definition as a function of incidence angle (θ_p in Figure 2.1) for $K=0.4$ (left) and $K=0.5$ (right). In both plots, the magenta star indicates the incidence angle at which PSEI gives the density.

Even though PSEI for the angle θ_{pd} defined in equation 2.18 gives a density estimation, it is very difficult to accomplish this task in practice, as is illustrated in the following example. Figure 2.4 compares a real density log with densities derived from PSEI at different angles. In this particular case, the angle at which $PSEI(\theta_{pd})$ equals ρ is 68.2 degrees. As Figure 2.4 reveals, for θ_{pd} the density is exactly reproduced. However, small variations in the angle used for the calculation introduce a significant error in the estimated density. This result can be explained by the behavior of the PSEI Vs and ρ exponents illustrated in Figure 2.3. The slopes of the c and d exponents are high near the θ_{pd} value; hence, in the vicinity of θ_{pd} , small variations in the angle significantly change the c and d values. In addition to the precision required in the incidence angle, the validity of density derivation from PSEI can be compromised due to the approximate knowledge of V_s/V_p , noise in the seismic data, possible processing artifacts, and imperfections of PS seismic inversion to obtain PSEI. Nevertheless, these facts limit only the derivation of absolute density

values. They do not preclude the potential use of PSEI to *discriminate* between reservoir situations where density is the key elastic property.

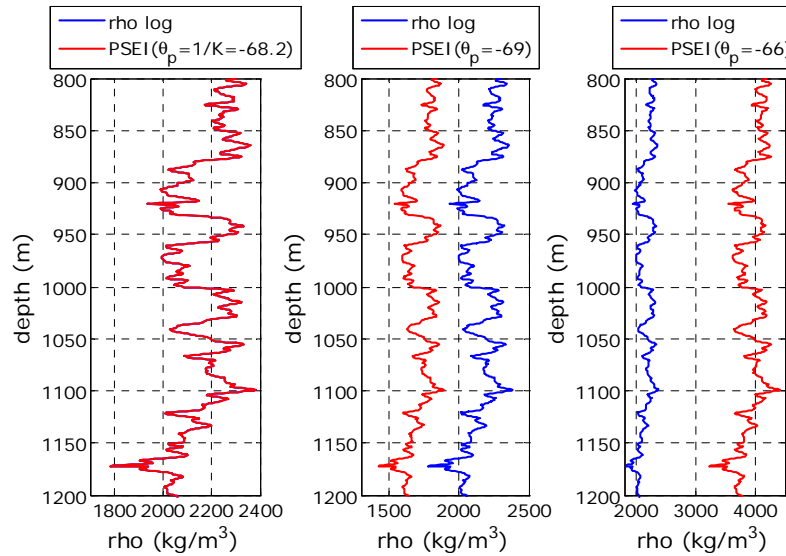


Figure 2.4: Density values from well logs (red lines) and calculated with the PSEI formula at different incidence angles: (from left to right) -68.2 (θ_{pd}), -69 , and -66 degrees.

As was mentioned before, knowing the precise values of an elastic property is not necessarily the main goal for using seismic data. It is usually more important to be able to understand and predict the behavior of elastic properties, or ultimately a seismic attribute, resulting from changes in reservoir properties. Rock-physics models have been developed to establish that link between elastic and reservoir properties. Consequently, observing the behavior of rock-physics models in the PSEI domain gives the opportunity to predict how PSEI will respond to some reservoir changes, such as lithology and saturations.

Figure 2.5 presents plots of real log values color coded by the volume of shale in density- V_p and PSEI(-10)-PSEI(-50) planes. Moreover, contours of values calculated with Gassmann’s equations are included, simulating the substitution of the original water in the sands by three different homogeneous water-gas mixtures. Modified (critical porosity) Hashin-Shtrikman curves ($mHSU$) for mixtures of

quartz-gas (Qz -gas) and quartz-brine (Qz -Bri) are also plotted in each graph, with an arrow indicating the *diagenesis or depth trend* (Avseth, 2000). As can be seen in Figure 2.5, $mHSU$ for Qz -Bri fits the points corresponding to clean, fully water-saturated sands. Likewise, $mHSU$ for Qz -Gas passes over the contours calculated with Gassmann for the fully gas-saturated sands. It also can be noticed how the cloud of points is distributed as an *inverted V*, from clean sandstones to pure shale going through the mixture; hence, data points seem to behave as predicted by the bimodal-mixture model (e.g. Dvorkin and Gutierrez, 2001).

Besides the mentioned expected data-model fits, Figure 2.5 illustrates two important new results. In the PSEI(-10)-PSEI(-50) plane, *changes in water-gas saturations* are translated in clear trajectories; i.e. *the points move monotonically in well-defined directions*. Furthermore, the values of PSEI increase almost linearly as *diagenesis effects* increase. These new observations indubitably show the potential of PSEI for predicting lithology and identifying partial gas saturation, which are two important problems in the hydrocarbon exploration context.

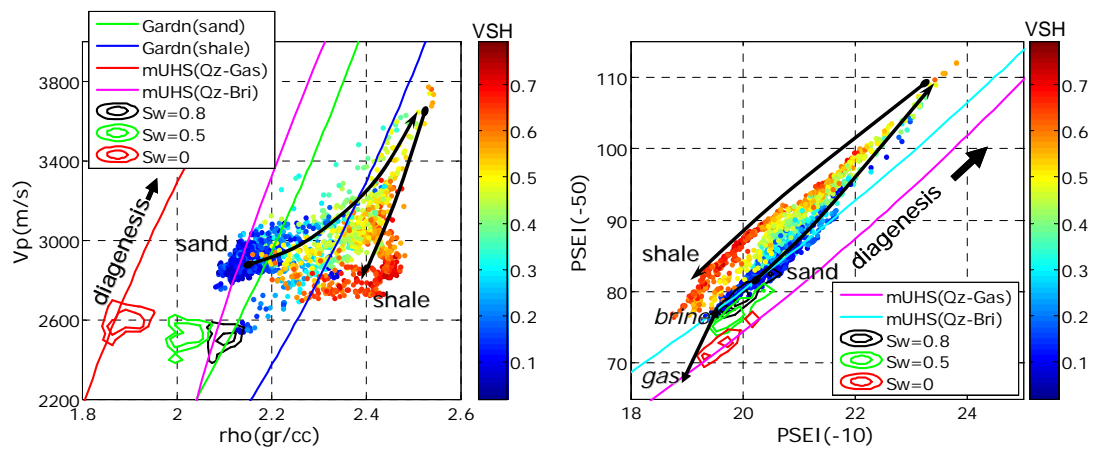


Figure 2.5: Rho-Vp and PSEI(-10)-PSEI(-50) plots. Points are well log values, color-coded with the volume of shale. Contours correspond to the sands with $Sw=0.8$ (black), 0.5 (green), 0 (red) simulated with Gassmann. $mUHS$: modified Hashin-Shtrikman upper curve for Quartz-Gas (magenta) and Quartz-Brine (cyan). Black lines indicate the apparent lithology change trend (similar to the bimodal-mixture model).

2.4 Conclusions

In this chapter a formulation of P-to-S “elastic impedance” (PSEI) was presented. The theoretical derivation assumes the validity of the convolutional model for PS converted waves and weak contrast between the elastic properties across the reflecting interface. The asymmetric contribution of V_s and ρ on PSEI can be exploited in discriminating different reservoir properties. This *decoupling* between the roles of V_s and ρ gives rise to clear trajectories in the $PSEI(\theta_1)$ - $PSEI(\theta_2)$ plane for changes in lithology and water-gas saturations; i.e. the points move monotonically in well-defined directions. Using PSEI for two different angles (e.g., corresponding to near and far offsets) can contain enough information for identifying the reservoir property of interest. Consequently, the difficulty of matching PP and PS reflections is avoided.

Although the theoretical value of the angle at which PSEI translates to a direct density value was derived, in practice it will be difficult to estimate densities directly from PSEI. However, this fact limits only the possibility of obtaining absolute density values. It does not prevent the potential use of PSEI for discriminating between reservoir situations where density is the key elastic property.

Chapter 3

PSEI for identifying lithology and partial gas saturation

“The ideal reasoner, he remarked, would, when he had once been shown a single fact in all its bearings, deduce from it not only all the chain of events which led up to it but also all the results which would follow from it”
(Sherlock Holmes, in "The Five Orange Pips," by Sir Arthur Conan Doyle)

3.1 Abstract

The use of P-to-S (PS) converted waves has been proposed as a possible solution for the problems of seismically discriminating lithologies with similar acoustic impedances and identifying partial gas saturations. For example, Engelmark (2000) shows how in many Tertiary clastic reservoirs, PS seismic data can be used to differentiate between shale and sand. Wu (2000) and Zhu *et al.* (2000) show the feasibility of using PS reflectivity for distinguishing fizz water from commercial gas. In both mentioned situations, the elastic property that carries the information for distinguishing lithology or partial gas saturation is the density; hence the difficulty when using only PP seismic data. Attempting to extract information about rock density from amplitude-versus-offset (AVO) analysis or conventional seismic inversion has not always been a successful approach, because of limitations in the

data quality and the type of processing required. The effect of density on P-wave data is small compared with the compressional and shear wave velocities (V_p and V_s) contributions.

In this chapter, two practical applications of the PS elastic impedance (PSEI) using well-log data are presented. First, how PSEI better discriminates lithology in clastic sequences with small acoustic impedance (I_p) contrast is shown. Second, how through PSEI it is possible to distinguish fizz water from commercial gas concentrations is shown. Statistical rock-physics methods were applied to reach these conclusions and to compare PSEI with a group of PP attributes: λ , μ , $\rho\lambda$, $\rho\mu$, and EI (where λ and μ are the Lamé constants, and EI is the PP elastic impedance). Although the absolute values of the results are valid only for the analyzed wells, the idea of using PSEI for discriminating lithology and partial gas saturations can be extrapolated to situations where density is the key elastic property. The methodology presented in this chapter is completely general, and it is a way to do feasibility studies. Using only well-log data and rock physics before working with seismic information makes it possible to predict, in a relatively fast way, whether the elastic properties in the study area respond to changes in the reservoir properties of interest.

3.2 Introduction

Identifying lithology and distinguishing between fizz water and commercial gas are two specific problems that in many cases cannot be solved with only P-to-P (PP) seismic information. The phenomenon of sand-shale crossover with depth can give rise to significant overlap in acoustic impedance (I_p), making it difficult to discriminate sand from shale using PP data alone. Attempting to differentiate the seismic response of sands with low gas saturation (fizz water) from higher gas concentrations is difficult. The abrupt reduction in P-wave velocity (V_p) with the first few percent of gas controls the seismic response. Therefore, usually only the presence of gas, but not the saturation, can be detected with PP seismic. This well known physical phenomena can be modeled by Gassmann's equations, and was

documented by Domenico in 1976. In contrast, density (ρ) varies more gradually and linearly with gas saturation, while S-wave velocity (V_s) does not change much. As noted by Berryman *et al.* (2002), the linear behavior of ρ with saturation makes seismic attributes that are closely related to density useful proxies for estimating gas saturation. Attempting to extract and use information about rock density from AVO analysis or inversion has not been a successfully robust approach in many cases because of limitations in data quality and the type of processing required.

The use of P-to-S (PS) converted waves has been suggested as a source of additional information for discriminating lithology with low impedance contrast (e.g. Engelmark, 2000), and for distinguishing high versus low gas saturation (Wu, 2000 and Zhu *et al.*, 2000). Those works propose using PP and/or PS reflectivity (R_{pp} , R_{ps}), which are interface properties.

This chapter, using well-log data, shows how exploiting the PS AVO behavior, by combining near-offset and mid-to-far offset PSEI, it is possible to discriminate between lithologies with low I_p contrast and to distinguish fizz water from commercial gas concentrations. Using statistical rock-physics methods, the classification success ratio of PSEI with the classification success ratio of a group of intervallic PP attributes is compared. As is shown, using PSEI for near and mid-to-far offsets simultaneously dramatically increases the probabilities of seismically differentiating between sand and shale with similar I_p and of discriminating between areas with high and low gas saturations. Obviously, the computed success ratio values are valid only for the analyzed wells. However, the idea of using PSEI for discriminating lithology and partial gas saturations can be extrapolated to situations where density is the key elastic property.

3.3 Lithology discrimination

Lithology identification using PP seismic data is a common problem in shallow and not-well consolidated sequences of clastic sediments. The main reasons for the difficulty of identifying sand and shale are the overlap in acoustic impedance, small Poisson's ratio differences, and acquisition constraints, such as limited angles

(Engelmark, 2000). Therefore, not only is it hard to identify lithology with I_p , but also attempting to use the changes of amplitudes with offsets (AVO) is not necessarily a solution. On the other hand, in those types of reservoirs, the densities of sand and shale are commonly different; hence, PS seismic data, and PSEI in particular, is a source of information to be considered. As was showed in the previous chapter, PSEI is closely linked to density.

To compare PSEI with other PP seismic attributes for discriminating lithology in reservoirs with low I_p contrast, the statistical rock physics methods of Mukerji *et al.* (2001) and Avseth *et al.* (2005) were adapted and applied to a set of real well-log data. Three lithologic groups were defined *a-priori*: sand, shale, and lignite. The lignite group was included because of its very distinctive characteristics of thin layers with very low densities. Below, the main steps of the applied statistical rock-physics method, obtaining estimates of the uncertainty for discriminating between the three *a-priori* defined groups in a reference well are described. Then, for validation purposes, lithology is predicted in a second well, located 40 kilometers from the reference well, using the PSEI-computed well logs. The Bayesian classification success rate is analyzed and discussed.

3.3.1 Feasibility analysis: Statistical rock physics

The applied methodology, based on the statistical rock-physics methods of Mukerji *et al.* (2001) and Avseth *et al.* (2005), is summarized in Figure 3.1. It basically consists of the following steps: First, a well with good-quality sonic and density logs is selected as the reference well. The logs are classified into the groups of interest (e.g. common lithology, pore fluids, etc.). This can be done by defining threshold values for some logs, or by using well-test data. Rock-physics models can be used to extend the well-log observations, i.e. extending the training data, when an expected group in the study area was not sampled by the logs. From each group independently, correlated Monte-Carlo (CMC) simulations are drawn for V_p , V_s , and ρ . These values are used to calculate the seismic attributes, i.e. any observable signature that can be extracted from the seismic data. Then, kernel-based, non-

parametric, probability-density estimation is used to obtain the class-conditioned probability-density functions (*pdfs*), that is, the conditional *pdfs* for each group. Based on the estimated *pdfs*, the best attribute or combination of attributes for discriminating between the defined groups can be selected, either by simple visual inspection or by classification success ratio analysis (e.g. Bayesian confusion matrices, discriminant analysis, etc.).

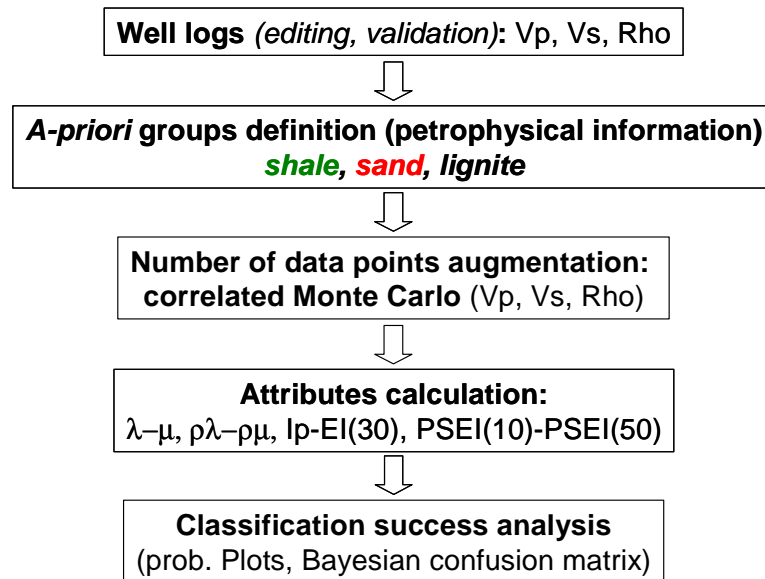


Figure 3.1: Flowchart of the methodology applied to compare the capability of discriminating lithologies between a set of pairs of attributes.

Only pairs of intervallic seismic attributes with well-established physical meaning were analyzed: $\lambda\rho - \mu\rho$ (Goodway *et al.*, 1997), $\lambda - \mu$ (Gray, 2002), $I_p - EI(30)$, and $PSEI(10) - PSEI(50)$. λ and μ are Lamé's parameters, I_p is the acoustic impedance, $EI(30)$ is the PP elastic impedance for 30 degrees (Connolly, 1998, 1999; Mukerji *et al.*, 1998) and $PSEI(10)$ and $PSEI(50)$ are PS elastic impedances (presented in the previous chapter) for incidence angles of 10° and 50° respectively. The first three pairs of attributes can be obtained from PP seismic data, and with them, PP AVO variations are included in the analysis. All these attributes are analytically defined; hence, they can be calculated with V_p , V_s , and ρ log values, as well as extracted from the seismic data.

Well-log editing

Before attempting to assign a group indicator to every sampled depth, the consistency of information between logs needs to be checked, to clean the data and remove bad measurements. The consistency review was based on two logs: neutron porosity (NPHI) and density porosity (DPHI). For the studied well, shale (mainly clays) is expected to show high gamma-ray (GR) log values and greater NPHI than DPHI, due to the trapped water in clay minerals. On the other hand, in the clean sands NPHI and DPHI logs must be similar. The third *a-priori* group, lignite, is a low-density hydrogenous medium with high carbon content; therefore, NPHI response must be high even in formations containing little water (Hearst *et al.*, 2000). Points that did not satisfy any of those criteria or corresponded to depths with high variations in the caliper log were discarded. Figure 3.2 shows logs of the reference well before and after editing.

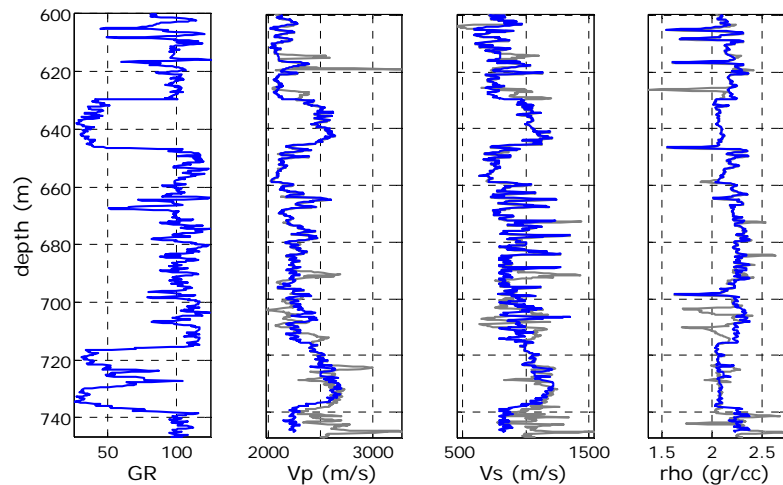


Figure 3.2: Log data of the reference well before (gray) and after (blue) editing.

Group definition

The criteria for assigning a group indicator (categorical variable) to each depth point was defined in terms of cutoff values of gamma-ray (GR) and density (ρ) logs, as indicated in Table 3.1. Figure 3.3 shows some of the edited logs of the reference well indicating the *a-priori* assigned lithologic group, *viz.* sand, shale, or lignite.

Figure 3.4 presents histograms of V_p , V_s , ρ , and I_p calculated for each defined group. Although the V_p , V_s , and ρ distributions of sand and shale show certain separations, the overlap in I_p is remarkable. This is not a peculiarity of the studied area; in fact, it is a common situation in relatively shallow clastic reservoirs. At shallow depths, sands usually have smaller I_p than shale. With increasing depth, there is a crossover, and I_p for sands becomes greater than that for shale. Consequently, for some range of depths, there is little or no I_p contrast between sand and shale. On the other hand, amongst the three variables selected to describe the elastic response (V_p , V_s , ρ), density appears to be the key property for discriminating between the *a-priori* lithologic groups.

Table 3.1: Cutoff log values used to identify the *a-priori* defined lithologic groups.

Group	Gamma Ray log (GR)	Density log (ρ)
Sand	≤ 50	≥ 2
Shale	≥ 80	≥ 2
Lignite	-	≤ 1.9

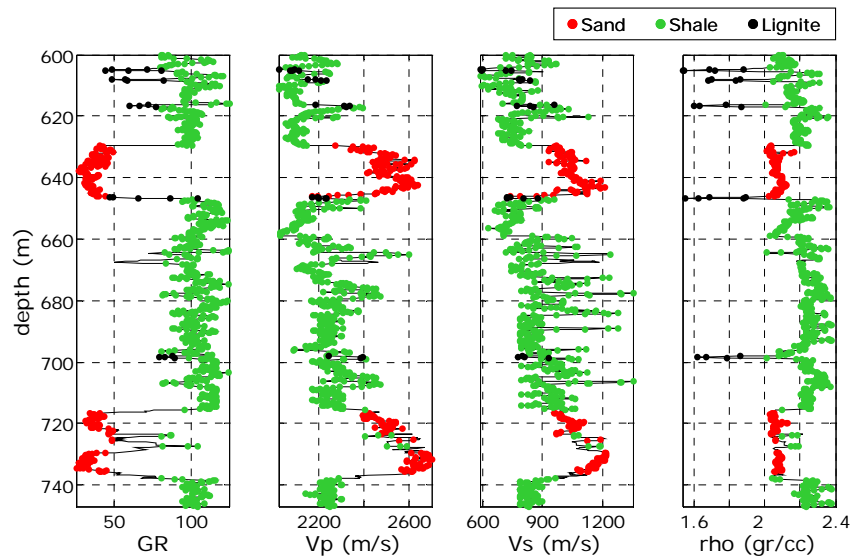


Figure 3.3: Log data of the reference well after editing, indicating with color dots the assigned lithologic group.

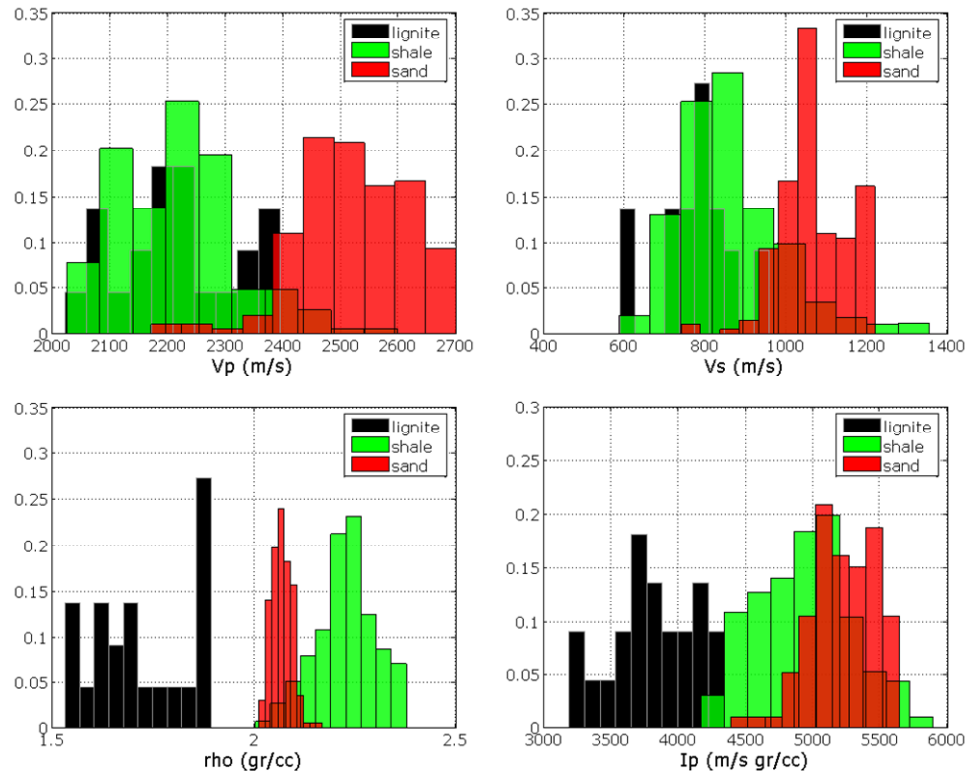


Figure 3.4: Histograms of P-wave velocity (V_p), S-wave velocity (V_s), density (ρ), and acoustic impedance (I_p) for reference well, color-coded by the *a-priori* groups.

Augmenting the number of data points

Assuming that V_p , V_s , and ρ well-log values were a good representation of the sand, shale, and lignite properties in the study area, the number of data points was augmented by drawing correlated Monte Carlo (CMC) simulations. The performed CMC simulations can be described as follows: First, linear regressions of V_p - V_s and V_p - ρ were calculated from well-log data for each group. Then, values from the V_p *cdf* (probability cumulative density function) were drawn, and using the derived regressions, the corresponding V_s and ρ values were obtained. Gaussian noise was added to each V_s and ρ simulated value to introduce the variability observed in the original data. The lignite group was treated differently. Because of the few available log samples and their dispersion, it was more reasonable to simulate each

elastic variable independently, instead of imposing an unknown correlation. Ten thousand points of V_p , V_s , and ρ were CMC simulated for each group. Figure 3.5 presents the plots V_p - V_s , and ρ - V_p of the log data and the CMC simulated points. For reference, Castagna *et al.* (1993) and Castagna’s Mudrock (Castagna *et al.*, 1985) are included in V_p - V_s plots. Similarly, Gardner’s relations for sandstone and shale, and the modified Hashin-Shtrikman upper curve are shown in ρ - V_p plots. The histograms of the elastic properties computed with the log data were compared with the equivalent histograms calculated with the CMC data values. Figure 3.6 reveals that initial the logs’ V_p , V_s , and ρ distributions were preserved after CMC simulation.

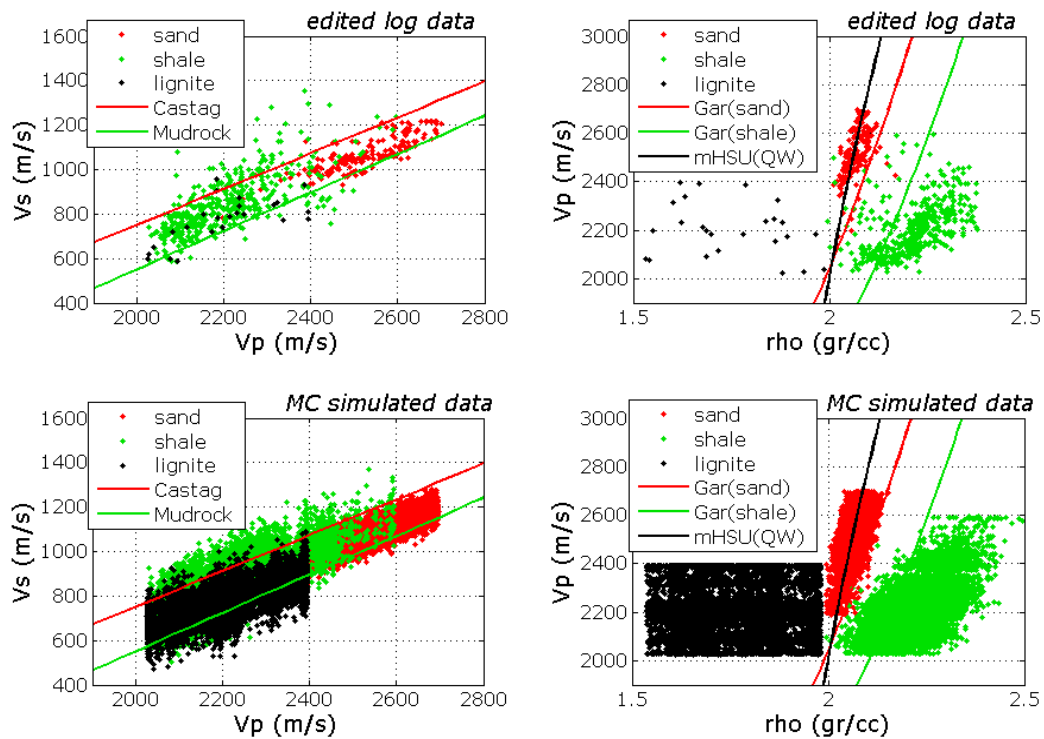


Figure 3.5: V_p - V_s and ρ - V_p plots of log data (up) and drawn correlated Monte-Carlo simulations (down), color-coded by the *a-priori* group. For reference, Castagna *et al.* (1993) and Castagna’s Mudrock (Castagna *et al.*, 1985) are included in V_p - V_s plots. Similarly, Gardner’s relations for sandstone and shale, and the modified Hashin-Shtrikman upper curve are shown in ρ - V_p plots.

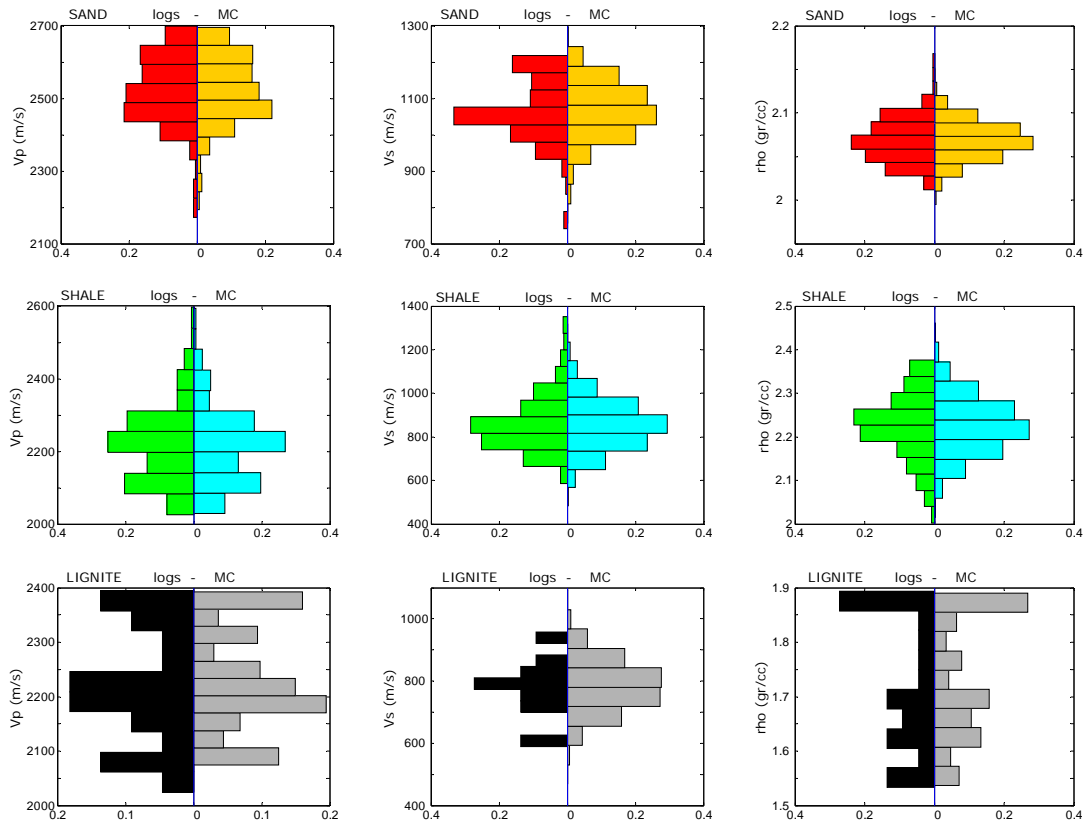


Figure 3.6: Normalized histograms of V_p (left column), V_s (center column), and ρ (right column), from log data (left histogram of each subplot) and drawn correlated Monte Carlo simulations (right histogram of each subplot), for each *a-priori* group (rows from top to bottom: sand, shale, lignite).

Attributes comparison

A set of intervallic seismic attributes was calculated for each *a-priori* defined group using the CMC-simulated V_p , V_s , and ρ data points. Then, non-parametric *pdfs* of sand, shale, and lignite were estimated in the four attribute planes considered, i.e. $\rho\lambda-\rho\mu$, $\lambda-\mu$, $I_p-IE(30)$, and PSEI(10)-PSEI(50). Finally, with the derived *pdfs*, the conditional probabilities of the true group given the predicted group were calculated. Figure 3.7 presents the plots of the analyzed pairs of attributes, computed with the CMC-simulated V_p , V_s , and ρ . As can be seen, there is a clear overlap between sand and shale points in all the PP seismic-attribute-analyzed planes. Per contra, in the PSEI(10)-PSEI(50) plane, the groups are almost completely separated.

Bayesian classification analysis was used to quantify the observed overlap-separation between *a-priori* defined groups.

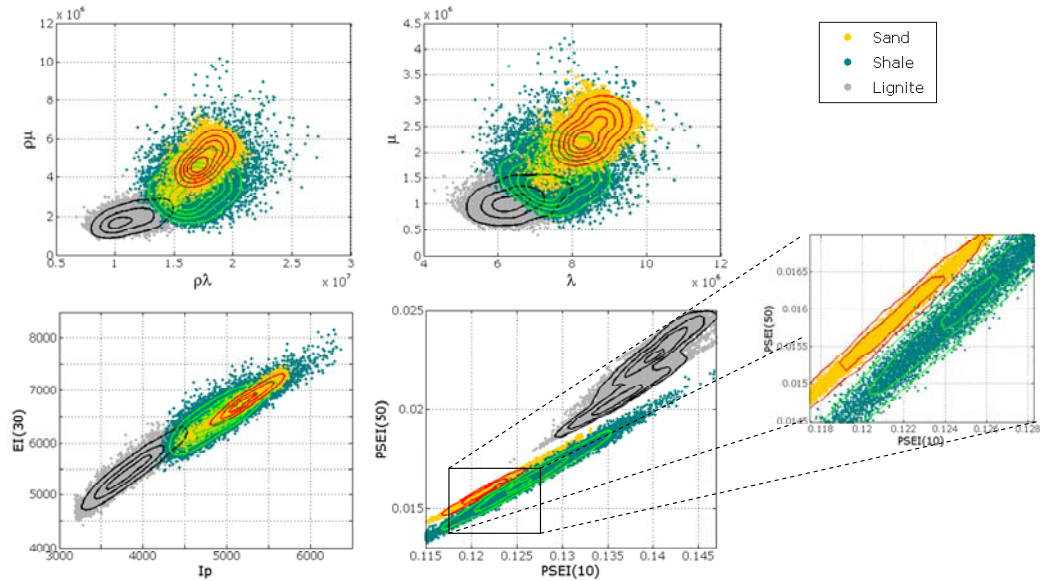


Figure 3.7: Analyzed pairs of attributes computed using CMC V_p , V_s , and ρ data points. A zoomed window (right) is presented for the PSEI(10)-PSEI(50) plot showing the separation between sand and shale points.

The elements of a Bayesian confusion matrix give the conditional probability of being the true group given a predicted group. In particular, the diagonal elements correspond to the probability of correctly predicting each group, i.e. $\text{Prob}(\text{true group} = X \mid \text{predicted group} = X)$, with X equal to sand, shale, or lignite. Figure 3.8 shows the diagonal elements of the Bayesian confusion matrix computed for the four pairs of considered attributes. It is clear that PSEI(10)-PSEI(50) is indeed the best attribute combination among those analyzed for discriminating between the three *a-priori* lithologic groups.

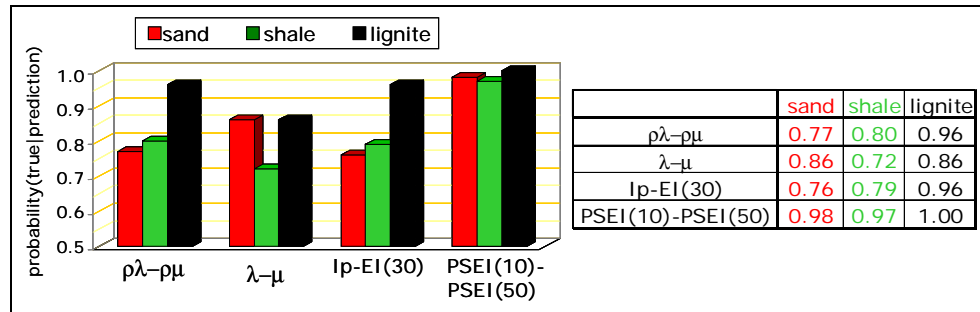


Figure 3.8: Conditional probability of the true lithologic group given the correct prediction of lithology (diagonal elements of the Bayesian confusion matrix) for the four pairs of analyzed attributes.

3.3.2 Classification test using PSEI

In the Bayesian classification approach, once the group-conditioned probabilities, $P(\text{attributes} \mid \text{group})$, are estimated with the training data, Bayes rule is used to get $P(\text{group} \mid \text{attributes})$. Then, based on these attribute-conditioned probabilities, the data can be classified, and the probability of predicting any group given some attribute values can be estimated. Figure 3.9 presents the results of applying Bayesian classification to the reference well. In this case, the values from the reference well were also used as training data. Simple visual inspection of Figure 3.9 reveals a high similarity between the *a-priori* classification based on cutoff values of GR and ρ logs, and the Bayesian classification with PSEI(10) and PSEI(50). To obtain a quantitative estimate of this observation, the Bayesian confusion matrix was calculated. Values of 0.97 and greater were obtained for the diagonal elements, as it shown in Figure 3.9.

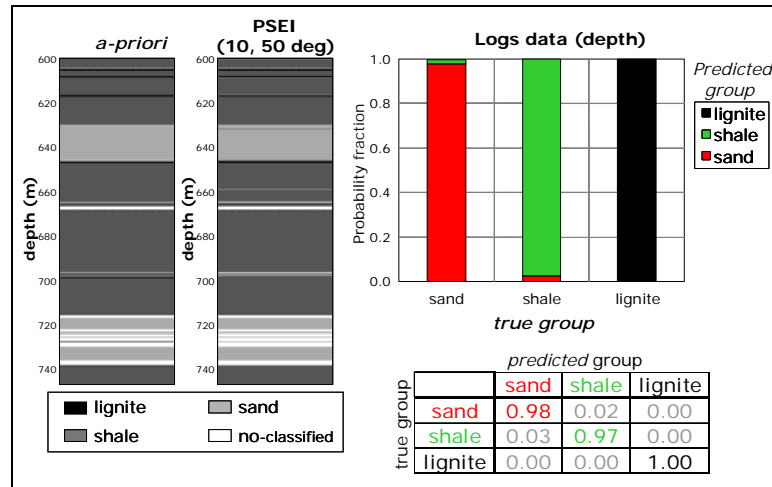


Figure 3.9: Reference well. Left: *a-priori* classification of each depth level based on GR and ρ thresholds, and the resulting Bayesian classification using PSEI(10) and PSEI(50) logs. Right: corresponding Bayesian confusion matrix.

A second well (*well 2*) was used to test the lithology identification results predicted with the reference well. *Well 2* is located 40 km from the reference well. It was edited, and a group indicator value (sand, shale, or lignite) was assigned to every sampled depth with the same cutoff values of GR and ρ logs used in the reference well. Figure 3.10 presents the *well 2* logs after editing and color-coding with the *a-priori* assigned lithologic group. Bayesian classification, using the *pdfs* estimated with training data from only the reference well, was applied to the PSEI(10)-PSEI(50) log derived values. As can be seen in Figure 3.11, for *well 2* shale and lignite are completely discriminated, but there is a 0.22 probability of erroneously predicting shale when the true lithology is sand. In terms of reserves estimation, this result indicates that sand volumes derived using PSEI will be a conservative prediction.

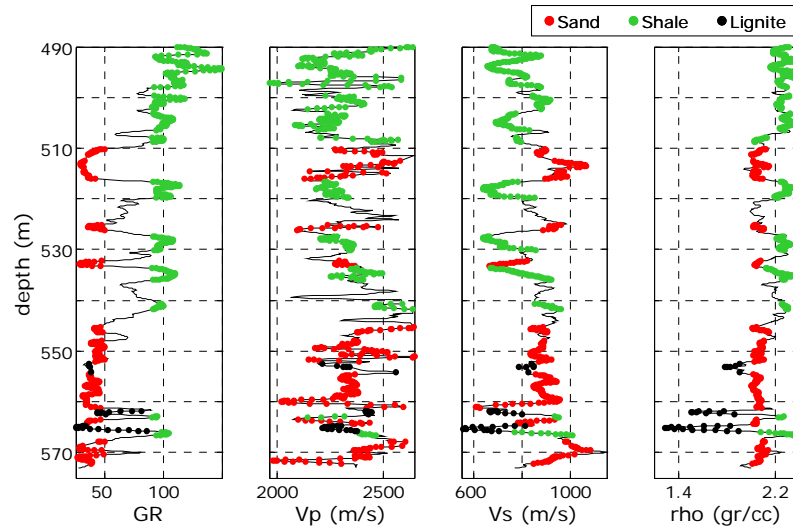


Figure 3.10: Well 2 log data (40 km from the reference well). Colors indicate the assigned lithology based on same threshold log values of GR and ρ used for the reference well.

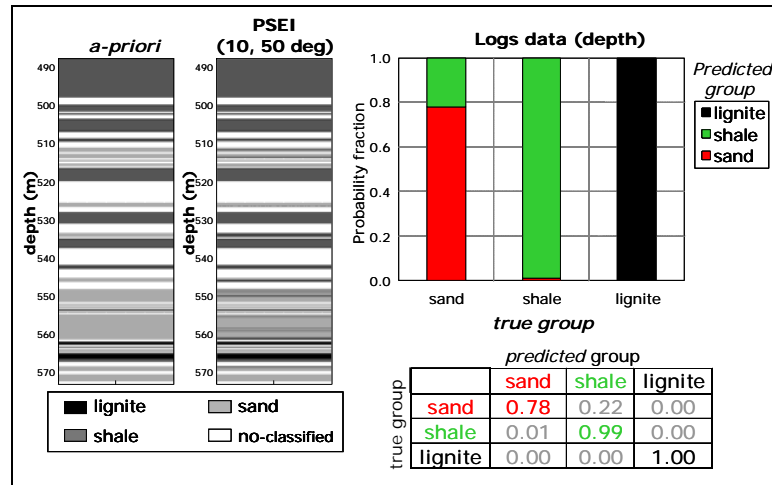


Figure 3.11: Lithologic group classification for well 2. Left: classification based on GR and ρ logs thresholds (*a-priori*), and the obtained Bayesian classification using PSEI(10) and PSEI(50) logs (*Pdfs* were estimated with training data from only the reference well). Right: corresponding Bayesian confusion matrix.

3.4 Partial gas saturation: fizz water versus commercial gas

Using well-log data, the statistical classification success rate was analyzed for discriminating fizz water using PSEI. The term fizz water was used to indicate low

gas saturations. Statistical rock physics was applied in a way similar to that described in the previous section (lithologic discrimination). Although sandstones with commercial gas and fizz water have been found in the area where the utilized well is located (showing similar PP attributes signatures), the available logs sample only fully water-saturated zones. Gassmann's equations were used to substitute in-place water with homogeneous mixtures of gas and water, covering a range of gas saturations (S_g). Elastic properties of each fluid component at reservoir conditions were calculated using the equations of Batzle and Wang (1992). Effective fluid modulus and density were calculated with Reuss and arithmetic average respectively, for water saturations ($S_w = 1 - S_g$) of 0.7, 0.5, 0.3, and 0.

The original logs and the logs resulting from fluid substitution are presented in Figure 3.12. Notice the abrupt reduction of V_p with the initial presence of a small amount of gas. This is a well-known physical phenomenon documented by Domenico in 1976, and it is the main physical limitation for identifying partial gas saturation with PP seismic data. In contrast, the density varies linearly with gas saturation. V_s does not vary much with gas saturation.

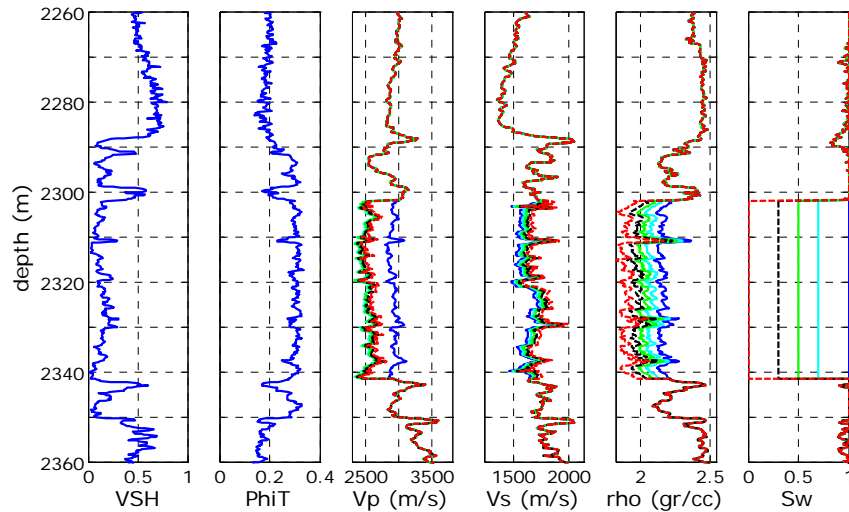


Figure 3.12: Logs from the utilized well (blue lines), and the resulting logs after fluid substitution (Gassmann) with different homogeneous mixtures of brine and gas.

PSEI values for incidence angles of (-15) and (-50) degrees were calculated with the log data from shale, original sand ($S_w=1$), and Gassmann-simulated, water-gas-saturated sands. The negative values of the angles indicate negative offsets, following the sign convention of the incidence angle and reflectivity used by Aki and Richards (1980). The constant K (average V_s/V_p) used in PSEI calculation was 0.6. In the PSEI(-15)-PSEI(-50) plane, shale points are well separated from sand for all S_w . Hence, PSEI for lithology identification is also feasible in this area. However, the important result to be emphasized here is the real possibility of discriminating between different homogeneous water or gas saturations. Values of PSEI at (-15) and (-50) degrees *monotonically increase* with reduction of gas concentration, responding to changes in density. Consequently, this combination of seismic attributes has the potential to differentiate between different water-gas proportions, homogeneously mixed.

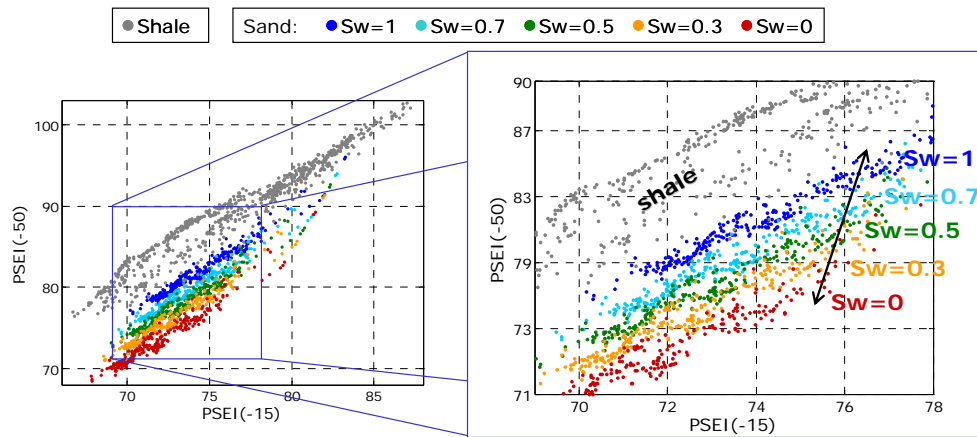


Figure 3.13: PSEI for incidence angles of (-15) and (-50) degrees computed with the well log values from shale and sand with $S_w = 0, 0.3, 0.5, 0.7,$ and 1 .

The number of log data points was augmented by applying correlated Monte Carlo (CMC) simulation, and the corresponding *pdfs* for all modeled S_w situations were computed. The Bayesian confusion matrix was calculated to quantify the observed separation of sands with different S_w in the PSEI(-15)-PSEI(-50) plane. Figure 3.14 presents the complete Bayesian confusion matrix obtained. The plotted

bars indicate the probability of predicting any group for a given true group, i.e. each bar corresponds to one row of the confusion matrix. In this case, analyzing only the diagonal elements can lead to incorrect conclusions. Off-diagonal elements are also very important, as they describe the probability of different types of misclassification errors, and hence are valuable inputs for risk analyses. Ideally, the off-diagonal elements should be small and need not be symmetric. As can be seen in Figure 3.14, the significant probabilities of misclassification in all Sw cases studied only extend to the immediate smaller or larger Sw group considered. This means that the uncertainty associated with estimating a specific single value of Sg from PSEI is high. However, PSEI can discriminate with errors smaller than 5% between sands with low Sg and with med-high Sg.

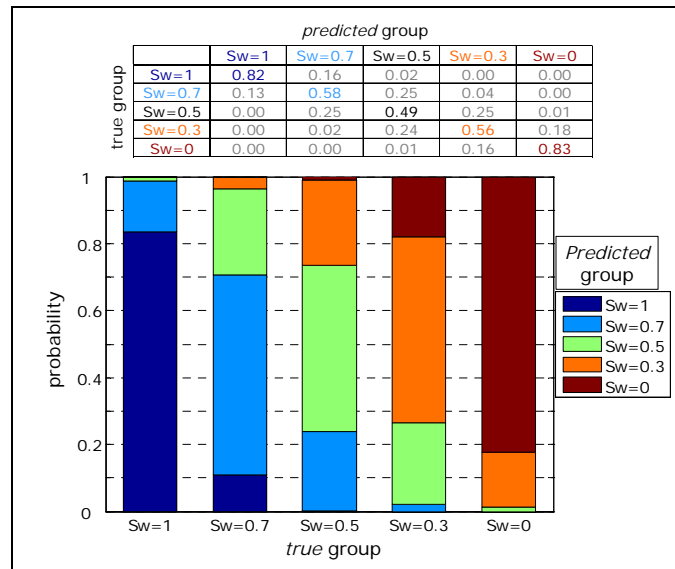


Figure 3.14: Bayesian confusion matrix values (top) and their representation in vertical bars (bottom). Each bar corresponds to a row of the confusion matrix, i.e. the probability of predicting any of the groups (colors) when the true group is the one indicated in the abscissa.

To compare the utility of a group of seismic attributes for discriminating between “fizz water” ($0.1 < S_g < 0.2$), and “commercial gas concentrations” ($S_g > 0.5$), statistical rock physics was applied. In this case, two groups were defined *a-priori*

(fizz water and gas). Figure 3.15 shows the diagonal elements of the Bayesian confusion matrix for each pair of attributes analyzed. It reveals that in this case, amid the pairs of attributes compared, PSEI(-15)-PSEI(-50) is the best for distinguishing fizz water from commercial gas. Using only PS elastic impedances, errors smaller than 10% are predicted when attempting to distinguish between the two defined groups.

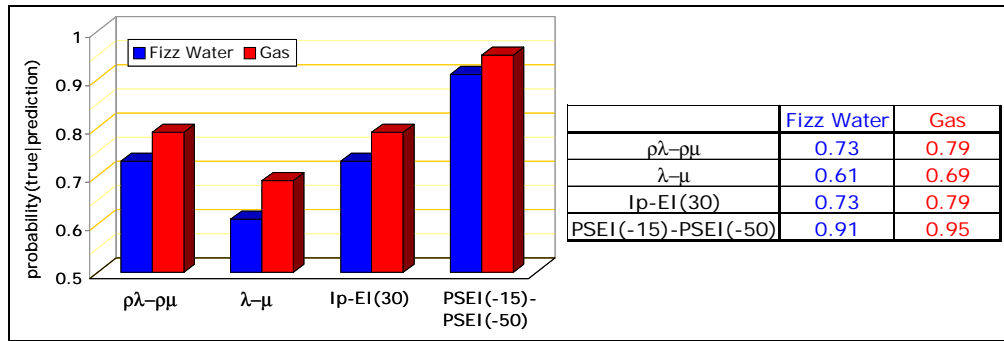


Figure 3.15: Conditional probability of the true group (fizz water, commercial gas) given the prediction (diagonal elements of the Bayesian confusion matrix) for the four pairs of attributes studied.

3.5 Conclusions

Applying statistical rock-physics methods to real well-log data, it was shown that, combining PSEI for two angles, it is possible to discriminate between lithologies with similar acoustic impedance and to identify different gas concentrations. The methodology used made it possible to determine not only the best attribute in the two analyzed cases, but also estimate the uncertainty associated with the predictions.

PSEI(10)-PSEI(50) is the best pair of attributes for discriminating lithology, compared with: $\rho\lambda-\rho\mu$, $\lambda-\mu$, I_p -EI(30). This result, obtained with log data for particular wells, can be extended to lithologies in clastic reservoirs with small acoustic impedance contrasts, but differences in densities. The feasibility of discriminating between sand, shale, and lignite in the study area was validated using a second well, 40 km from the reference well. For predicting lithology in the second well with PSEI, the classification system (*pdfs*) was generated using only the training

data from the reference well. Shale and lignite were completely discriminated, and there was only a 0.22 probability of erroneously predicting shale when the true lithology was sand. In terms of reserves estimation, this result indicates that sand volumes derived using PSEI would be a conservative estimate.

It was shown that PSEI values *monotonically* decrease with incremental increases of gas saturation in a homogenous gas-water mix, for negative offsets. Consequently, it is possible to discriminate between fizz water and commercial gas concentration using PSEI. In the studied case, combined use of PSEI for (-15) and (-50) degree incidence angles improves by about 20% the probability of successfully distinguishing commercial gas concentrations from fizz water, compared with the other PP seismic attributes analyzed.

One remarkable advantage of using two PSEI attributes (e.g. near and far offsets), instead of a combination of PP and PSEI is that the time and amplitude matching of PP and PS data is avoided for the interpretation. An important question that arises after this work is how the “noise” in the seismic data (either processing artifacts or random noise) affects the PSEI values or distributions. The answer is the key to anticipate the areas where the discriminator potential of PSEI can be exploited.

Chapter 4

Practical procedure for P-to-S seismic data inversion

“Simplicity is the ultimate sophistication”

(Leonardo da Vinci)

4.1 Abstract

This chapter presents a method for obtaining P-to-S elastic impedance (PSEI) from P-to-S (PS) seismic data using PP stratigraphic inversion software. Additionally, the validity of some of the approximations assumed in the proposed method is addressed. PSEI can be a good lithologic discriminator as well as a good indicator of partial gas saturation because of its monotonic relationship with density. Three examples with synthetic traces are presented to show the feasibility of obtaining PSEI values using the same principles as those of PP data inversion. In the first example, PS synthetic traces from a set of three-layer models are inverted to obtain PSEI using a probabilistic approach. Having total control of the inversion process allowed me to verify that the convolutional model approximation is a valid approach when inverting PS data. Then, a methodology to derive PSEI from PS data using commercial PP stratigraphic inversion software is proposed and applied in two synthetic examples, based on real well-log data. The method is based on generating

a pseudo-velocity and a pseudo-density log, sampled at pseudo-depth units. The technique exploits the similar functional expression of acoustic impedance and PSEI. Rather than developing new inversion algorithms, the objective of this chapter is to show the viability of a practical procedure to compute PSEI from PS seismic data.

4.2 Introduction

The previous chapter showed that P-to-S elastic impedance (PSEI) can discriminate lithologies with small acoustic and Poisson contrast, and differentiate between fizz water and commercial gas concentrations. In the previous chapter's feasibility analyses, PSEI values computed with P-velocity (V_p), S-velocity (V_s), and density (ρ) logs were used. However, the final goal is to be able to extrapolate the results to the seismic data. The value of a well-log-based feasibility study is based on its capability to extrapolate the results obtained at the wells to the area covered by seismic information. Consequently, it is important to analyze quantities or attributes that can be computed with V_p , V_s , and ρ logs as well as extracted from the seismic. In the context of this chapter, a well-log-based feasibility study, showing that PSEI responds to changes in the reservoir property of interest, suggests a consequent computation of PSEI from PS processed data. In practice, the inversion of PS data for PSEI can be done using the same algorithms and programs developed for P-to-P (PP) inversion.

PSEI is an attribute that depends on the incidence angle; therefore, the inversion has to be target-oriented. Variations of both the wavelet and the angle-to-offset transformation constrain the range of validity of the inversion. In principle, a single PS trace is needed to obtain PSEI at a given angle. However, in practice the input for the inversion could be a stack of traces in a limited range of offsets, to increase the signal-to-noise ratio.

A seismic trace can be modeled as the convolution of the reflectivity series with a wavelet. The reflectivity series is defined as the ratio between the difference and the sum of the impedances between consecutive depths. Most of the available PP stratigraphic inversion software relies on convolution to perform the forward

modeling, because it is a relatively fast operation. For PS traces at a given incidence angle (θ), the reflectivity can be defined in terms of PSEI(θ). As when inverting PP data, the wavelet has to be extracted from the data itself. These assumptions—i.e. validity of the convolutional model with the reflectivity defined from PSEI(θ), and the extraction of the correct wavelet—open the possibility of using already available stratigraphic inversion software to derive PSEI(θ) from PS seismic traces.

In this chapter, three examples with synthetic PS traces are used to show the feasibility of obtaining PSEI values using the same principles as for PP inversion. The first example consists of a set of three-layer models in which the thickness and water saturation (S_w) of the reservoir vary. The inversion is done using a probabilistic Monte-Carlo approach, relying on convolution for the required forward modeling. For the second and third example, synthetic PS data generated from real well-log data is used. Additionally, a methodology to obtain PSEI from PS data using commercial PP stratigraphic inversion software is presented. The proposed method is applied in the second and the third example. The objective of this chapter is to show the viability of inverting PS data to obtain PSEI, and to describe a practical method to accomplish it.

4.3 Example 1: Three layers models

A set of three-layer models were built using realistic values of V_p , V_s , and ρ . Thicknesses of the top layer and the complete model, as well as the elastic properties of top and bottom layers, are kept unchanged for all models. A total of 55 models were created, changing the thickness and elastic properties of the reservoir (middle layer). Thickness varies from zero to 100 meters, by ten-meter increments, yielding eleven variations. Five values of elastic properties are used corresponding to different fractions of brine and gas, homogeneously mixed. The water proportions selected are 0, 0.3, 0.5, 0.7, and 1. Figure 4.1 shows the set of models (variations of reservoir S_w) with reservoir thickness of 100 meters and the five S_w variations.

The synthetic PS traces (horizontal component) were computed for each model independently. Each trace was generated using the available implementation of

Kennett's method (Kennett 1980, 1985) in the "AVO modeling" (version 5.5) software of Hampson and Russell. Kennett's method gives the full elastic response of a stack of homogenous layers. The traces were calculated for an offset such that the incidence angle at the top of the reservoir layer was approximately (-50) degrees. The minus sign of the angle indicates negative offsets, following the sign convention of Aki and Richards (1980). A Ricker wavelet with central frequency of 40 Hertz was used as input for the modeling. Figure 4.2 presents the synthetic traces (data traces) generated for the models with reservoir Sw equal to one and equal to zero. The first trough and last peak of each trace were picked to obtain the approximate times of the top and bottom interfaces.

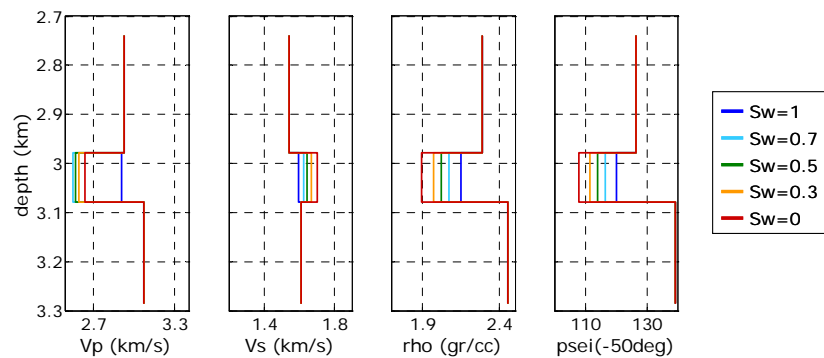


Figure 4.1: Elastic properties and derived PSEI(-50°) for the variations of Sw in the reservoir with thickness of 100 meters.

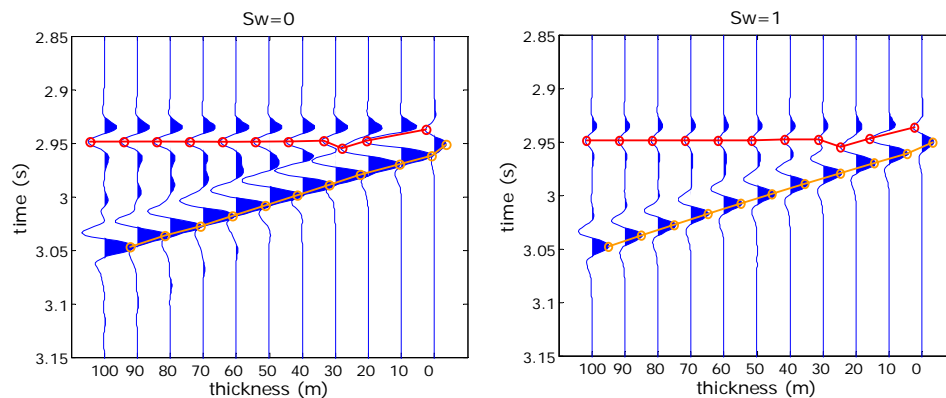


Figure 4.2: Synthetic traces ($\theta=-50^\circ$) for the models with reservoir Sw=0 (left) and Sw=1 (right), and the picked horizons used as input information for the inversion.

For this example, a probabilistic approach was used to invert the synthetic PS traces for PSEI(-50°). Any inversion problem can be expressed as follows (e.g. Tarantola, 2005):

$$\gamma(\mathbf{m}) = \text{const } \varphi(\mathbf{m})\varphi(\mathbf{g}(\mathbf{m})), \quad (4.1)$$

where $\varphi(\mathbf{m})$ and $\chi(\mathbf{m})$ are the *prior* and the *posterior* probability densities (*pdf*) in the model space, $\varphi(\mathbf{g}(\mathbf{m}))$ is the likelihood which includes the observed data and the uncertainty or error associated with each value, and $\mathbf{g}(\mathbf{m})$ is a function that solves the forward problem, i.e. the forward model operator that links the model space with the data space.

The inversion was done trace-by-trace in the time domain. The parameters to invert for, i.e. the elements of the model space, were the times of the top and the bottom interfaces, and PSEI(-50) of the three homogenous layers. One of the models was assumed to be known before the inversion. That is, a single “well” was available, sampling the model in which the reservoir is 100 meters thick and fully water saturated. The prior knowledge about the parameters, i.e. $\varphi(\mathbf{m})$, was basically derived from the “well”. As Tarantola (2005) points out, the *prior pdf* not need be defined in a closed form; it can be specified by giving a set of rules. For the case of study, the *prior pdf* was defined with the following conditions for the elements of the model space:

- 1) Prior knowledge of the interface times:
 - a) If the number of samples between the picked horizons is greater than or equal to 20, then the interface times are drawn from uniform *pdfs* centered at the picked times and ranges of 10 samples.
 - b) Otherwise, the *prior pdfs* for the times of the horizons are truncated double exponential *pdfs* with means of five samples and maximum variation of 20 samples.
- 2) Prior knowledge of PSEI values of top and bottom layer: truncated Gaussian *pdfs* with means equal to the PSEI values observed at the “well”, and standard and maximum variations of one percent and five percent of the means.

3) Prior knowledge of reservoir PSEI: uniform *pdfs* within $\pm 15\%$ of the value observed at the “well”.

The likelihood $\varphi(\mathbf{g}(\mathbf{m}))$ was an L1-norm type of function, defined by a constant multiplied by $\exp(-\sum |\mathbf{d}_{\text{obs}} - \mathbf{d}_{\text{cal}}|/\omega)$, where the summation (\sum) is over all the samples of the trace. In the likelihood function, \mathbf{d}_{obs} corresponds to the observed data, i.e. the PS input trace, \mathbf{d}_{cal} is the PS trace computed with convolution, and ω is a weighting factor that controls the severity of the comparison. ω was chosen as half of the difference between the samples of data trace at the “well” location and trace generated with convolution at the same position. The selection of ω was based on a measure of the ability to reproduce the observed data at a location (well) where the solution was known.

As was mentioned before, the data (\mathbf{d}_{obs}) was generated using a full waveform modeling for horizontally homogeneous layers. On the other hand, convolutional modeling was the forward operator for the inversion. The motivation for using convolution for computing \mathbf{d}_{cal} was to show the applicability of the standard convolution-based inversion approach. Figure 4.3 shows one of the data traces (full-wave modeling), and the equivalent trace computed by convolving the PSEI-derived reflectivity with two different wavelets. In one case, the wavelet was a Ricker of 40 Hertz, which is the same used as input for generating \mathbf{d}_{obs} . The other wavelet used in Figure 4.3 was extracted from the data traces. As can be noticed, convolving the original wavelet (Ricker) with the reflectivity derived from PSEI does not reproduce the data trace. Per contra, when using the extracted wavelet for the convolution, an excellent match between \mathbf{d}_{obs} and \mathbf{d}_{cal} is obtained. As was expected, this shows the importance of selecting an appropriate wavelet for the inversion.

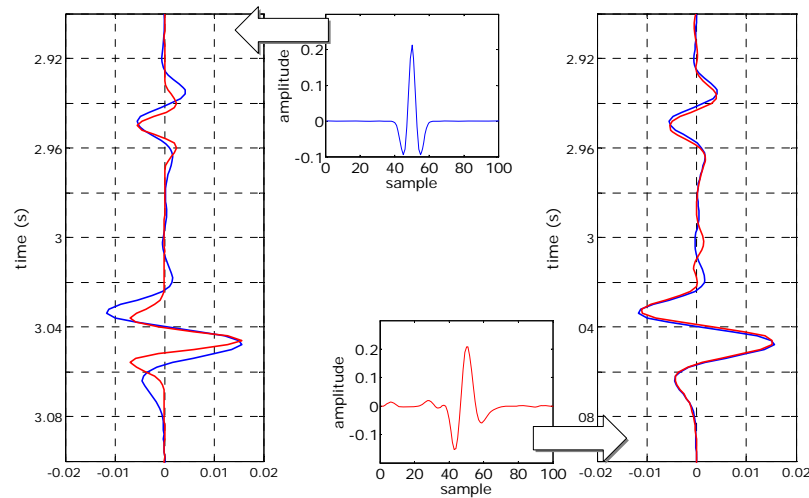


Figure 4.3: Traces computed using full wave modeling (blue) and convolution (red) of the reflectivity derived from PSEI, and the two wavelets: 40 Hz Ricker wavelet (center-left), and wavelet extracted from the full wave modeled trace (center-right).

The Metropolis algorithm was applied to the sample from the *posterior* $\chi(\mathbf{m})$. Figure 4.4 shows one set of particular solutions, specifically the ones where $\chi(\mathbf{m})$ was maximum. As can be seen, the times of both horizons and the constant values of PSEI for top and bottom layers were well estimated. The obtained values of PSEI for the reservoir clearly reproduce the trend with Sw of the input models. This is only one possible solution that, because of the simplicity of the problem, reasonably gives the expected answer. In general, the complete solution must be explored by drawing and visualizing many models from $\chi(\mathbf{m})$, analyzing some of marginal probabilities (parameters of interest), or computing different statistics for some of the parameters (Tarantola, 2005). Results of Figure 4.4 reveal that it is feasible to obtain PSEI from PS data, and hence estimate Sw , based on the same principles commonly used to invert PP data.

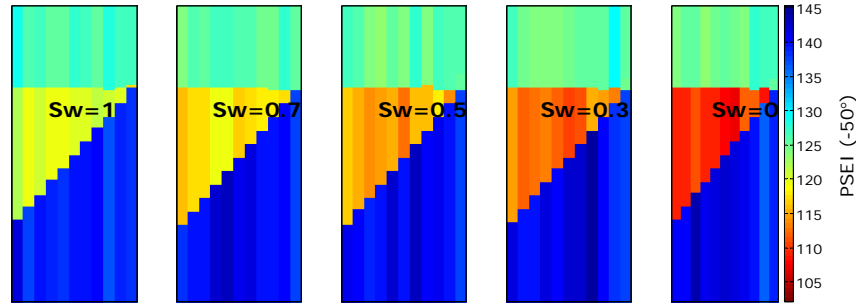


Figure 4.4: One possible solution (maximum *a-posteriori*) or model for each trace selected from the *posterior pdf*.

4.4 Example 2: PSEI from PS data using PP stratigraphic-inversion software for discriminating lithology.

Specific well-log manipulation is required for obtaining PSEI from PS seismic data using commercial PP stratigraphic-inversion software. Commonly, inversion programs build the initial model based on the acoustic impedance calculated with V_p and ρ logs. I propose to generate pseudo-velocity (pseudo_V) and pseudo-density (pseudo_ρ) logs for constructing the initial model. That is basically the same principle used to invert non-zero offset PP data for computing elastic impedance (e.g. Connolly, 1999). The new pseudo-logs need to be sampled in pseudo-depth (pseudo_z) units, such that the inversion software attains consistency in the time-to-depth conversion and between log PSEI values and PS data. The goal is to exploit the similar functional relation between acoustic impedance and PSEI, with the corresponding velocities and densities. The pseudo-logs should satisfy the following two conditions:

$$(\text{pseudo_V})(\text{pseudo_}\rho) = \rho^c V_s^d, \quad (4.2)$$

$$(\text{pseudo_z}) = \frac{1}{2}(\text{pseudo_V})(\text{PStime}), \quad (4.3)$$

To fulfill equations 4.2 and 4.3, pseudo_V, pseudo_ρ, and pseudo_z can be defined as follows:

$$\text{pseudo_}\rho = \rho^c, \quad (4.4)$$

$$\text{pseudo_V} = V_s^d, \quad (4.5)$$

$$\text{pseudo_z} = \frac{z}{2} \left(\frac{1}{V_p} + \frac{1}{V_s} \right) \text{pseudo_V}, \quad (4.6)$$

with exponent c and d given by:

$$c = \frac{K \sin \theta_p}{\sqrt{\frac{1}{K^2} - \sin^2 \theta_p}} \left(2 \sin^2 \theta_p - \frac{1}{K^2} - 2 \cos \theta_p \sqrt{\frac{1}{K^2} - \sin^2 \theta_p} \right), \quad (4.7)$$

$$d = \frac{4K \sin \theta_p}{\sqrt{\frac{1}{K^2} - \sin^2 \theta_p}} \left(\sin^2 \theta_p - \cos \theta_p \sqrt{\frac{1}{K^2} - \sin^2 \theta_p} \right). \quad (4.8)$$

For the second example, the well-logs from one of the wells (*reference well*) presented in the previous chapter were used. Before generating the synthetic PS traces for the inversion, a (fast) ray-tracing algorithm was used to determine the source-receiver offsets corresponding to approximately 10 and 50 degrees of incidence angle. Although a single offset does not strictly correspond to a single incidence angle, based on the ray tracing modeling (Figure 4.5), it was established that for the interest zone, offsets of 150 and 900 meters approximately correspond to incidence angles of 10 and 50 degrees, respectively. Using a Kennett's method, the PS synthetic traces for the inversion were generated. The wavelet used was a Ricker with a 60 Hertz central frequency.

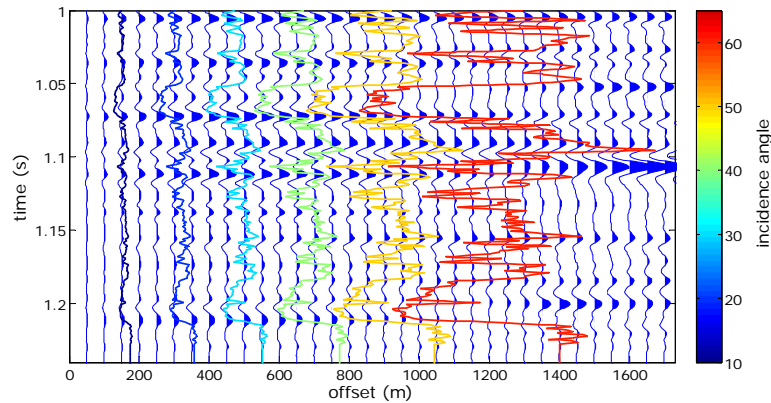


Figure 4.5: Synthetic PS traces (ray tracing algorithm) for offsets between 0 and 2000 m. Color lines are contours for constant incidence angle (P-wave incidence angle).

Figure 4.6 shows the *reference well* PSEI logs for incidence angles of 10 and 50 degrees respectively, calculated with the original V_s and ρ logs. Additionally, derived with equations 4.4, 4.5, and 4.6, pseudo- V_s and pseudo- ρ logs sampled in pseudo-depth units are presented.

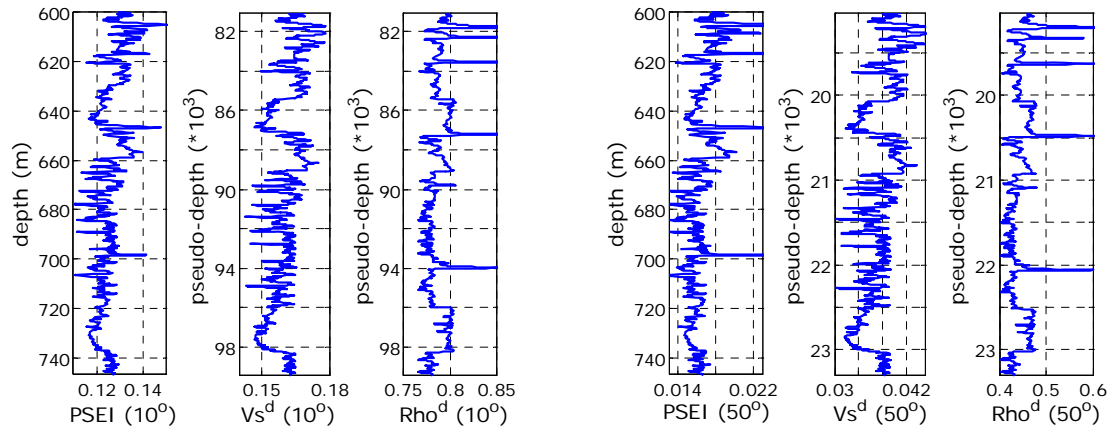


Figure 4.6: PSEI calculated logs, and pseudo-velocity and pseudo-density, sampled in pseudo-depths, for incidence angles of 10 and 50 degrees.

The standard procedure for inverting PP seismic traces was applied; with the variation that the initial model was built using the well-logs computed with equations 4.4, 4.5, and 4.6. The model based inversion option of the commercial software “Strata” (version 5.5) by Hampson and Russell was used. Figure 4.7 presents 10 and 50 degrees PSEI values calculated from the logs and inverted from the synthetic traces. As was expected, there is a clear similarity between PSEI from logs and synthetic seismic. However, the inversion was not able to reproduce the high values associated with lignite, principally due to their small thickness. Additionally, it can be seen how inverted PSEI presents a blocky aspect with average thickness of three samples. The blocky appearance of the result is a characteristic of the model-based inversion algorithm. The average size of the layers or blocks is parameter defined by the user. It is important to remark that the objective of this test is neither to compare inversion algorithms nor to optimize their input parameters. The goal is to show the viability of the process and the steps to complete it.

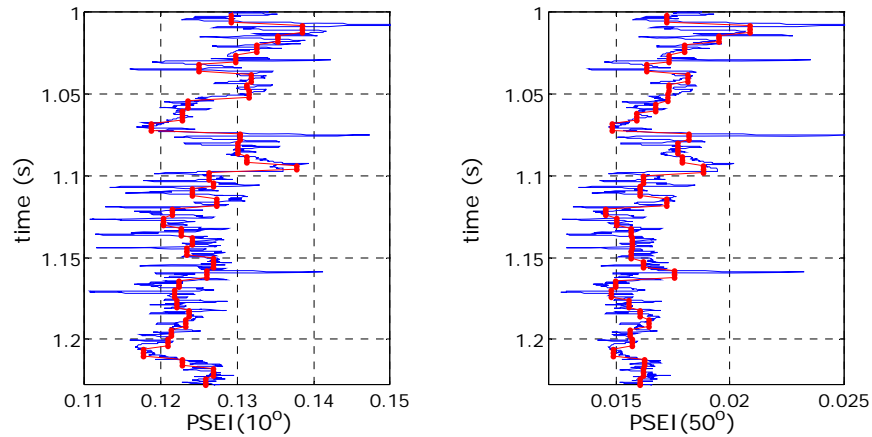


Figure 4.7: PSEI for incidence angles of 10 (left) and 50 (right) degrees calculated using log data (blue) and obtained from the inversion of the PS synthetic traces.

Following the methodology presented in the previous chapter, the PSEI profiles obtained from the inversion of the synthetic traces were classified using a Bayesian scheme. The conditional probabilities for the classification were computed using only the well-log data from the *reference well*. In a real case with enough logs and seismic data, the *pdfs* calculated from logs must be scaled using surrounding inverted traces. The probability distributions required for the Bayesian classification, or in general for any classification system, must be similar in scale to the values to be classified.

Figure 4.8 illustrates the results of the Bayesian classification. The problem with the lignite layers is their small thickness. Nevertheless, the Bayesian confusion matrix indicates that the lignite group is principally confused with shale, which for practical purposes does not affect the main goal of identifying the sand bodies. Elements of the sand group have a 0.24 probability of being identified as shale, i.e. missing sand bodies. On the other hand, there is only a 0.09 probability of predicting sand when the true layer is shale, that is, of erroneously drilling shale.

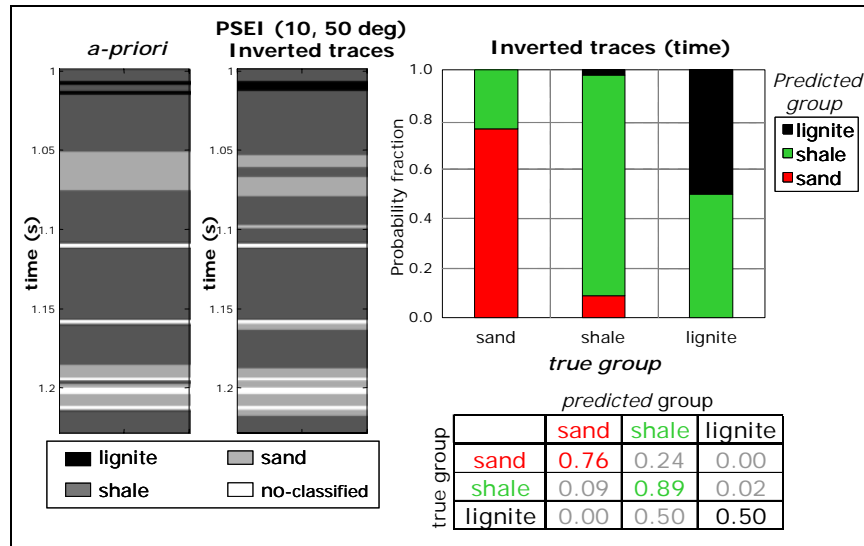


Figure 4.8: Bayesian classification results for *reference well* inverted synthetic seismic, using the conditional *pdfs* obtained from the logs. Left: *a-priori* and the result from the Bayesian classification lithologic indicator for each time level. Right: Resulting Bayesian confusion matrix.

4.5 Example 3: PSEI from PS data using PP stratigraphic-inversion software for identifying partial gas saturation.

The same real well logs analyzed in the previous chapter to show the PSEI capabilities for identifying partial gas saturation were used in the third example. As was mentioned before, the well only sampled sandy bodies that were fully water saturated. Gassmann fluid substitution was done in a portion of the sandstones, which have shown gas in other wells in the area. Four different homogeneous mixtures of gas and brine were used as the replacing fluid, with the following brine proportions ($S_w=1-S_g$): 0.7, 0.5, 0.3, 0. Figure 4.9 shows the original logs, the Gassmann computed logs, and PSEI logs calculated for incidence angles of (-25) and (-50) degrees. Negative angles indicate negative offsets, following the Aki and Richards (1980) sign convention. As can be seen, PSEI monotonically decreases with increasing gas concentration, i.e. reduction of brine.

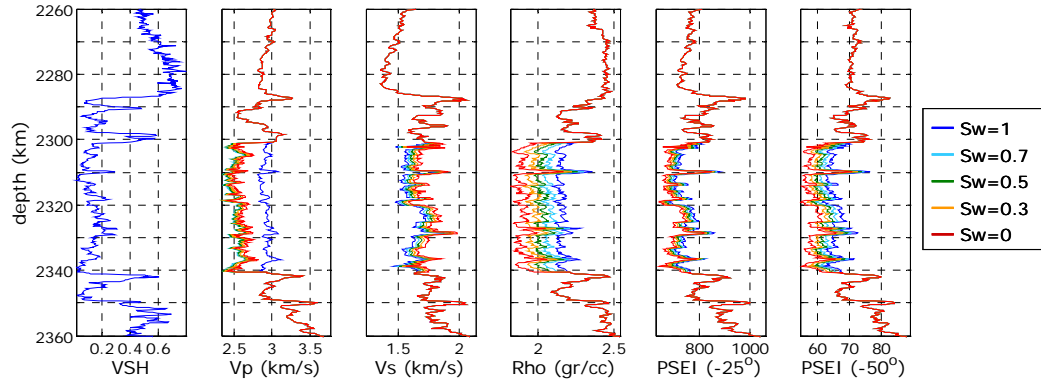


Figure 4.9: Original logs (blue lines) and computed logs (Gassmann) simulating fluid substitution with four different water (S_w) and gas ($1-S_w$) saturations.

Synthetic PS traces were generated using Kennett’s full-waveform method. Each laterally homogenous elastic model was constructed with V_p , V_s , and ρ logs corresponding to a particular S_w in the reservoir. The input wavelet was a 40 Hertz Ricker. Figure 4.10 presents the pseudo-logs computed with equations 4.4, 4.5, and 4.6, for incidence angles of (-25) and (-50) degrees, and S_w of 1, 0.7, 0.5, 0.3 and 0.

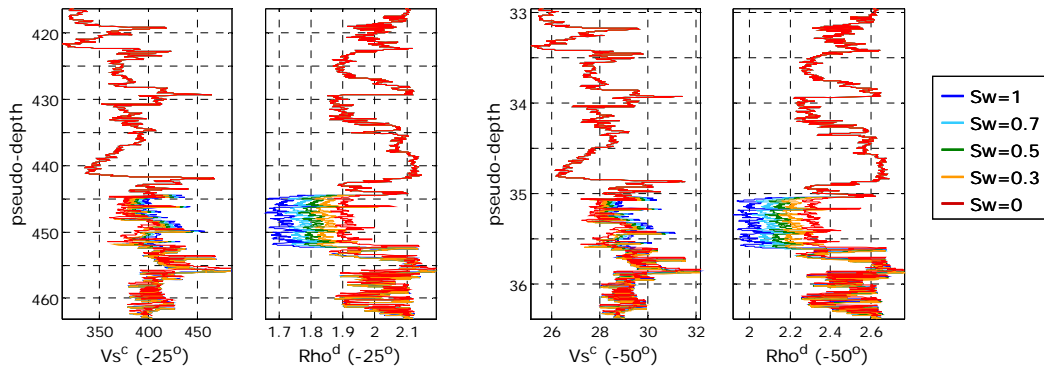


Figure 4.10: Computed pseudo-logs sampled at pseudo-depths for $\theta=(-25)$ deg. (left) and $\theta=(-50)$ deg. (right). Colors indicate S_w .

Based on ray tracing, it was established that for the zone of interest, offsets of 1200 and 2800 meters correspond approximately to angles of 25 and 50 degrees, respectively. The same standard procedure for inverting PP seismic traces mentioned in the second example was applied to the synthetic PS traces with offsets

of 1200 and 2800 m. Figure 4.11 shows the results of the inversion at the reservoir level (in time). One can notice the trend of decreasing PSEI values as the gas saturation increases. The goal of this example, as the previous one, was to show the viability of the process and a practical way to accomplish PSEI inversion using existing, off-the-shelf PP software.

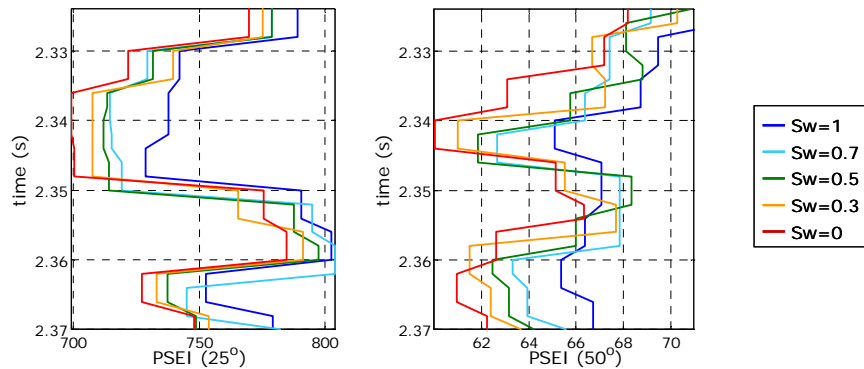


Figure 4.11: Inverted PSEI (reservoir level) for $\theta_p = -25$ degrees (left) and -50 degrees (right), color-coded by S_w (as S_g increases, i.e. S_w decreases, PSEI values tend to decrease).

4.6 Conclusions

The viability of inverting PS data for PSEI values using the same principles as used in PP data inversion was shown using three examples with synthetic traces. A procedure for inverting PS data using commercial PP stratigraphic inversion software was presented. The main step is to build the initial model with generated pseudo-velocity and pseudo-density logs, sampled in pseudo-depth units. The obtained results, in terms of the residuals, were as good as the inversion of PP data for acoustic impedance. The results were more sensitive to which algorithm was used for the inversion than whether PS data was used to obtain PSEI. It is recommended performing synthetic tests like the ones presented in this chapter, but tailored to the specific case study, to analyze the impact of the algorithm and the wavelet selected on the inversion results for both PP and PS data.

Chapter 5

Inversion method combining rock physics and multiple-point geostatistics

“The mere formulation of a problem is far more essential than its solution, which may be merely a matter of mathematical or experimental skills. To raise new questions, new possibilities, to regard old problems from a new angle require creative imagination and marks real advances in science.” (Albert Einstein)

5.1 Abstract

In this chapter, a new inversion technique that combines rock physics and multiple-point (*MP*) geostatistics in a Bayesian framework is presented. Although the proposed method is presented here in terms of reservoir characterization, it can be applied in its current implementation to any inverse problem that can be approximated as a series of unidimensional forward-modeling operators.

Rock-physics principles are incorporated at the beginning of the process, defining the links between reservoir properties (e.g., lithology or saturation) and physical properties (e.g., compressibility or electrical conductivity). Specifically, for

inverting normal-incidence seismic data (the acoustic case), which is the implementation presented in this chapter, a *group* is a reservoir property or combination of properties, such as lithology and/or fluids, with an associated distribution of velocities and densities. Multiple-point simulation (*MPS*) or multiple-point geostatistics is used to define and explore the space of solutions. In spite of the fact that the inversion method is not restricted to any particular multiple-point statistical technique, a variation of the stochastic simulation with patterns, or SIMPAT (Arpat, 2005) was used.

The solutions given by the inversion technique proposed in this chapter are multiple realizations of spatial distributions of *groups* consistent with the available well data, seismic data, and the geological concept imposed by the multiple-point geostatistical algorithm through the training image. The method can be extended to satisfy multiple physical constraints simultaneously; in other words, the solutions can be conditioned with different types of geophysical data.

5.2 Introduction

The transformation of any geophysical data into physical properties of the Earth (like elastic parameters) can be posed as an inverse problem. In seismic methods, elastic properties are inferred by inverting travel times and amplitudes of the elastic waves propagated through the subsurface. However, the goal of using geophysical methods usually goes beyond estimating the physical quantity to which the technique responds. Rather, the final goal usually is to infer characteristics of the rocks (lithology, fluid, porosity, etc.) or the regime of physical conditions (pressure, temperature, etc.) to which they are subjected.

Seismic reflection data is used in reservoir characterization not only for obtaining a geometrical description of the main subsurface structures, but also for making predictions of properties such as lithologies and fluids. Transforming seismic data to reservoir properties is an inverse problem with a non-unique solution. Even in the utopian situation of data without noise, the limited frequency of recorded seismic waves makes the solution non-unique. The inversion of seismic data for reservoir

properties gets more complicated in practice, because of the always-present noise in the data and the forward modeling simplifications needed to obtain solutions in a reasonable time.

The first techniques for predicting reservoir properties from seismic data were exclusively based on the interpreter's ability to identify patterns (Balch, 1971; Taner *et al.*, 1979; Possato *et al.*, 1983). After those initial qualitative methods, several quantitative approaches were developed to transform seismic data into reservoir properties. Some of the methods are based on defining linear relations between an average of a reservoir property observed in well logs and a characteristic or attribute of a piece of the seismic signal (Tonn, 1992; Matteucci, 1996). As an important extension of the simple linear regression, geostatistical techniques, such as cokriging, have been integrated in the analysis to account for spatial correlations (Doyen, 1988; Russell *et al.*, 2001). In addition, neural networks have been used as a way to include non-linear correlations between seismic attributes and reservoir properties (Ronen *et al.*, 1994; Banchs and Michelena, 2000). The reservoir properties predicted with direct relations between attributes of the seismic signal and reservoir properties usually correspond to a range of depths on the order of a seismic wavelength; however, the type of average and the type of homogeneity assumed are commonly not well-defined parameters.

Removing wave propagation, or more precisely, removing the wavelet from the seismic data, makes it possible to define better the zone of the subsurface to which a particular section of the seismic trace is responding. Removing the wavelet from the seismic signal is equivalent to transforming the seismic data into elastic-property values; this is the process generally known as seismic inversion. The values of the elastic properties derived are associated to a specific depth or time; therefore, the transformation from elastic to reservoir properties can be done point-by-point. Variations of the linear-regression, geostatistical and neural-network techniques previously mentioned can be used for the one-to-one conversions without understanding the physical bases of the transformations. However, accepting any statistical correlation regardless of the physics underlying the calibration can easily

yield erroneous results (Kalkomey, 1997; Hirsche *et al.*, 1998). Furthermore, it is very difficult to support any attempt to predict reservoir properties not sampled by well logs or training data, a common situation in frontier areas without enough well control. Rigorously, the interpretation is limited to the training data.

Rock physics has been included in seismic interpretation as a post-process of the so-called seismic inversion, establishing the link between the extracted impedances (or other attribute) and reservoir properties. Including rock physics not only validates the transformation to reservoir properties, but also makes it possible to enhance well-log or training data based on geological processes (Avseth, 2000; Gutierrez, 2001; Florez, 2005). In particular, Mukerji *et al.* (2001) formally introduced statistical rock-physics methods as a way to combine rock physics, information theory, and geostatistics to reduce uncertainty in reservoir characterization. One of the key steps in that methodology is to extrapolate from the well data using a correlated Monte Carlo simulation. This procedure and the post-inversion analytical calculation of the attributes using the log data, depend on the validity of the point-to-point rock-physics relations. In statistical rock-physics techniques, wave propagation effects are included only in a very simplified way (e.g., in a single homogenous interface).

Different types of algorithms have been published for inverting the seismic data to elastic properties (mainly acoustic impedances or reflectivities). Russell (1988) presents in a condensed way the common traditional methods: Sparse-spike and model-based. Sparse-spike techniques are based on deconvolving the seismic trace under some sparseness assumptions of the reflectivity series, an idea initially proposed by Oldenburg *et al.* (1983). First, reflectivities are obtained; then, impedances are computed, including the missing low frequencies, usually from well data or seismic-velocity analysis. On the other hand, in model-based methods, starting from a given initial model, the inversion algorithm perturbs the model until some minimization criteria are satisfied. The objective function, or the function to be minimized, is usually some type of difference between the observed and modeled data. However, additional terms are usually included in the objective to restrict

possible solutions to those that satisfy additional criteria, such as a fixed mean layer thickness, or a condition of lateral continuity. Solutions obtained with model-based techniques strongly depend on the initial model, which is usually constructed using the well-log information. Sparse-spike methods and model-based techniques both provide a single solution no estimate of uncertainty.

The seismic inversion problem can also be formulated in a Bayesian framework. Following Tarantola's (2005) work, any inversion problem can be set up as follows:

$$\sigma_M(\mathbf{m}) = (\text{constant}) \rho_M(\mathbf{m}) \rho_D(\mathbf{g}(\mathbf{m})). \quad (5.1)$$

In equation 5.1, sub-indices M and D indicate the space in which the quantities are defined: M for model space, and D for data space; \mathbf{m} is the vector of parameters that defines the model, $\sigma_M(\mathbf{m})$ is the posterior probability density, $\rho_M(\mathbf{m})$ is the prior probability density, $\mathbf{g}(\mathbf{m})$ is the forward modeling operator, and $\rho_D(\mathbf{g}(\mathbf{m}))$ is the likelihood. The prior probability density $\rho_M(\mathbf{m})$ describes the state of knowledge about the solution before the data is incorporated to the problem, thereby defining the space of possible solutions. The likelihood $\rho_D(\mathbf{g}(\mathbf{m}))$ measures the similarity between the available data and the synthetic data obtained by solving the forward problem, i.e. applying the operator $\mathbf{g}(\mathbf{m})$ to a proposed model. Equation 5.1 is a general expression valid for any inverse problem. Under adequate assumptions, equation 5.1 leads to particular types of problems with well-established methods for finding the solutions. For example, as Tarantola (2005) shows that, assuming Gaussian distributions both for the prior probability density and for the errors in the data, and using a linear forward model operator, equation 5.1 yields a posterior probability density that is also Gaussian. In this situation, the mean and covariance of the posterior probability density are given by the solution of a least squares problem; that is, means and covariances are analytically defined. Without strong assumptions like the one just mentioned, equation 5.1 can be very difficult to solve, or even to pose in a closed analytical form. In such cases, the solution to the inverse problem consists of samples from the posterior probability density that can be obtained using Monte Carlo methods (Tarantola, 2005).

The prior probability density that defines the space of possible solutions does not

need to be analytically defined; it can be specified by a set of rules (Tarantola, 2005). Accordingly, the seismic inversion technique presented by Bortoli *et al.* (1993) and Haas and Dubrule (1994) proposes the use of geostatistical methods for defining and exploring the space of solutions. Specifically, Bortoli *et al.* and Haas and Dubrule incorporate the sequential Gaussian simulation algorithm (Deutsch and Journel, 1998) for solving the seismic-inversion problem. As with all geostatistical simulation techniques, this type of seismic inversion provides multiple, equally probable solutions. Generating many realizations can yield any desired statistics about the solutions and is thus the way to assess uncertainty. The objective of including geostatistical information in Monte-Carlo-based inversion algorithms is to give priority to solutions or configurations of the model parameters consistent with particular spatial correlations. Bosch (1999), Bosch *et al.* (2001), and Bosch *et al.* (2005) present algorithms and examples of inversions based on Monte Carlo methods, combining geostatistical information and data from multiple geophysical methods.

Traditionally, geostatistical methods relied on the two-point statistics (variogram) to capture the geologic continuity. However, the variogram does not incorporate enough information to model complex structures or curvilinear features. To overcome these limitations, Guardiano and Srivastava (1993) present the ideas of training images and multiple-point (*MP*) geostatistics. The training image can be defined as a representation of the expected type of geologic variability in the area of study. It reflects the prior geological knowledge, including the type of features or patterns expected, but it does not need to be conditioned to any hard data. The central idea of the *MP*-geostatistics paradigm is to capture multiple-point statistics or patterns from the training image using a predefined arrangement of pixels, or a template, and to use those patterns as the building blocks for the stochastic realizations. Single-normal equation simulation (SNESIM) (Strebelle, 2000) was the first practical *MP*-geostatistical algorithm published; it solved CPU and memory limitations of the Guardiano and Srivastava algorithm. In SNESIM, the conditional probability for assigning a value to a particular node is obtained from the training

image by counting occurrences of the same pattern.

An alternative multiple-point geostatistics algorithm, developed using ideas of image reconstruction, has been proposed (Arpat *et al.*, 2002; Arpat and Caers, 2004). SIMPAT (sequential simulation with patterns) (Arpat, 2005), as its name suggests, is a pattern-based geostatistical algorithm inspired by the problem of image reconstruction. In SIMPAT, the training image is used to obtain the possible geologic patterns in the study area. The patterns are used as the building blocks for the reservoir realizations. A pattern corresponds to the arrangement of pixels in a pre-defined basic shape or template. Arpat (2005) summarizes SIMPAT as follows: *“The technique builds images (reservoir models) by assembling puzzle pieces (training image patterns) that interlock with each other in a certain way while honoring the local data”*. Furthermore, Arpat (2005) proposes a way of including seismic data in SIMPAT simulations. In that approach, seismic data is used as an image. Seismic patterns are extracted from a seismic training image and are used jointly with the geologic (or facies) patterns. However, in some real situations, it is very difficult to make correlate a vertical section of the seismic data to a particular region of the subsurface. Wave propagation in the Earth is not a well-localized phenomenon; that is, there is not a simple correspondence between a single seismic sample and a particular depth position. A time-to-depth conversion is needed for correlating geologic and seismic patterns, a difficult task, given the always-present uncertainty in seismic velocities.

In this chapter, a novel inversion technique, which combines rock physics with MP-geostatistics simulation, is presented. The method as described, works for any inverse problem that can be approximated as a series of unidimensional forward-modeling operators. In addition, the technique can be easily extended to invert data from different geophysical methods simultaneously. This ability to account simultaneously for several types of geophysical data can considerably improve the prediction of reservoir properties. Sometimes, combining elastic and electric properties can be the key to identifying lithology and fluids. The solutions to the inversion problem provided by the technique are realizations of predefined groups in

the subsurface. A *group* is defined as a set of rocks with common lithology, fluids or any other reservoir property of interest. Each group has an associated distribution of physical properties to which the geophysical data respond. The method is presented for the acoustic case, i.e. normal-incidence seismic data. Hence, the physical properties associated to each group are P-wave velocity (V_p) and density (ρ). Although the method has been developed for two-dimensional (surface-versus-depth) acoustic problems, it can be extended to a more general, 3D, multi-physics case.

A modified version of the SIMPAT algorithm presented by Arpat (2005) was selected as the MP-geostatistical component of the presented inversion method. However, any MP-geostatistical technique, such as SNESIM (Strebelle, 2000) or FILTERSIM (Zhang, 2006), can be adapted without changing the core structure of the entire inversion algorithm. In the next two chapters, applications of the inversion technique proposed using synthetic and real wells and seismic data are presented.

5.3 Proposed algorithm for seismic inversion

The seismic inversion algorithm presented in this chapter is based on the formulation of an inverse problem as an inference problem (e.g. Tarantola, 2005). Rock physics and MP-geostatistical principles are used to constrain and explore the space of possible solutions. In addition to the innovative way of combining rock physics and MP-geostatistics, a fundamental difference between this method and any other seismic inversion technique is that the solutions given by the proposed method are equally probable realizations of spatial arrangements of *groups* in the subsurface. A *group* is defined as a discrete variable or index for naming rocks with similar characteristics, such as lithology and/or fluid. Every group has an associated distribution of values of the physical properties needed to perform the forward modeling, i.e. the physical quantities to which the geophysical method used responds.

As shown in Figure 5.1, the proposed inversion technique consists of two main steps: pre-processing and the inversion itself. In the pre-processing stage, the groups are defined and the pattern database is constructed. In the inversion step, which is

repeated several times using the result of the previous iteration as the starting point, multiple realizations of spatial distributions of groups are generated using MP-geostatistical techniques, in this case a modification of the SIMPAT algorithm (Arpat, 2005). Each realization is consistent with the geological model and the rock-physics transformations used, and attempts to minimize the difference between the seismic data and the synthetic seismic computed from the realization.

An important characteristic of the presented inversion technique is that it can easily account for different types of geophysical data simultaneously. Essentially, the main limitation for inverting different types of geophysical data simultaneously is that the inversion must use unidimensional forward operators or the full forward-modeling operator can be approximately factored into a series of unidimensional forward operators. Constraining the solutions with multiple physical properties can significantly reduce the uncertainty in predicting reservoir properties.

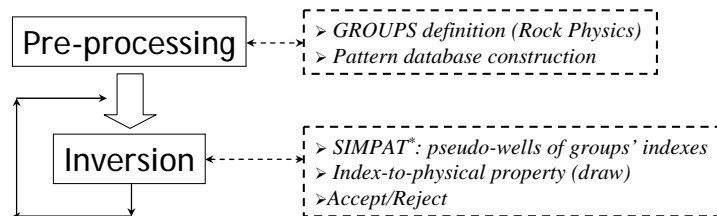


Figure 5.1: The two main steps of the seismic inversion method proposed –pre-processing and inversion itself– specifying the principal processes in each one.

Next, detailed descriptions of the pre-processing and inversion steps are presented. Two variations of the inversion step are proposed: a compact approach and an extended approach. Using the extended approach may give a better match between synthetic and data, but may forfeit some sharpness in the borders of the geological features. On the other hand, the compact approach favors well-defined and continuous borders, but requires that the training image contains large variety of patterns. To obtain reasonably good solutions with the compact approach, the training image has to be a more precise representation of the real geology, in terms of pattern contents, than when using the extended approach.

5.3.1 Pre-processing step

The pre-processing step is formed by two well-differentiated and independent procedures: definition of groups, and pattern database construction. The order of these two components of the pre-processing step is not important; both must be completed before starting the inversion step, since their results are required inputs for the inversion. Additionally, the group indices forming the training image must be defined in the same way as the building blocks of the inversion solutions.

5.3.1.a Group definition and rock physics

In the context of the proposed inversion method, the term *groups* defines the building blocks to construct the solutions, gathering rocks with similar reservoir characteristics as lithology, fluids, etc. Each group is represented by an index variable and has an associated distribution of physical properties needed to perform the forward modeling. In particular, for the acoustic case each group has an associated distribution of P-wave velocities (V_p) and densities (ρ). The groups are specifically defined for the reservoir to be analyzed, according to the goals of the study. The values of the groups' elastic properties are derived principally from well data. Given the importance of the elastic parameters associated with each group, rock physics should be used to validate and understand the well-log observations. Moreover, and more importantly for many real applications, rock physics can be used to extend the well data for predicting the elastic behavior of no-sampled groups expected to appear in the study area. As was mentioned before, the results of the inversion method are multiple realizations of spatial arrangements of groups. Hence, the definition of the groups is a fundamental step in the presented technique.

Figure 5.2 shows the groups that could be defined for the simplest case of lithologic identification in a clastic reservoir, inverting seismic data under the acoustic assumption. Only two groups with well-differentiated elastic properties are proposed: channel sand and background shale. The V_p - ρ distributions of each group could be defined from well-log observations; then, rock physics makes it possible to validate and edit the well-log data with quantitative criteria. Comparing the data

with an appropriate rock-physics model can be a way of identifying noise or bad data. In exploration areas, where the well-log data is usually scarce; the crucial advantage of using rock-physics is the ability to extend the training data, or equivalently, to predict the physical properties of groups not sampled by the wells but expected in the study area. Figure 5.3 illustrates that ability to generate elastic-property distributions for new groups not sampled by the wells. In this example, given the initial groups presented in Figure 5.2, rock-physics models are used to assign the elastic properties of the new groups.

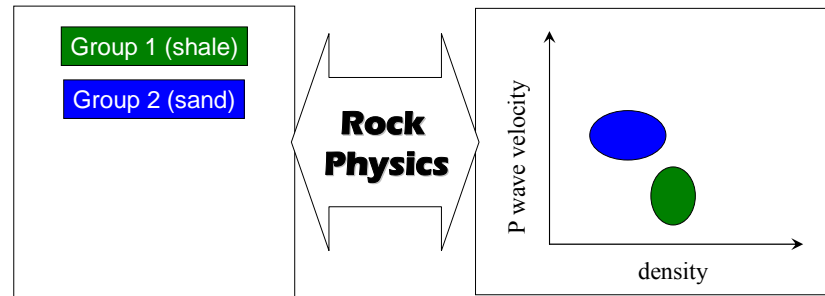


Figure 5.2: Typical groups defined for the simplest case of lithology identification in a clastic reservoir, inverting seismic (acoustic) data. For inverting acoustic data, each defined group has an associated distribution of P-wave velocity and density.

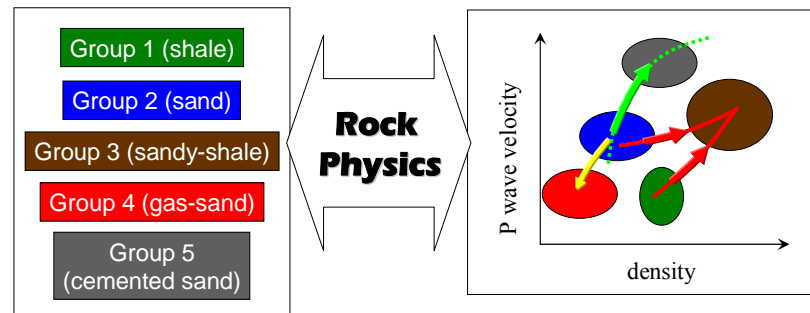


Figure 5.3: A rock-physics-based extension of the groups presented in Figure 5.2. The arrows indicate the rock-physics model used in each case: Gassmann fluid substitution (yellow arrow), Dvorkin's cementation model (green arrow), Marion-Yin-Nur "V" model (red arrows). Details of all the mentioned rock-physics models can be found in Mavko *et al.* (1998).

5.3.1.b *Pattern database construction*

The MP-geostatistics algorithm incorporated in the proposed inversion technique is a modification of SIMPAT (Arpat, 2005). SIMPAT builds realizations based on patterns obtained from the training image; hence, a pattern database is needed. The method for building the pattern database is essentially the same as that proposed by Arpat (2005). I describe the database generation for the two-dimensional case; consequently, the training image and the template are defined in a plane. For the 3D case, cubes or rectangular boxes replace squares or rectangles, but the general procedure remains the same.

The training image must be representative of the expected geology, built with the same groups defined in the other component of the pre-processing step. It has to be rich enough to contain all (or most) possible geologic patterns expected in the study area. As suggested by Strebelle (2000), a training image can be a realization of an object-based geostatistical technique. Once the training image is produced, it is scanned using a predefined template, or arrangement of cells. The scanning consists of moving the template over the entire training image. At each position, the cells covered by the template form a pattern. Each unique pattern is kept in the database. Although Arpat (2005) gives some indications about the selection of the template size, the optimal size is still an open question. The size of the template drastically affects SIMPAT's time of execution; therefore, it must be as small as possible, while still being at least as large as the main geologic features to be reproduced (e.g. wideness of a channel).

The process of building the pattern database using a simple training image and small template is illustrated. Figure 5.4 shows a 3-by-3 template and a training image of size 20-by-11 (x -by- z), formed by two types of group indices (channel and background). The training image proposed resembles a vertical section of the subsurface, cutting a set of channels perpendicularly to the original stream direction. Figure 5.5 illustrates three positions of the 3-by-3 template during the training image scanning. Note that each position of the template in the training image gives a candidate element for the pattern database. The pattern is retained for the database if

its configuration of group indices has not yet been encountered in the training image; therefore, each pattern in the database will be unique. The template is moved one cell at each step, until all training-image positions have been scanned, i.e. all possible center pattern positions have been visited. Figure 5.6 shows the patterns database constructed from the training image and template presented in Figure 5.4

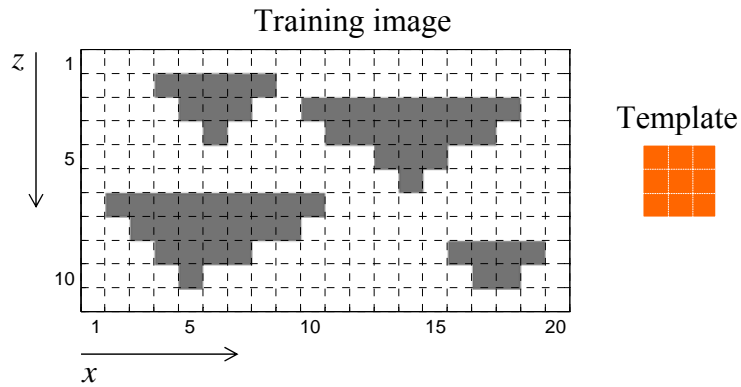


Figure 5.4: Two-dimensional training image resembling a vertical section of a set of channels (gray cells) encased in a homogeneous background (white cells), and a 3-by-3 reference template.

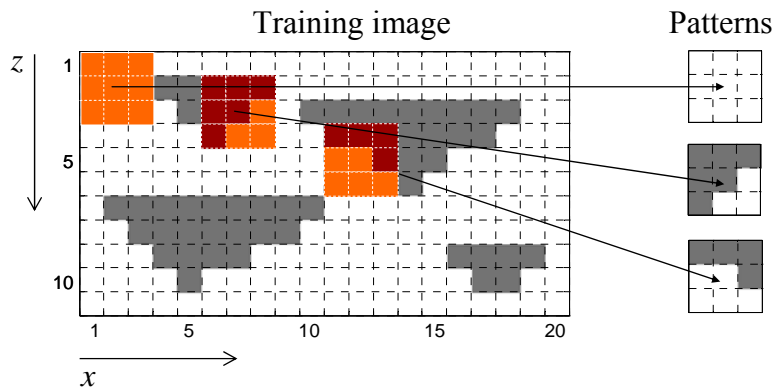


Figure 5.5: Three positions of a 3-by-3 template (orange cells) scanning the training image, and the corresponding extracted patterns.

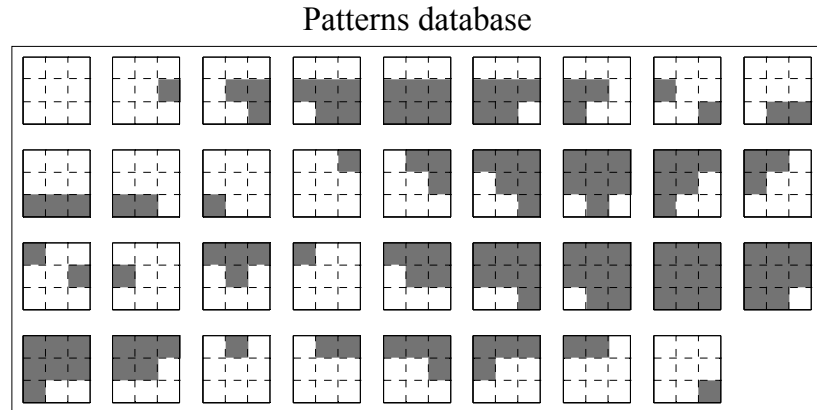


Figure 5.6: Pattern database for the first grid level generated using the template and training image of Figure 5.4.

To account for large-scale structures or correlations, without increasing the number of cells in the template, Tran (1994) introduced the multiple-grid idea. In the context of the presented inversion technique, using a multiple grid means that for each grid level “ $g+1$ ”, only the (2^g) th grid position on the training image is used to generate the pattern database. The values of “ g ” start with zero, where all (consecutive) grid cells are considered, as in the example of Figure 5.5. Figure 5.7 presents two positions of the template during the training image scanning for the second grid level of the multiple ($g = 1$), i.e. selecting every two grid cells. For each grid level considered, a pattern database is generated.

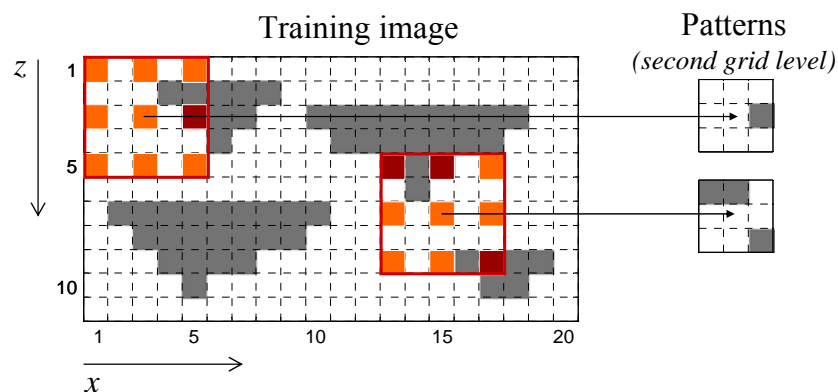


Figure 5.7: Two positions in the second level grid ($g=1$) of a 3-by-3 template (orange cells) scanning the training image and the corresponding extracted patterns.

To increase the interaction between the grid levels, not only the selected pattern is pasted in the solution grid, but also some of the continuous cells skipped when defining the grid level. This idea of pasting more cells than the template size is a small modification of the dual-template concept proposed by Arpat (2005). Although the patterns always have the size of the template, the associated pattern size changes with the grid level. To illustrate the associated-patterns concept, Figure 5.8 shows two positions of the 3-by-3 template when scanning the example training-image in the second grid level, the patterns from those locations, and their associated patterns. The associated pattern and the template always have the same length in the horizontal direction (x size). On the other hand, in the vertical direction, the associated pattern length for a grid level “g+1” is given by:

$$nzasp = 2^g (xtsiz - 1) + 1 \quad (5.2)$$

The use of the associated patterns guarantees that for any grid level, all depths or cells in the vertical direction will be filled. For seismic forward modeling, all z positions of the visited x must be assigned velocity and density values, a condition that, in the inversion technique presented, can be fulfilled only if all those cells have been assigned a group index.

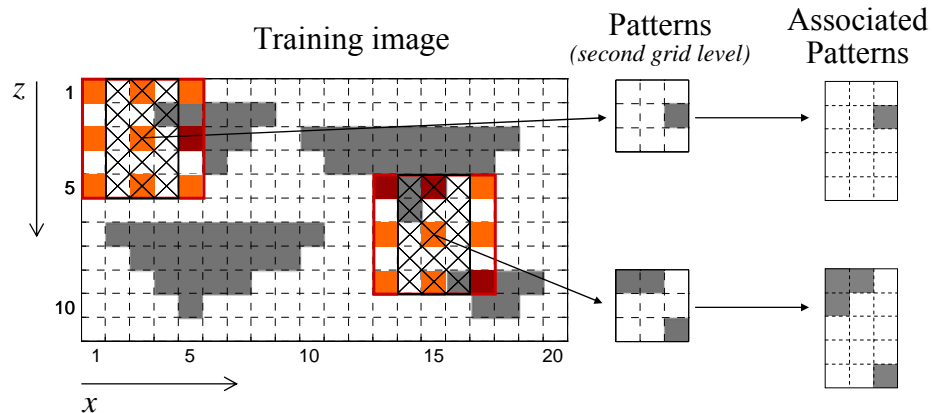


Figure 5.8: Two positions of a second grid level (3-by-3 template), showing the extracted patterns and the corresponding associated patterns.

5.3.2 Inversion step: Seismic (acoustic) inversion

The second step, the inversion itself, is an iterative process. In the current implementation, the number of iterations is a user-defined parameter that can be determined by running tests with a subset of the data. If desired, a criterion for stopping the inversion can be easily incorporated. The decision to finish the inversion can be based on a function of the global residual between the synthetic seismic and seismic data. For clearness, the presented description of the inversion step is restricted to the two-dimensional case, i.e. surface (x) and depth (z).

A synthetic example created from the cross-section presented in Figure 5.4 is used to illustrate all processes in the inversion step. Figure 5.9 shows the input data used in the example: the initial state of the solution grid with all cells empty except the ones corresponding to the well-log data, the distributions of elastic properties (V_p , ρ) for the two defined groups, and the seismic data. The pattern database used was constructed by scanning the training image of Figure 5.4. The input seismic data was generated using Kennett's algorithm, which gives the full normal-incidence elastic response of a layered medium. For a description of Kennett's algorithm, see for example Mavko *et al.*, 1998. A Ricker wavelet with a central frequency of 60 Hz was used for generating the data as well as for the forward modeling in the inversion.

As was mentioned before, two alternative approaches of the inversion step are proposed: the compact approach and the extended approach. In the following, detailed descriptions of both ways to complete the inversion step are presented.

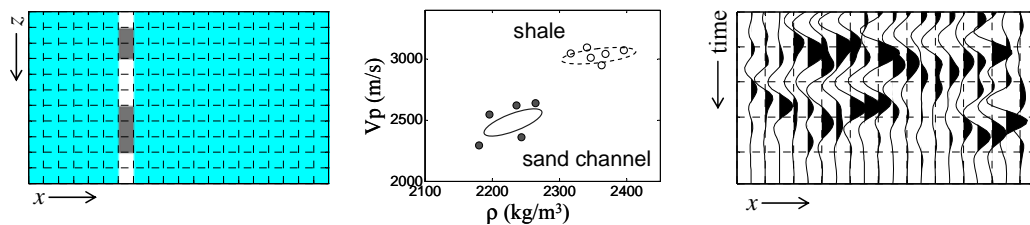


Figure 5.9: Input data used in the example for describing the inversion step: defined grid (cyan cells = empty) with the given well log of group indices, the elastic property distributions of the two defined groups (channel, background shale), and the seismic data.

5.3.2.a Inversion step: Compact approach

Figure 5.10 shows a schematic representation of the procedures that form a single iteration of the inversion step in the proposed compact approach. First, the order for visiting all desired x positions is defined by a pseudo-random path. The path is pseudo-random because the distance from the visited x -coordinate to the well position increases or does not change for each consecutive surface location selected. The randomness is introduced when selecting locations with similar distance from the wells.

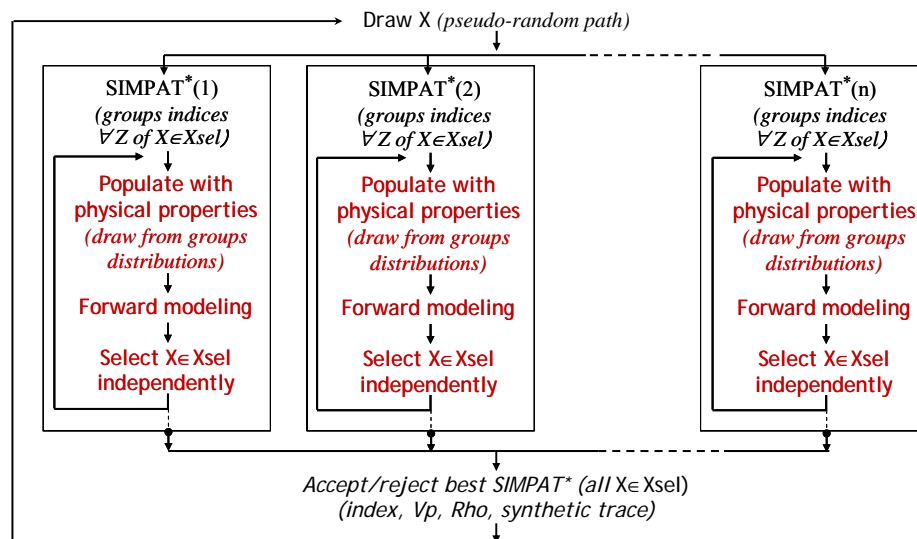


Figure 5.10: Schematic representation of the inversion step in the compact approach version. The components of the elastic loop are highlighted in red. An iteration is completed when all x positions defined in the pseudo-random path are visited.

At every surface position visited, multiple SIMPAT-modified simulations (SIMPAT*) are completed. Each SIMPAT* realization generates pseudo-logs of group indices at the visited x -coordinate and its surrounding locations, inside a radius of half the template's horizontal length. The principal differences between SIMPAT* and the original SIMPAT algorithm presented by Arpat (2005) are the way of defining the random path and the selection of cells that are written or filled when visiting any particular position of the grid. For every visited x and for every

grid level, SIMPAT* simultaneously creates pseudo-logs of group indices populating all z within a surface distance smaller or equal to half of the template's horizontal size.

To populate all z at the visited x location, SIMPAT* first defines a random path for all the z cells of the grid level in turn (starting with the coarser grid). At each z , the pattern from the database is selected that best matches the arrangement of group indices in the cells covered by the template. The non-empty cells covered by the template, which forms the pattern to be matched, are either hard data (usually from well logs) or previously simulated cells. When the compared cells are hard data, the patterns that match exclusively those cells are selected first. Then, the remaining cells covered by the template are considered for narrowing the choices that equally match the hard data. In the entire inversion process, the hard data is never changed.

As was initially proposed by Arpat (2005) for SIMPAT, the criterion selected for measuring degree of similarity between two patterns was the Manhattan distance. Let, $A=\{a_1, a_2, \dots, a_n\}$ and $B=\{b_1, b_2, \dots, b_n\}$, be the patterns to be compared, with a_i and b_i ($i=1, \dots, n$) being group indices. Then, the Manhattan distance between them is given by:

$$d = \sum_{\substack{i=\text{template} \\ \text{positions}}} \{a_i - b_i\}, \quad \text{with} \begin{cases} \{a_i - b_i\} = 1, & \text{if } a_i \neq b_i \\ \{a_i - b_i\} = 0, & \text{if } a_i = b_i \end{cases} \quad (5.3)$$

Once the best pattern is selected by minimizing d , the associated pattern is pasted, centered at the visited cell. As was described in the previous section (pre-processing step), the associated pattern fills or overwrites the grid cells in an area centered at the visited cell, with length x equal to the size of the template in the horizontal direction, and height z determined by the grid level defined in equation 5.2.

Figure 5.11 illustrates the main SIMPAT* steps used to populate the surrounding cells of a visited location: selecting cells to be compared, searching in the pattern database for the best match, and pasting the selected associated pattern. Particularly, Figure 5.11 shows the procedure corresponding to the first step, or the first visited cell, in the analyzed example (3-by-3 template, second level of grid). Figure 5.12

shows four SIMPAT* realizations of pseudo-logs of group indices for the first x visited (the well location) in the analyzed example. Because the template used has a length of three in the x -direction, three pseudo-logs of group indices are generated simultaneously by each SIMPAT* realization.

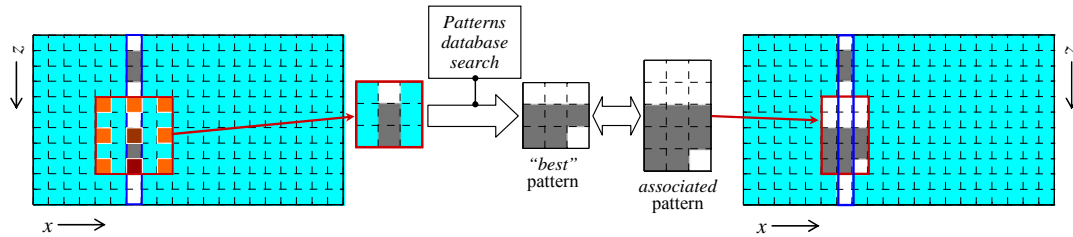


Figure 5.11: Main components of a single SIMPAT* step (step one in this case): selecting cells to be compared ($g = 1$, i.e. second grid level), searching in the pattern database for the best match, and pasting the selected associated pattern.

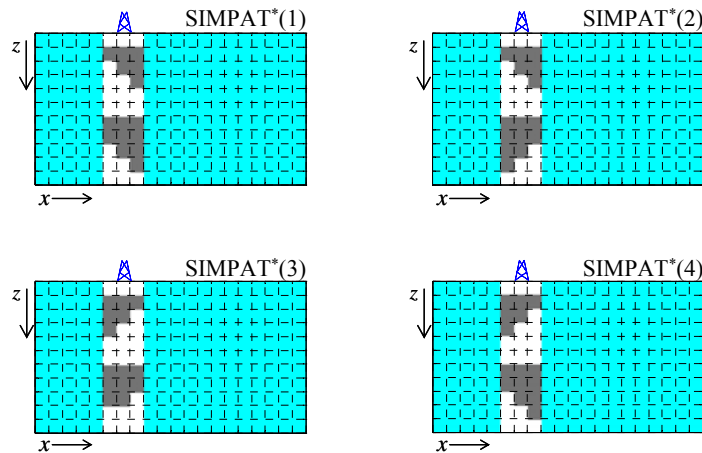


Figure 5.12: The result of four SIMPAT* realizations, completing the first visited x location (well position), i.e. simulating all z for all grid levels (two in this case).

The next step in the proposed compact approach is the elastic loop. A multiple, equally probable set pseudo-logs of elastic properties are created from each SIMPAT* realization, and a corresponding synthetic trace is computed. The goal of the elastic loop is to obtain the best pseudo-logs of elastic properties for the SIMPAT*-proposed group indices. The pseudo-logs of group indices are transformed into elastic properties, drawing for each sampled depth V_p and ρ values

from the corresponding groups' distributions. In the current implementation of the method, the distributions of elastic properties are assumed Gaussian. Therefore, for each defined group, mean and variance values of V_p and ρ , as well as the covariance between the two elastic variables, are the parameters required to describe completely the joint distributions of elastic properties. P-wave velocity pseudo-logs are used to make the depth-to-time transformation before computing synthetic traces. In this way, synthetic traces are generated in the time domain and can be directly compared with the seismic data. In the acoustic case, the pseudo-logs of acoustic impedance (AI) are obtained by simply multiplying the generated V_p and ρ pseudo-logs, transforming from depth to time sampling. Then, the reflectivity pseudo-logs, needed for the forward modeling are computed with the following relation:

$$R(t) = \frac{AI_{i+1} - AI_i}{AI_{i+1} + AI_i}. \quad (5.4)$$

Figure 5.13 shows multiple realizations of elastic properties (pseudo-logs) for the first SIMPAT* realizations of Figure 5.12, the synthetic seismic traces computed for each one, and the collocated seismic data traces (red lines). At the well location, the values of group indices and elastic properties are the observed in the well-logs. The synthetic seismic traces are computed by convolving every generated reflectivity pseudo-log with the given (input-data) wavelet. As Figure 5.13 illustrates the pseudo-logs of group indices and elastic properties corresponding to the traces that better reproduces the collocated seismic data are retained. The degree of similarity between a synthetic trace and a data trace, with 'ns' number of samples, is a function of the absolute values of the difference between samples (s_i), as the following expression specifies:

$$trzsims = \exp\left(-\sum_{i=1}^{n.samples} |s_i^{syn} - s_i^{dat}|\right). \quad (5.5)$$

The greater the value *trzsims* is, the more similar the compared traces are.

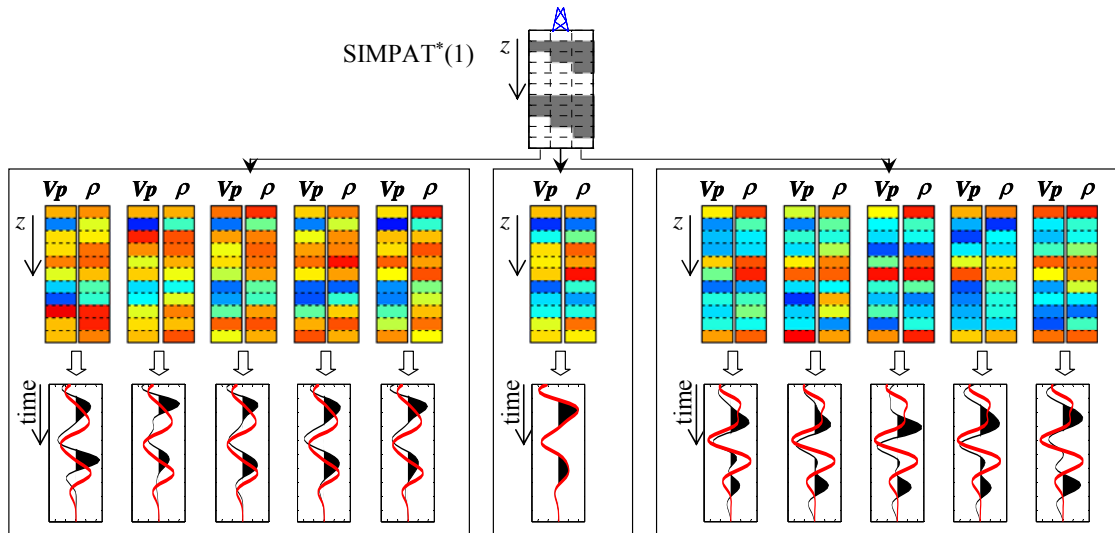


Figure 5.13: Multiple realizations of pseudo-logs of elastic properties for the first SIMPAT* realizations of Figure 5.12, the synthetic seismic traces computed for each one, and the collocated seismic data traces (red lines).

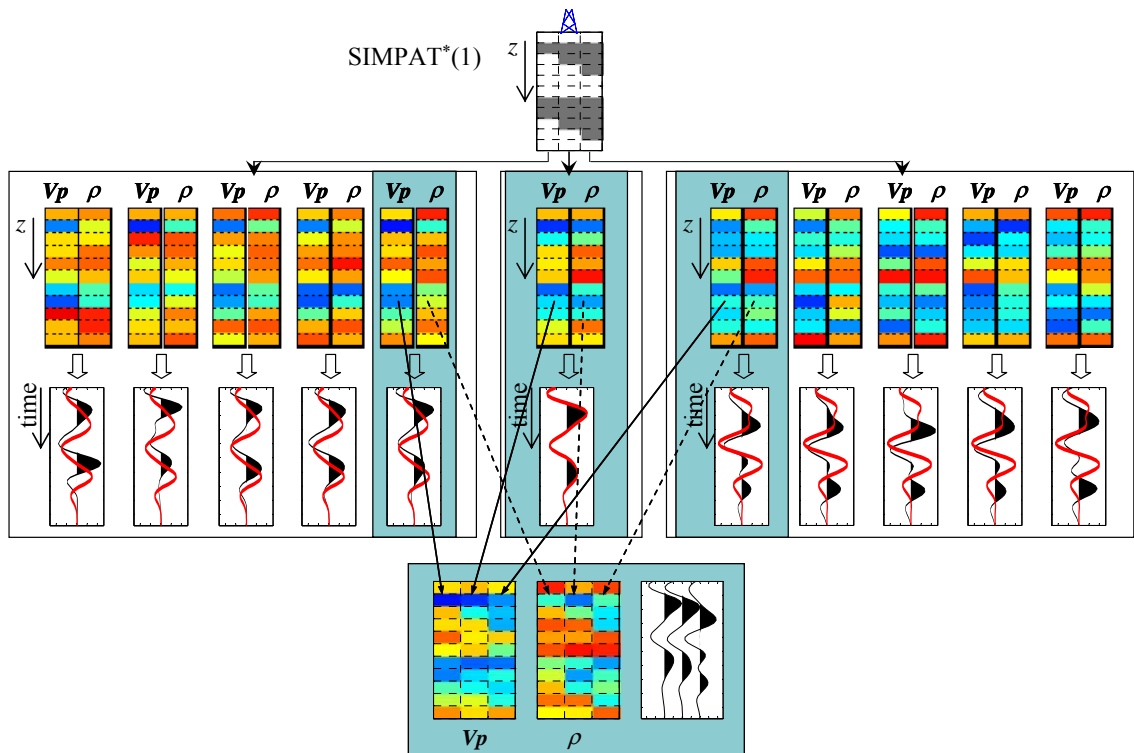


Figure 5.14: Selection of the elastic properties (V_p , ρ) pseudo-logs that generates the synthetic trace which better reproduces the collocated seismic data trace.

The decision of using an exponential function of the absolute value of the differences between samples to measure similarity was based on assuming that the errors in the seismic data can be described by a Laplace distribution function, i.e. $\exp(-|x|)$. As is well known, the results obtained minimizing in the l_1 -norm sense are robust (relatively insensitive to outliers). However, the option of using different types of misfit functions, like l_2 -norm or a measure of the correlation between traces, is an open topic for research.

The elastic loop is completed for all the SIMPAT* realizations providing the best set of elastic properties pseudo-logs sampled. Figure 5.15 shows the results of the elastic loop for the four SIMPAT* realizations of Figure 5.12, and the collocated seismic data traces (red lines). The SIMPAT* realization that produces the synthetic traces that match better the seismic data is selected. As Figure 5.15 demonstrates, in the analyzed example the best reproduction of the input data was obtained with the SIMPAT*(3) realization. The measure of similarity between a group of synthetic and data seismic traces is given by the following expression:

$$\text{enstrzsim} = \sum_{\text{trz}=1}^{\text{xtsiz}} \text{trzsim}_{\text{trz}} = \sum_{\text{trz}=1}^{\text{xtsiz}} \exp\left(-\sum_{j=1}^{\text{ns}} |s_j^{\text{syn}_{\text{trz}}} - s_j^{\text{dat}_{\text{trz}}}| \right). \quad (5.6)$$

Finally, if $\text{enstrzsim}_{\text{new}}$ (obtained by completing the described procedure) is greater than $\text{enstrzsim}_{\text{prev}}$ (calculated using previously accepted traces at the simulated x -locations), and greater than a user defined value (ensmav in equation 5.7), then the pseudo-logs of group indices and elastic properties corresponding to the traces compared are pasted into the corresponding solution grids, as Figure 5.16 illustrates. In case the proposed set of pseudo-logs is not accepted, the solution grids are transformed back to their previous states. The minimum value of enstrzsim for accepting the synthetic traces proposed is defined as a function of the seismic traces to which they are compared. The idea is to let the user define the precision required for reproducing the input seismic data. The user-input parameter α (usually smaller than one) defines the minimum acceptance value, ensmav , as follows:

$$\text{ensmav} = \sum_{\text{trz}=1}^{\text{xtsiz}} \exp\left(-\sum_{j=1}^{\text{ns}} \alpha |s_j^{\text{syn}_{\text{trz}}}| \right). \quad (5.7)$$

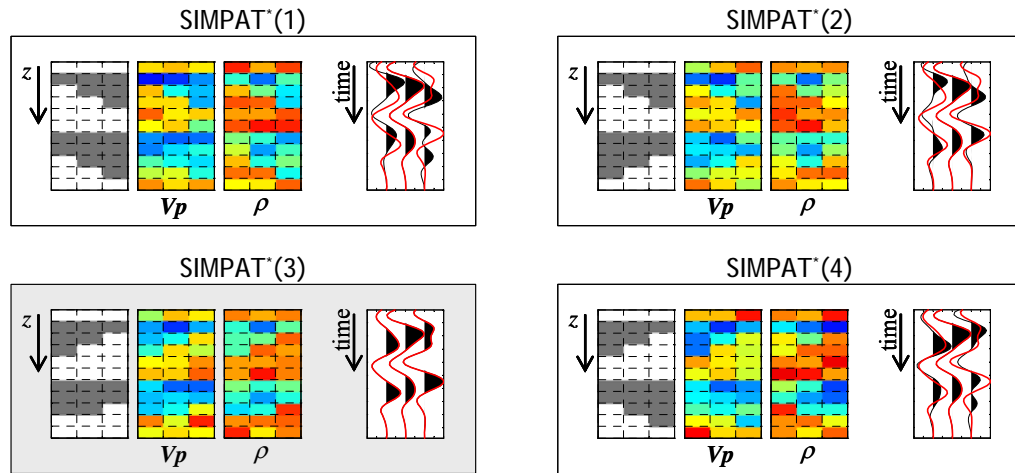


Figure 5.15: Results of the elastic loop for the four SIMPAT* realizations of Figure 5.12, and the collocated seismic data traces (red lines).

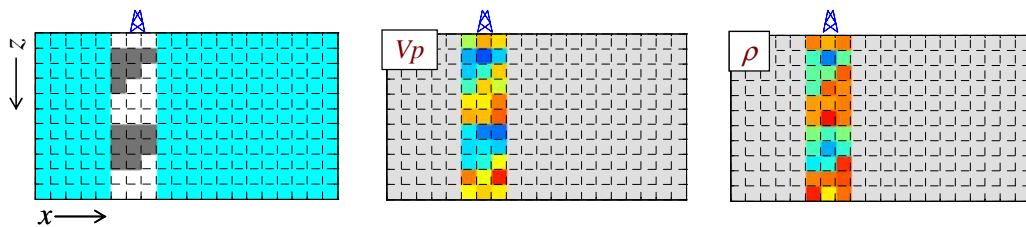


Figure 5.16: Result of the inversion step (compact approach) for the first x -position visited, i.e. the well location.

The process just described, i.e. SIMPAT* realizations and the associated elastic loop, is repeated for the next surface location following the pseudo-random path defined at the beginning of the iteration. The accepted pseudo-logs (group indices and elastic properties) affect or soft condition the subsequent simulations. An iteration ends when the pseudo-random path is completed, i.e. all x positions selected are visited. The obtained solution, input for the next iteration, is formed by the grids with accepted pseudo-logs of group indices, velocities and densities, and synthetic traces. Figure 5.17 shows the results of the inversion after completing the first and second iterations for the example used to illustrate the inversion step. Compared to the true model (Figure 5.4), the configuration and shape of the channels is very well recovered. It is important to remember that this is not the definitive solution, but is

one of many possible solutions, a single sample from the posterior probability density. Many samples must be analyzed to get a real idea of the complete solution.

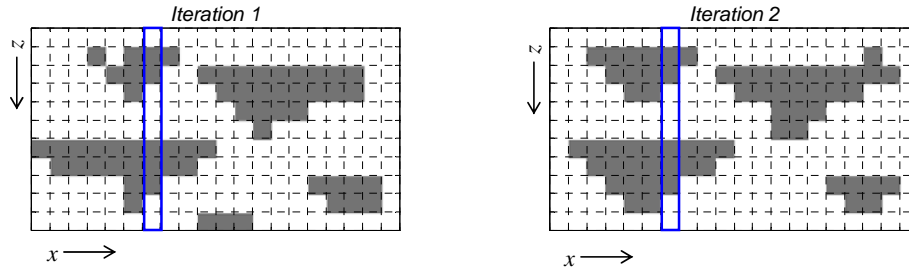


Figure 5.17: A result of two iterations of the presented inversion method on the synthetic example used for describing the technique. The blue rectangle indicated the well location.

5.3.2.b Inversion step: Extended approach

The components of the inversion step in its extended approach are shown in Figure 5.18. As can be noticed, the general structure is similar to that of the compact approach (Figure 5.10). However, in the extended approach every SIMPAT* simulation is repeated multiple times. Each SIMPAT* iteration starts with the pseudo-logs accepted in the elastic loop. Additionally, the final pseudo-logs of group indices and elastic properties that generate the best synthetic traces (better reproduce the collocated seismic data) at each x inside a radius of half of the template horizontal size are selected from all the SIMPAT* realizations independently. In this section, the steps in the extended approach that are different from the previously presented compact approach are described.

In the extended approach, at every surface position visited, multiple sets of two nested loops are performed, as illustrated in Figure 5.19. The external loop corresponds to multiple iterations of SIMPAT*. The SIMPAT* proposed pseudo-logs of group indices are accepted or rejected based on the results of the elastic loop, which is similar to that presented for the compact approach.

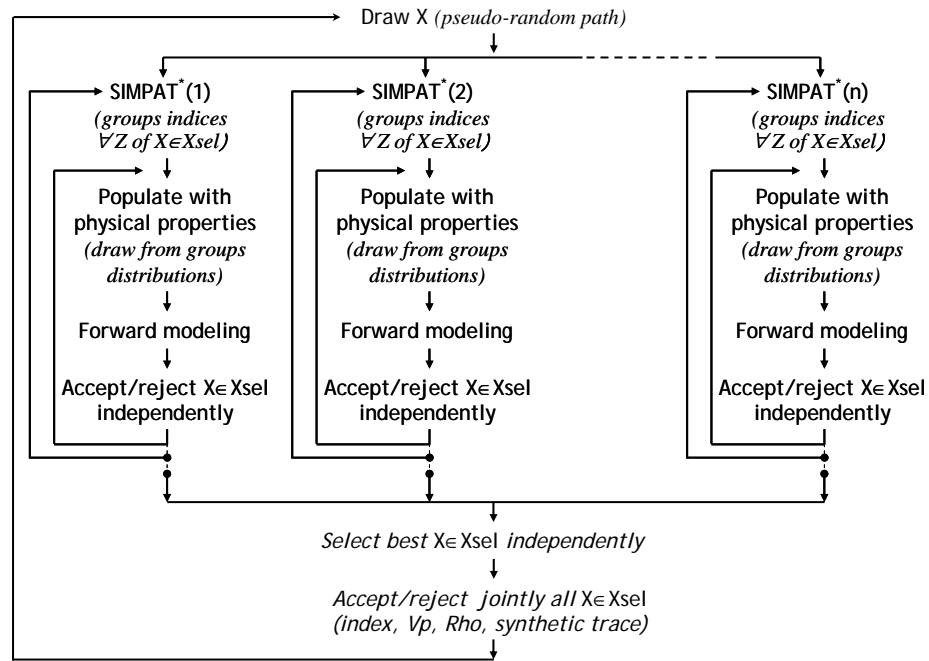


Figure 5.18: Flowchart of a single iteration of the inversion step (extended approach). Two loops are completed for every $SIMPAT^*$ realization.

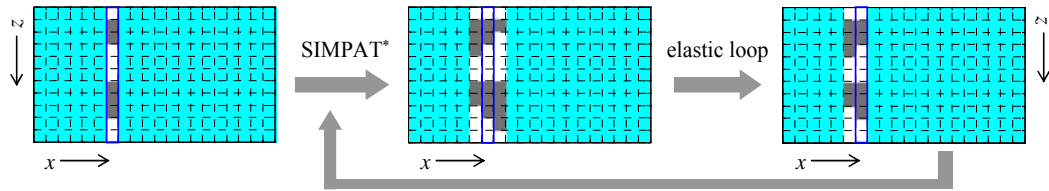


Figure 5.19: The two main loops in the inversion step (extended approach). First, a $SIMPAT^*$ realization is generated. Then, the elastic loop is completed selecting the synthetic traces that best match the seismic data, within a tolerance range. The selected traces and the corresponding elastic and group indices pseudo-logs are retained and used as the initial state for a following $SIMPAT^*$ simulation.

Figure 5.20 illustrates the elastic loop of the proposed extended approach. Four realizations of AI (computed by drawing values of V_p and ρ for each depth, conditioned to the $SIMPAT^*$ proposed group index) for the pseudo-logs of group indices created from a given $SIMPAT^*$ simulation are shown. For each x -position simulated, only the synthetic traces that match the seismic data better than a user-defined value (mav in equation 5.8) are retained. The pseudo-logs of group indices and elastic properties corresponding to the retained traces are also kept. In the

extended approach, the degree of similarity between a synthetic and data trace is the same as defined for the compact approach (equation 5.5).

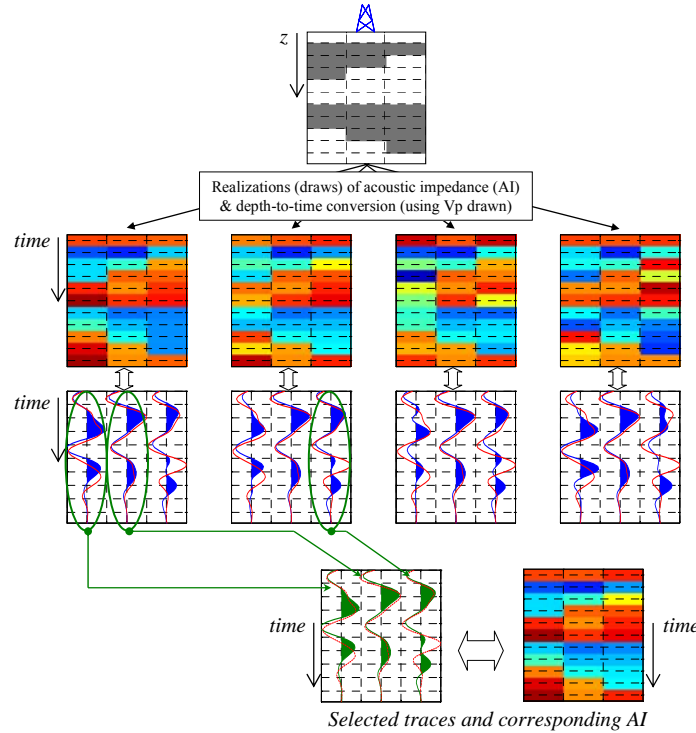


Figure 5.20: Illustration of the elastic loop, showing four realizations of pseudo-logs of acoustic impedance for a given SIMPAT* realization, the synthetic seismic traces computed from each one, and the selection of best traces.

In the elastic loop of the extended approach, each single trace is accepted if the value resulting from the comparison (tr_{zsim}) is greater than the mav value defined in equation 5.8. Similar to the compact approach, the comparison value is specified by the user defined parameter β , as the following equation shows:

$$mav = \exp\left(-\sum_{j=1}^{ns} \beta |s_j^{syn}|\right). \quad (5.8)$$

The retained pseudo-logs of group indices are used as input (soft) data for the next iteration of the external loop; that is, the next SIMPAT* simulation starts with the pseudo-logs of group indices accepted in the elastic loop, after the comparison with the seismic data. As shown in Figure 5.21, after independently completing

several SIMPAT*-elastic loop iterations, the synthetic traces that best match the seismic data at every location around the visited x are selected. Finally, the chosen traces form an ensemble that is compared with the collocated seismic data traces as a single entity, and it is accepted or rejected with the same criteria defined for the compact approach (equations 5.6 and 5.7).

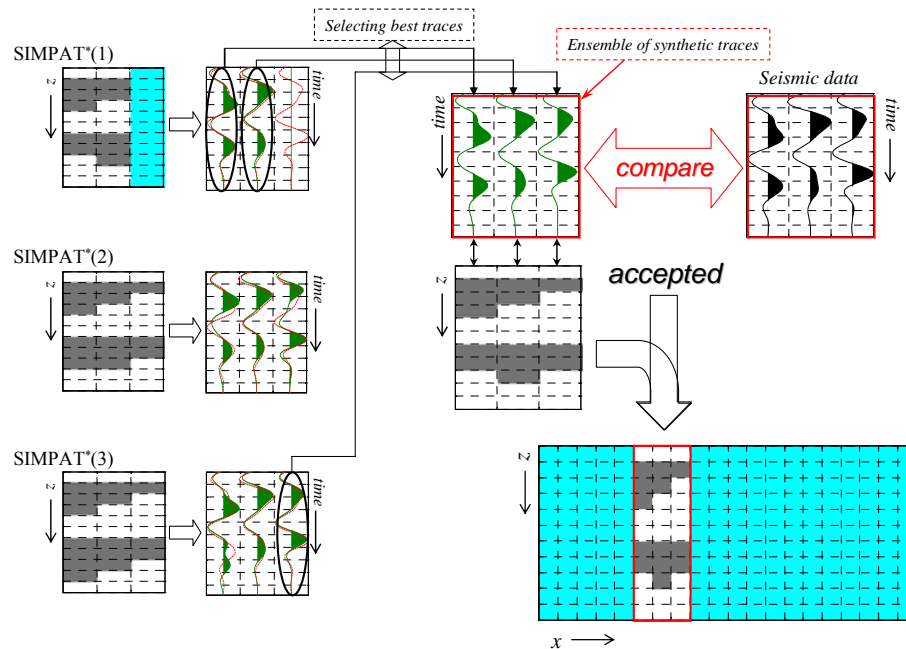


Figure 5.21: Last components of the inversion step (extended approach) for each visited x location. Best traces are selected from all the SIMPAT*-elastic loop realizations, forming an ensemble that is compared with the seismic data and previous accepted traces. If a better match, greater than a used-defined value is obtained, the corresponding ensemble of pseudo-logs is pasted into the solution.

In general, the compact approach favors continuity in the borders of the geological bodies proposed. However, because the compact approach cannot break or combine sets of pseudo-logs of group indices like the extended approach can, the condition on the training image to provide a complete set of patterns is stronger. The extended approach of the inversion step selects the best individual traces and pseudo-logs of group indices after each SIMPAT* realization, and when creating the ensemble of traces, gives more flexibility to find a match to the seismic observation.

More research needs to be done before discarding any of the presented approaches.

5.4 Future work

The obvious extension of the presented algorithm is inverting 3D data. The main modifications needed for a 3D version are the redefinition of the random path to visit all surface locations (x,y) , and the comparison of cubes (or rectangular boxes) instead of squares for template and pattern selection. For a 3D implementation, the code must be optimized as much as possible to compensate for increased CPU requirements, mainly caused by searching the pattern database.

The proposed inversion technique is not conceptually limited to the acoustic case. The conventional approach used to invert partial-offset-stack seismic for elastic impedance (Connolly, 1999) can be used with the presented algorithm. The single modification required is drawing three elastic properties instead of two during the elastic loop; hence, the values of “elastic reflectivities” can be computed and convolved with the given wavelet to generate the adequate synthetic traces.

A way for reducing the number and the length of the geostatistical simulations could be based on a windowed seismic comparison. Instead of revisiting all depths for each geostatistical simulation, this approach would refine the model in zones where the match between the synthetic and data traces is worst. The fact that the models are built in depth but the traces are compared in time limits the width of the windows and determines the order in which the process must be done. Alternatively, the splitting could be done in the frequency domain rather than the time domain. This approach would establish a correspondence between the multiple grid levels used for the geostatistical simulation and band frequencies of the seismic signal. Only low frequencies of the seismic data and a low frequency synthetic generated from higher levels of grids would be used, and only the best realizations would be kept for the next grid level. At every grid step (lower grid level), the frequency band of the synthetic and data traces could be increased to include more detail.

The criterion used to define the misfit or similarity between observed and modeled observations is another topic open for research. Inspired on the assumption

of a double exponential function for describing the uncertainties in the seismic observations, a l_1 -norm similarity function was used. However, criteria based on l_2 -norm or the correlation value could be explored.

In the current implementations of the algorithms, the elastic properties of each group are defined by bivariate Gaussian distributions, fixed for all the inversion. The option to include some type of variations to those distributions is an interesting topic to be explored. Gradual changes of depth, cementation, or even mineralogy that can be anticipated could be transformed in trends or smooth spatial variations of the distributions of the groups' elastic properties.

5.5 Conclusions

A novel inversion technique was presented, which combines rock physics with MP-geostatistical simulation. The method is based on the formulation of an inverse problem as an inference problem, with rock physics and MP-geostatistics as the elements for constraining and exploring the space of possible solutions. Although the technique is not restricted to any particular MP-geostatistical algorithm, a small variation of the stochastic simulation with patterns, or SIMPAT (Arpat, 2005), was the algorithm included. In the form that was presented, the inversion method works for any inverse problem that uses a one-dimensional forward modeling operator. It can be easily extended to invert *simultaneously* data from different geophysical methods, with the condition of a unidimensional forward modeling operator or full forward-modeling operator that can be approximately factored into a series of unidimensional forward operators. Electrical methods are strong candidates to be combined with seismic data in the simultaneous inversion proposed.

The solutions provided by the method are equally probable realizations of spatial arrangements of groups in the subsurface. A group was defined as a discrete variable or index for naming rocks with similar characteristics, such as lithology and/or fluid. Every group has an associated distribution of values of the physical properties needed to perform the forward modeling, the physical quantities that influence the geophysical methods used.

Chapter 6

Inversion method: Synthetic tests

“When a distinguished but elderly scientist states that something is possible, he is almost certainly right. When he states that something is impossible, he is very probably wrong” (Sir Arthur C. Clark)

6.1 Abstract

This chapter presents the results of a set of tests applied to the inversion technique introduced in the previous chapter. In each case, synthetic, normal-incidence seismic (acoustic) data was inverted to predict the spatial arrangement of groups in a reservoir, using the two proposed approaches of the method. For all tests, the model itself was clearly depicted by the zones with high values in the computed probability maps. The models used were 2D cross-sections extracted from a 3D synthetic reservoir model.

Five tests were performed. The first test aimed to validate the concept of the proposed inversion technique and the implementation of the proposed approaches. This test used the model itself as the training image to guarantee the completeness of the pattern database. For the second test, the training image was formed by combining twelve cross-sections with similar characteristics to the one used as the

model. In the third test, the elastic properties of the sand group were modified to create a partial overlap with the shale, simulating the case of a deeper reservoir. The fourth test simulated gas saturation in two of the channels. Two different scenarios determined by the well locations were tested: drilling into the gas channels, and missing them. In the case that the gas-saturated channels were missed by the wells, rock-physics models (Gassmann equations) were used to predict the elastic properties of the expected, but not sampled, group of gas-saturated sand. The fifth test shows the possibility of starting with an initial guess, which does not require the solution grid to be filled. It shows that a possible starting point for the inversion with the presented method can be based on the solution of a more conventional inversion technique. Starting with some initial information in the solution grid can reduce the number of iterations needed to obtain solutions.

6.2 Introduction

The aim of using geophysical methods for reservoir characterization is to reduce uncertainty in predictions of rocks and fluids away from wells or control points. The transformation of geophysical data, in particular the seismic data, into reservoir properties is an inverse problem. However, in geophysical jargon, the definition of seismic inversion is commonly restricted to the process of obtaining elastic properties in the subsurface from seismic data. Then, as a post-process using rock physics (in the best scenario), each elastic property in time or depth is transformed into reservoir properties point-by-point.

In the previous chapter, a new inversion method was presented. The technique combines rock-physics and multiple-point geostatistics methods in a Bayesian framework. The concept of a group was introduced in the inversion method as the building block for constructing solutions. A group is defined as a discrete variable or index for naming rocks with similar characteristics, such as lithology and/or fluid. Every group has an associated distribution of values for the physical properties needed to perform the forward modeling, i.e. the physical quantities to which the geophysical method used responds. The solutions of the proposed inversion

technique are realizations of spatial arrangements of the defined groups. A solution or realization is obtained after completing multiple iterations. The number of iterations is a user-defined parameter that can be determined based on the behavior of the global residual, i.e. based on a quantity that measures the difference between all the input seismic data and the forward-modeled synthetic seismic. Some of the key characteristics of the new inversion technique are the following:

- The solutions are consistent with the well data and the geological description.
- The solutions attempt to reproduce the expected continuity of the geologic bodies.
- A physics-based guess can be used for predicting non-sampled properties.
- Multiple solutions are provided for estimating uncertainties.
- The method is practical: limited time and resources are needed.
- Different data types (multi-physics) can be used simultaneously.

In this chapter, a set of tests using synthetic 2D seismic data are presented to demonstrate the validity of the proposed inversion technique. The two-dimensional models used were extracted from a modified version of the top layer of the *Stanford VI synthetic reservoir*. The Stanford VI reservoir was created by the geostatistics group in the department of Petroleum Engineering at Stanford University (Castro, *et al.*, 2005). All the information about the model relevant to this work is summarized in Figure 6.1. As can be seen, the basic model used to construct the tests was a cross-section of a simplified, two-lithology channel system with 80 cells in the vertical direction (z), corresponding to a total vertical thickness of 80 meters (one meter per cell). In the horizontal direction (x or *CDP location*), the length of the model was 3750 meters, given by 150 cells with an individual width of 25 meters. Figure 6.1 also presents the spatial distribution of the P-wave velocities (V_p) and densities (ρ), as well as a cross-plot between the two elastic parameters color-coded by the groups (channel-sand, background-shale).

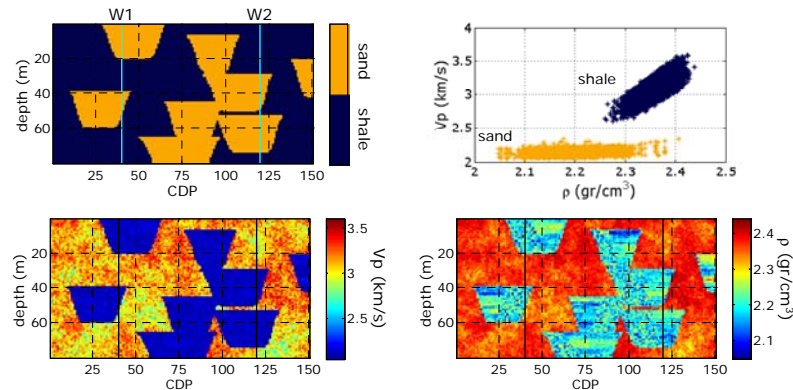


Figure 6.1: Geological framework of the model used for the first and second tests (top left). Cross-plot of all P-wave velocity (V_p) and density (ρ) values in the model, color-coded by the group (top right). Spatial distribution of V_p and ρ in the model (bottom). The wells (W1, W2) were located at CDP 40 and 120.

A synthetic seismic profile was computed using Kennett's algorithm implementation which models full, normal-incidence wave propagation, assuming a layered media at each CDP location (for a description of Kennett's algorithm, see for example Mavko *et al.*, 1998). A Ricker wavelet with 15 Hz central frequency was the wavelet used; hence, the approximate mean wavelengths for the channel sand and background shale were 210 meters and 140 meters, respectively. Figure 6.2 shows the computed seismic profile for the model given in Figure 6.1. Comparing the seismic with the input geologic cross-section shows that although some of the channels could be depicted in the seismic section, it is very difficult (maybe impossible) to predict lithology everywhere by examining only the seismic amplitudes.

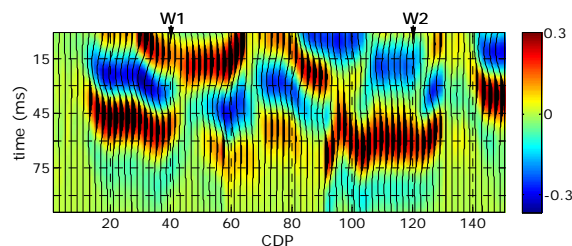


Figure 6.2: Synthetic seismic computed with Kennett's algorithm using a Ricker wavelet with 15 Hz of central frequency. All seismic traces were included for the color image, but only every fourth trace is plotted with a wiggle trace. W1 and W2 indicate the locations of the two given wells.

A characteristic of seismic inversion techniques like model-based and sparse-spike inversions is the tendency to generate layered solutions. This is an expected result, because the methods are based on that assumption. Though a layered assumption is valid in many situations, especially when stratigraphic sections of several hundreds of meters are studied, it is not always the appropriate hypothesis to describe the internal structure of a reservoir. Figure 6.3 shows the results of inverting the seismic data presented in Figure 6.2 using the model-based and sparse-spike algorithms of the commercial package STRATA (Hampson and Russell software, version 6.2). P-wave velocity and density information at CDPs 40 and 120 were given as input log data. As was pointed out before, the solutions obtained with these types of inversion algorithms are impedance profiles at each input trace position; consequently, a post-process is required to generate lithologic profiles. Some of the channels can be roughly depicted (low impedance values) in the areas around the first and last CDPs on both inversions; however, the channels between the wells cannot be identified. Although the solutions in Figure 6.3 are probably not the best that can be obtained with each algorithm, a drastic improvement cannot be expected, particularly in the central region of the model where most of the channels were present.

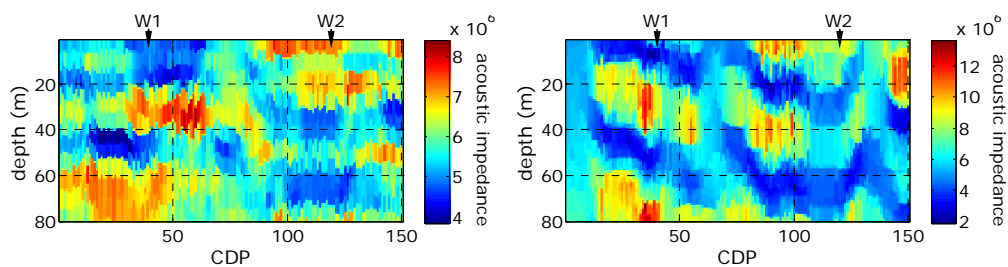


Figure 6.3: Acoustic impedance sections (depth) obtained by inverting the synthetic seismic of Figure 6.2 with model-based (left) and sparse-spike (right) algorithms. V_p and ρ information at CDP 40 (W1) and 120 (W2) were used as input data.

This chapter presents a set of 2D synthetic tests using both approaches (extended and compact) of the inversion technique presented in the previous chapter. All the models used for the tests were variations of the data shown in Figure 6.1. The

shapes and spatial arrangement of the channels, i.e. the geological framework, was similar for all the cases. The differences between models were created by modifying the elastic properties or adding a new group (gas-saturated sand).

For clarity and consistency in the presentation of the results, the same number of iterations (six) was selected for all tests to obtain a realization. This decision was based on multiple trials (with all tests). After six iterations, the sample-by-sample difference between the input seismic data and the synthetic data computed from the solution tend to remain constant.

The model shown in Figure 6.1 and the seismic data of Figure 6.2 were used for the first two tests. In the first test, the model itself was used as training image. The goal of using the model as the training image was to check the inversion concept itself and the validity of the implementations. For the second test, a training image was constructed from twelve cross-sections with the same size as the solution. Even though the dimensions of channels were well represented in the training image, none of the selected cross-sections had the same arrangement of channels as the true model. In the third test, the elastic properties of the sand group were modified to create some overlap with the shale V_p and ρ distributions.

In the fourth test, gas saturation was simulated in some of the channels. A strategy is presented to generate a training image that accounts for fluid variations without changing the initial geological concept. Results from inverting the corresponding seismic data for two different locations of the given wells, drilling and missing the gas sands, are discussed. The value of the inversion technique for extending the training data (samples from well-logs) using rock-physics is demonstrated with the fourth test.

The last test shows how the presented inversion method allows the user to input an initial guess of a possible solution. The initial model does not need to fill the solution grid. The inversion can be started with a rough picture of a possible spatial distribution of the groups, maybe only in the areas where the user is more confident about what groups to expect. The initial model is considered soft data for the inversion process. As shown in the analyzed tests, the solution from other inversion

method (e.g. model-based) can be used to generate the initial state of the solution grid.

For all tests, a probability map for each defined group is presented as the main result. These probability maps are equivalent to the geostatistical quantity known as *E-type* (average from realizations for each cell), given that group indices can be interpreted as indicator variables. In exploration situations, when well-log control is scarce, this type of result is probably the most important result expected. On the other hand, for later stages of development of the area, each of the solutions (inversions after a defined number of iterations) needs to be considered, as in any stochastic method.

6.3 Test 1: The model itself as the training image

The goal of the first test was to validate the proposed inversion method and to check the implementation of the algorithms. To accomplish that objective, the seismic data shown in Figure 6.2 was inverted using the model (Figure 6.1) as the training image. This guaranteed the completeness of the pattern database.

Figure 6.4 shows the logs of group indices and the ρ - V_p values from the two given wells (W1 and W2 at CDP 40 and 120, respectively). The mean, variance and covariance of V_p and ρ for each group (sand, shale) were computed from the logs. In this case, sand and shale elastic properties were well differentiated, with relatively low dispersion; hence, possible variations of arrangements of elastic properties inside the group zones gave similar seismic responses. In general, when the elastic properties of the groups are well-separated distributions with small dispersion, as a first order approximation, the elastic loop is not needed, or only a few draws are necessary. Even using only the mean values of the group's elastic properties can provide good results.

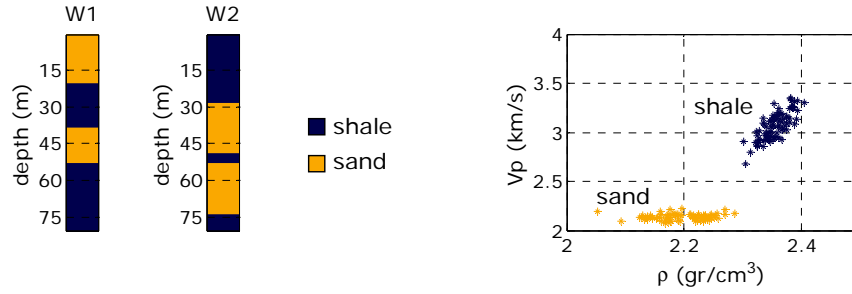


Figure 6.4: Well-log data used for the first test, extracted from CDP 40 (W1) and 120 (W2) of the model shown in Figure 6.1. Group-index logs (left) and a plot of P-wave velocity (V_p) and density (ρ) values, color-coded by the group (right).

The input parameters for the inversion's compact approach were the following: four grid levels, a 7-by-7 template, every other CDP visited, single draw used for the elastic loop, a comparison factor (defined in equation 5.6) with alpha of 0.8, and twenty SIMPAT* realizations for every visited CDP. The extended approach of the technique required an additional input value to define the number of times that SIMPAT* revisits the proposed pseudo-log of indices. To provide a fair comparison between the two proposed inversion approaches, five SIMPAT* realizations with four revisits at every visited CDP were used as input parameters for the extended approach. Table 6.1 summarizes the input parameters for the two inversion approaches used in the first test.

Table 6.1: Values of the input parameter used in the first test.

<i>Parameter description</i>	<i>Reference name</i>	<i>Value</i>
Grid levels ($g+1$)	grdlev	[4 3 2 1]
Template size	(ztsiz, xtsiz)	(7, 7)
Skipped CDP	jumpx	1
Elastic properties draws (loop)	elasloop	1
α (for comparison factor)	compval	0.8
SIMPAT* realizations per CDP	simxloc (compact approach)	20
	simxloc (extended approach)	5
Revisit SIMPAT* realizations per CDP (only for extended approach)	simxloc2	4

To illustrate how the inversion method populates the simulation grid, Figure 6.5 presents the initial state, four intermediates, and the final stage during a first iteration (for the compact approach). In the first iteration, the CDPs are visited in such an order that the distance to the wells increases (or remains the same) for each consecutive visited location. This is a way of propagating the information from the wells or control points. A different result than that in Figure 6.5, but also valid, can be obtained by simply changing the random seed to construct the pseudo-random path for visiting the CDPs.

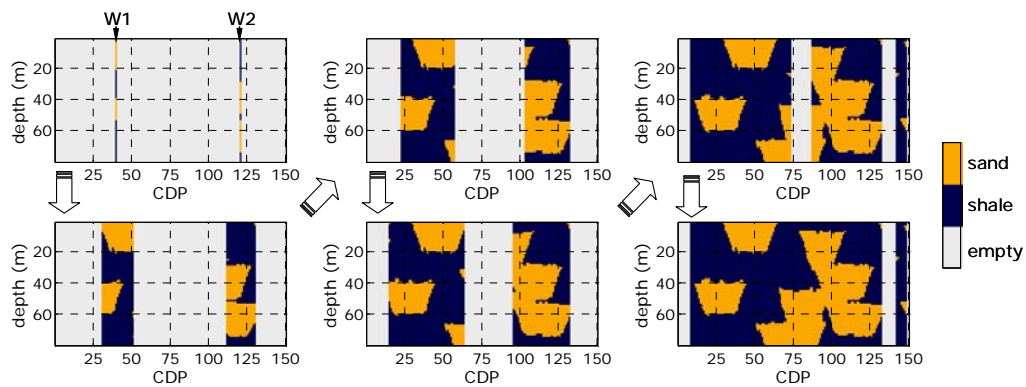


Figure 6.5: (First test) Initial state of the solution grid with only the information from the wells, four intermediates, and the result of a first iteration obtained using the compact approach of the proposed inversion algorithm.

Figure 6.6 presents the results of one set of six iterations. As was expected, with each iteration the reproduction of true model was improved. The first 10 CDP locations and the range between CDPs 133 and 137 were the regions that were more difficult to populate. A single group (shale) was present in those zones of the model, causing a seismic response with small amplitudes, requiring additional draws of elastic properties to reproduce better the internal arrangement of V_p and ρ . Additionally, in the current implementation of the inversion algorithms, the number of times the first and last CDP locations (within half of the template size in the x direction) may be filled is fewer than for rest of the CDPs. These locations are not included in the pseudo-random path.

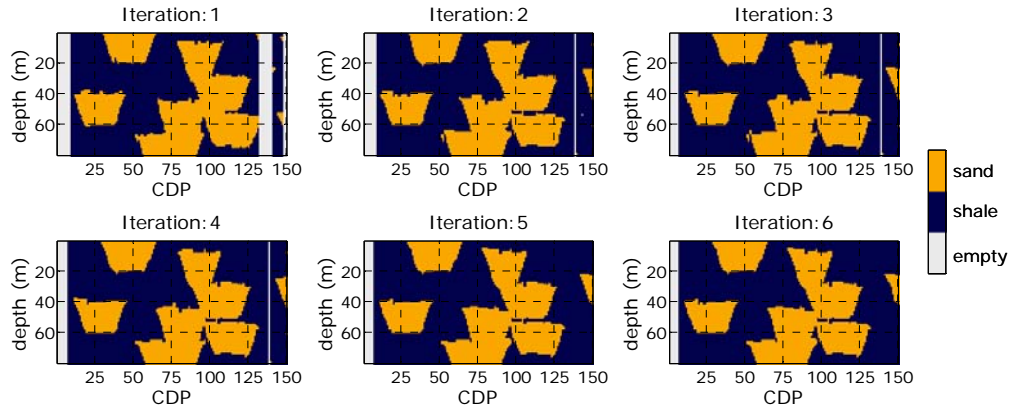


Figure 6.6: (First test) Results of one set of six iterations obtained using the compact approach of the proposed inversion technique.

Figure 6.7 shows the input seismic data used for the first test (same as Figure 6.2), the synthetic seismic result after six iterations of the compact approach of the inversion, and the sample-by-sample difference between them (residual). To allow comparisons, all seismic traces of Figure 6.7 were scaled to the same value. Simple visual inspection reveals the high similarity between the input and output seismic data. The low values of the residual verify that observation. Although Figure 6.7 shows only the synthetic output and residual of a single realization, it is a representative sample of all the obtained solutions for the first test.

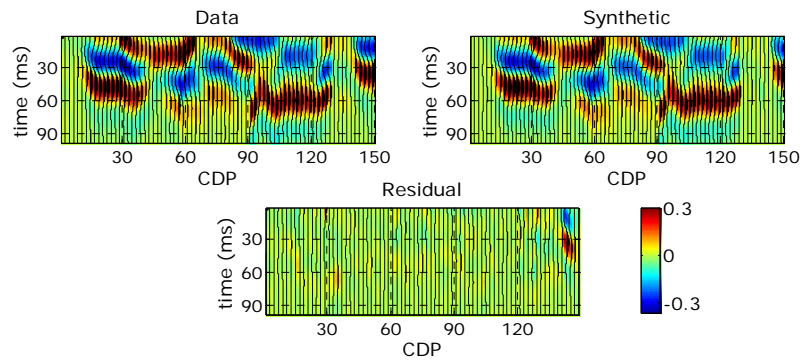


Figure 6.7: (First test) Input seismic data, synthetic seismic (output) after six iterations of the inversion compact approach, and the residual (difference sample-by-sample between input and synthetic). All traces are colored and scaled to the same value, but for clarity, the wiggles are plotted only at every other CDP.

Figure 6.8 shows the probability maps for the sand and shale groups, computed from thirty realizations of both proposed inversion approaches. This probability is a joint probability for all cells, so it cannot be used to draw group values individually at each cell or to generate solutions. Each realization of the complete reservoir is by itself a valid solution, equivalent to a draw from the posterior probability. Presenting the results as probability maps (in this case, equivalent to the geostatistical quantity known as *E-type*, given that the group indices can be seen as indicator variables) is particularly useful for the initial stages of development of a reservoir, where a primary goal is to depict the main geological bodies (groups). The results presented in Figure 6.8 demonstrate the validity of the proposed inversion technique and verify the implementations of both proposed approaches, since the model is clearly very well reproduced. As was expected, at the CDP locations where only shale was present, the probability maps values are zero for both groups. That indicates the cells at those locations were never filled. Additionally, although both E-types shown in Figure 6.8 are similar, some small differences can be identified. The border of the channels in the solutions from the compact approach tend to be better defined (more continuous) than in the solutions of the extended approach. This result illustrates the expected general differences between the two approaches of the inversion method presented.

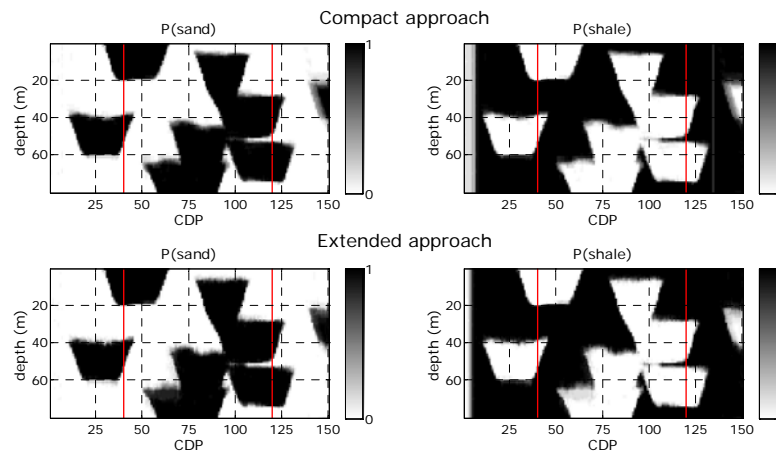


Figure 6.8: (First test) Probability map for sand (left) and shale (right) groups computed with 30 realizations of the proposed inversion's compact (top) and extended (bottom) approaches. Red vertical lines indicate the locations of the wells (CDP 40 and 120).

The probability maps shown in Figure 6.9 prove that in this case, all CDP locations (including the ones with only shale) can be correctly populated when 30 draws in the elastic loop are included. The input parameters for generating the 30 realizations to compute those probability maps were the same as previously mentioned (Table 6.1), except for *elasloop*, which was increased to 30. To illustrate the effect of adding multiple draws of elastic properties before the accept/reject decision in a particular realization, Figure 6.10 contains the input seismic data (for reference), the obtained synthetic data (from a realization) and their sample-by-sample difference or residual. Almost no difference can be detected between the two seismic sections, as the low amplitudes of the residual validate.

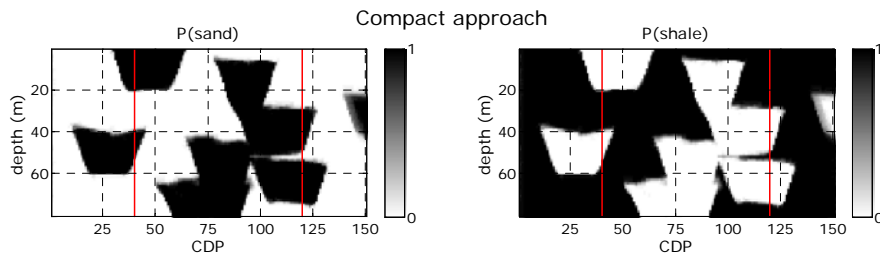


Figure 6.9: (First test) Probability map for sand (left) and shale (right) groups computed with 30 realizations of the proposed inversion's compact (top) and extended (bottom) approaches, with 30 draws in the elastic loop. Red vertical lines indicate the locations of the wells (CDP 40 and 120).

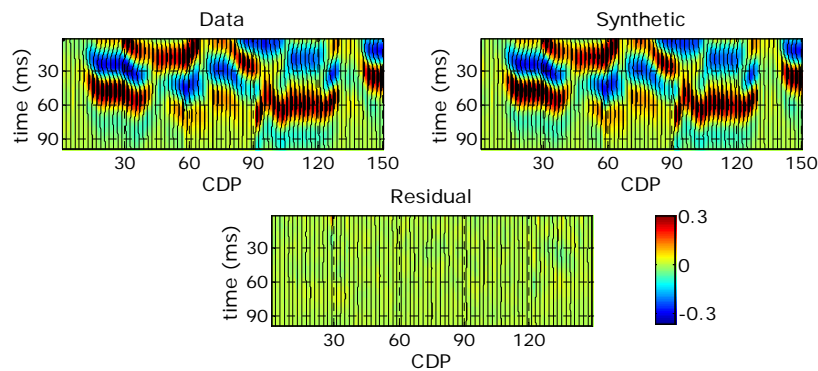


Figure 6.10: (First test) Seismic data (input) and synthetic data (an output) resulting from six iterations of the inversion's compact approach, and the residual (difference sample by sample between input and output data). All traces are scaled to the same value and colored, but for clarity, the wiggles are plotted only at every other CDP.

6.4 Test 2: composed training image

The model, well logs, and seismic data used for the second test were the same as previously described for the first test, but the training image was changed. For the second test, as a step toward representing a real case, the training image was constructed by extracting twelve cross-sections from the modified Stanford VI synthetic reservoir. The twelve cross-sections that formed the training image, shown in Figure 6.11, were parallel to the one used to create the input data. Although in the selected cross-sections the channels were individually a good representation of the channels in the true model, their spatial arrangements were different.

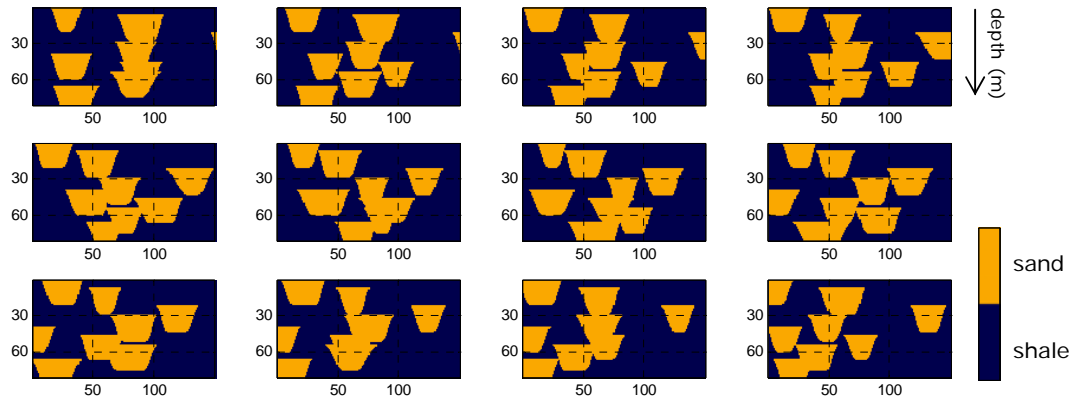


Figure 6.11: Training image used for the second test, formed by twelve cross-sections with the same size as the solution grid. None has the same spatial arrangement of channels as the model used to generate the input data.

For reference, to show the value of inverting the seismic data, thirty realizations of the reservoir were generated using the modified SIMPAT (SIMPAT^{*}), without including the seismic data. The input data were logs of group indices at the two given well positions and the training image of Figure 6.11. Each realization was the result of six SIMPAT^{*} iterations. Figure 6.13 shows the results of a set of six iterations completed to generate one solution or realization. As can be seen, the simulated channels start to show the expected shape after two iterations. Figure 6.14 shows three of the thirty SIMPAT^{*}-without-seismic realizations. By construction, all SIMPAT^{*} realizations are equiprobable results reflecting the geological concept

included through the training image, i.e. the shapes and general distribution of channels. On the other hand, the probability map shown in Figure 6.14 demonstrates that without any constraint between the wells, like that provided by seismic data, it was not possible to fix the locations of the channels.

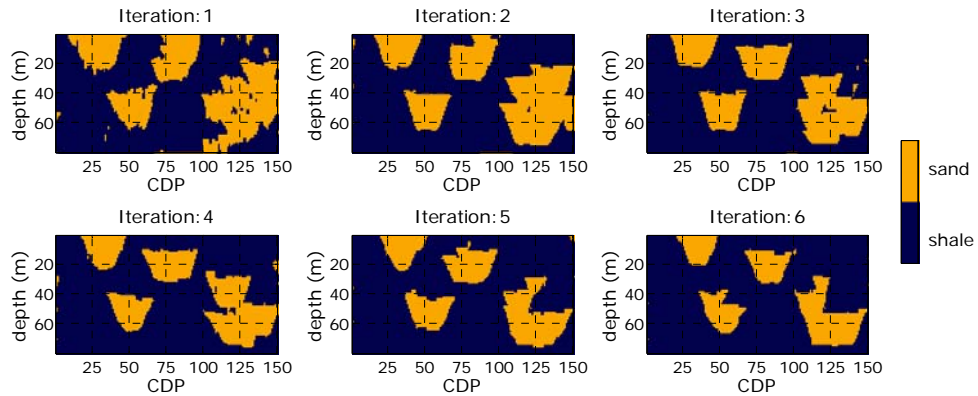


Figure 6.12: Results from a set of SIMPAT* iterations completed without seismic data to obtain one solution or realization.

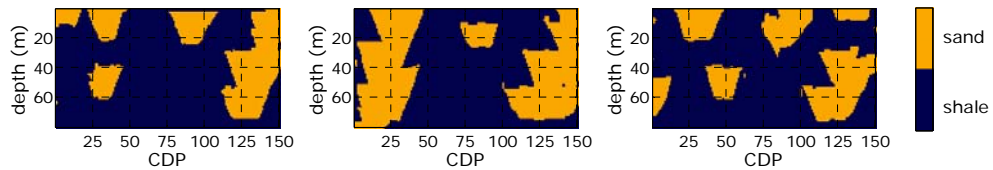


Figure 6.13: Three realizations (six iterations for each one) generated using SIMPAT* (without seismic) and the well-log data.

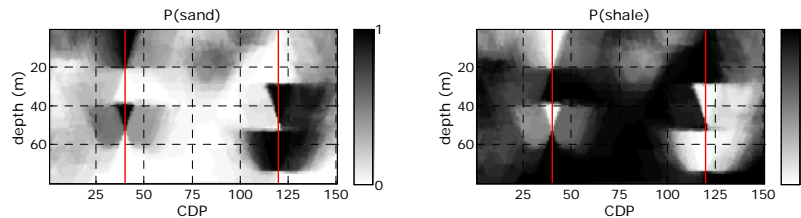


Figure 6.14: (Second test) Probability maps for sand (left) and shale (right) groups computed with thirty SIMPAT* realizations *without conditioning to the seismic data*. Red vertical lines indicate the locations of the wells (CDP 40 and 120).

Using the same input data and parameters as in the first example, but the training image of Figure 6.11, the seismic section shown in Figure 6.2 was inverted. Thirty realizations with each inversion approach were generated, then the probability maps shown in Figure 6.15 were computed. As a comparison between Figure 6.4 and Figure 6.15 reveals, the zones with high values correctly coincide with the channel locations in the model used to generate the input data.

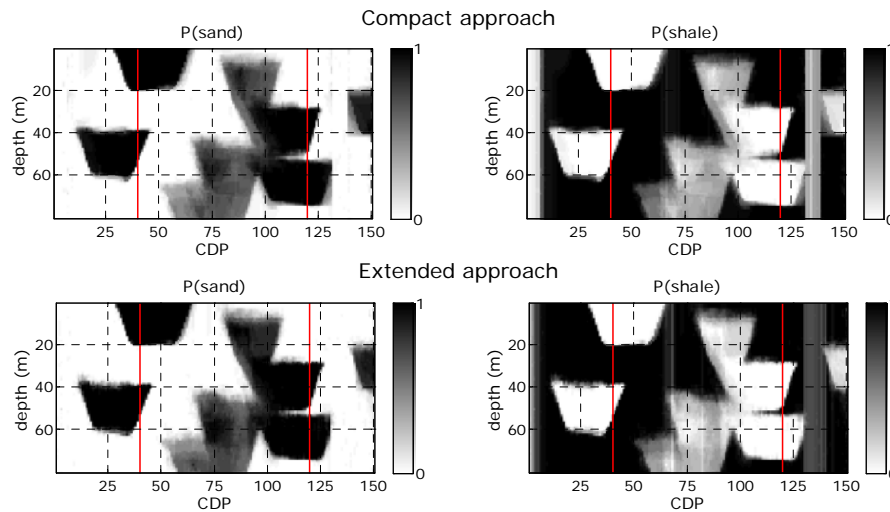


Figure 6.15: (Second test) Probability map for sand (left) and shale (right) groups computed with 30 realizations of the proposed inversion's compact (top) and extended (bottom) approaches. Red vertical lines indicate the locations of the wells (CDP 40 and 120).

6.5 Test 3: two groups with overlapping elastic properties

The geologic framework and the training image used for the third test were the same as for the second test. The elastic properties of the sand group were modified to create a partial overlap with V_p and ρ of the shale group. New seismic data was generated from the model with the modified elastic properties, using Kennett's algorithm with a Ricker wavelet of central frequency of 15 Hz. Figure 6.16 presents all the components of the model used in the third test: the new V_p and ρ spatial distributions, the cross-plot between those elastic properties, and the computed seismic section to be inverted.

The group-index logs of the two given wells (CDPs 40 and 120) and the cross-plot of their elastic properties, color-coded by group, are shown in Figure 6.17. Mean, variance and covariance were computed with the ρ and V_p well-log values to define the bivariate Gaussian distributions that describe the elastic properties of each group.

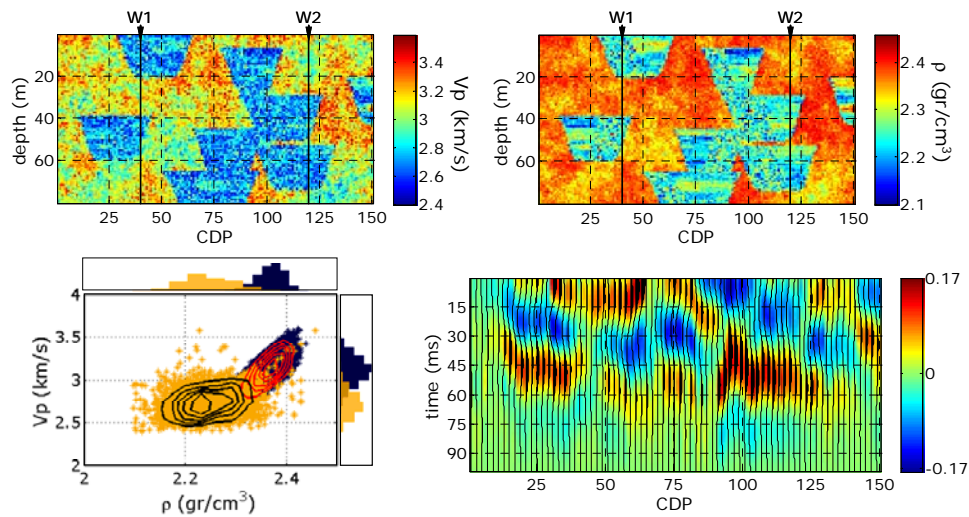


Figure 6.16: Model used for the third test: spatial distributions of V_p (top left) and ρ (top right), plot of all of V_p and ρ values, color-coded by group (lower left), and the computed seismic data (lower right). The third model was characterized by the overlap between the elastic properties of the two groups.

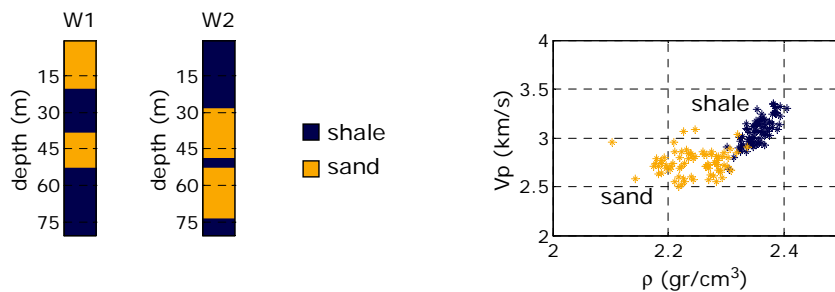


Figure 6.17: Well-log data used for the third test, extracted from CDP 40 (W1) and CDP 120 (W2) of the model shown in Figure 6.16: group-index logs (left) and plot of ρ - V_p log values color-coded by the group index (right).

The input parameters used for the inversions were the same as shown in Table 6.1, changing the value of *elasloop* to 30; that is, an elastic loop with 30 draws of elastic properties was completed for every pseudo-log of group indices simulated by SIMPAT*. The sand and shale probability maps obtained from thirty realizations (six iterations for each one) using the compact and the extended approaches are shown in Figure 6.18. Sand channels, which coincide with those in the true model, can be clearly identified in the probability maps. As can be seen, in the deepest region of the probability maps (below 70 meters) between CDP 125 and 140, the shape of a small channel, which was not present in the input model, can be discerned. A zone of relatively small elastic-property values, coincident with the referred area, can be seen in the input model (Figure 6.16), which, for this example, could well be attributed to the presence of sand channels.

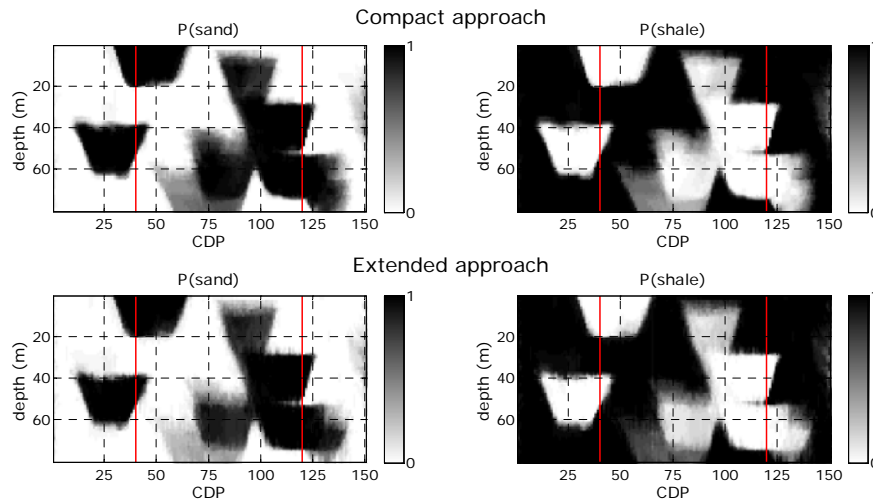


Figure 6.18: (Third test) Probability map for sand (left) and shale (right) groups computed with 30 realizations of the proposed inversion's compact (top) and extended (bottom) approaches. Red vertical lines indicate the locations of the wells (CDP 40 and 120).

6.6 Test 4: Gas sand

The fourth test was designed to develop a strategy for including fluid predictions in the solutions of the new inversion technique. A small variation in the geological framework was introduced into the model used for the previous tests. The channel

located at a depth of 60 meters and CDPs 100 to 125 was *disconnected* from the others, changing some of its cells to shale. That channel, and the one centered at CDP 25 between depths of 40 and 60 meters were simulated to be fully gas saturated. To account for the presence of gas, a new group was defined. The groups used for the fourth test were the following: brine sand, gas sand, and shale. Figure 6.19 shows the spatial distribution of the groups, V_p and ρ , as well as the V_p - ρ cross-plot (for all the points in the model) and the generated seismic data to be inverted. The amplitude values in the new seismic section corresponding to reflections from the gas channels were about twice the amplitudes from brine-saturated sands. The elastic properties for the gas-saturated sands were computed from the brine-saturated sand of all previous tests, using the approximation to Gassmann's equations presented by Mavko *et al.* (1995), with the input values shown in Table 6.2. Using the approximate Gassmann's equations, there was not need of shear waves information.

The solutions provided by the inversion scheme proposed are realizations of spatial arrangements of groups; hence, to include the prediction of different fluids, a group for each possible fluid-lithology combination needs to be defined. On the other hand, the geological concept or idea of the reservoir geology is usually fluid independent. Therefore, the training image needs to be perturbed to include variations of fluids inside the geological bodies with the appropriate lithology.

Table 6.2: Parameters used for the fluid substitution.

<i>Mineral</i>		<i>Initial fluid (brine)</i>		<i>Final fluid (gas)</i>	
<i>Parameter</i>	<i>Value</i>	<i>Parameter</i>	<i>Value</i>	<i>Parameter</i>	<i>Value</i>
P-wave modulus	96.6 [GPa]	Bulk modulus	2.57 [GPa]	Bulk modulus	0.133 [GPa]
		Density	0.99 [gr/cm ³]	Density	0.33 [gr/cm ³]

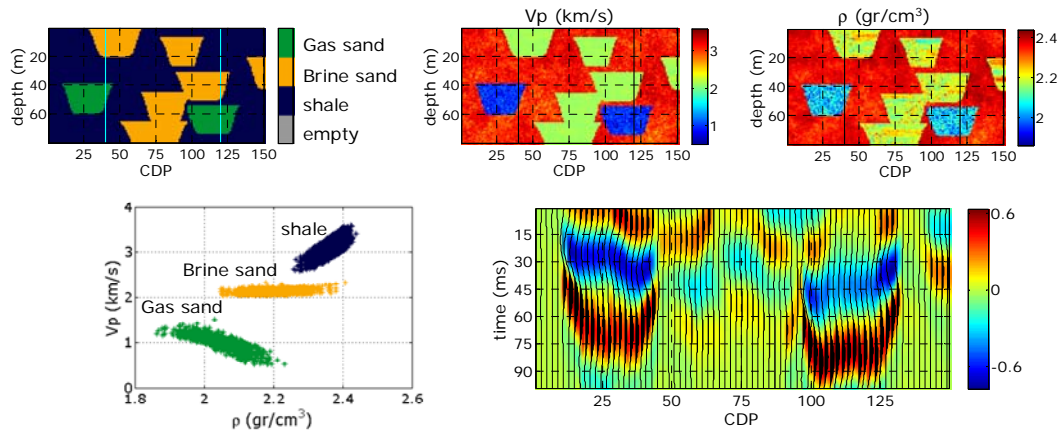


Figure 6.19: Model used for the fourth test: spatial distributions of group indices (top left), V_p (top center) and ρ (top right), plot of all of V_p and ρ values color-coded by the group (lower left), and the generated seismic data.

The training image used for the fourth test was generated based on the 12 cross-sections shown in Figure 6.11. For each cross-section, 12 new images were generated by randomly assigning to the channels one of the fluid-lithology groups. The connectivity between channels was checked before giving the saturating fluid in order to guarantee that any body was composed of a single group. Figure 6.20 shows the 12 variations of one of the cross-sections used as part of the training image in the fourth test.

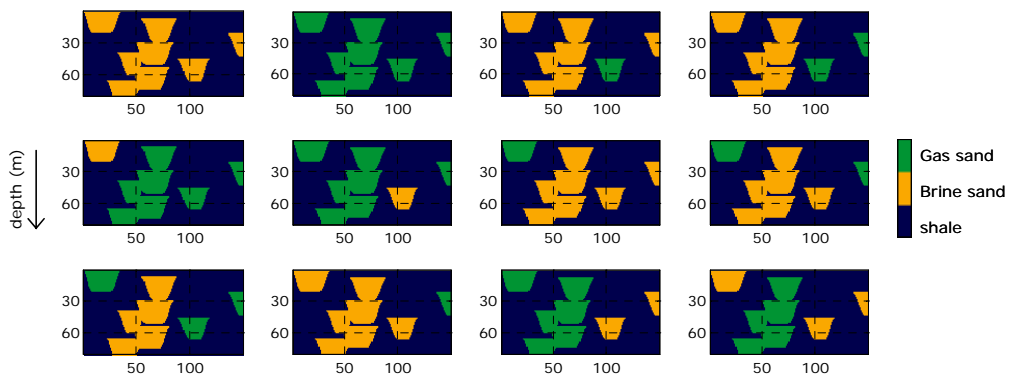


Figure 6.20: The twelve variations of one cross-section used as part of the training image in the fourth test. Although the geologic framework remains constant, each image shows a unique distribution of fluids in the geological bodies (connected channels) given by a distinct assignment of groups.

Figure 6.21 shows the group indices and the V_p and the ρ values from CDPs 40 and 120 of the model, given as well-log data for inverting the seismic profile in the fourth test. In this case, both channels saturated with gas were sampled by the wells. As was done in the previously described tests, the mean, variance and covariance to characterize the elastic properties of each group were computed using the well-logs. The parameters used with the two inversion approaches are presented in Table 6.3.

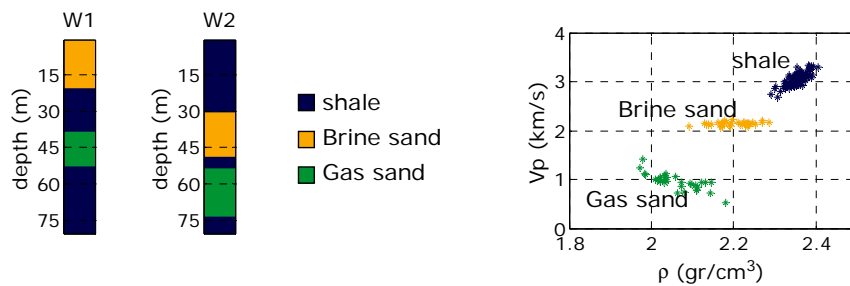


Figure 6.21: Well log data used for the fourth test, extracted from CDP 40 (W1) and 120 (W2) of the model shown in Figure 6.19: group-index logs (left) and a plot of V_p and ρ log values, color-coded by the group index (right).

Table 6.3: Values of the input parameter used in the fourth test.

<i>Parameter description</i>	<i>Reference name</i>	<i>Value</i>
Grid levels ($g+1$)	grdlev	[4 3 2 1]
Template size	(ztsiz, xtsiz)	(7, 7)
Skipped CDP	jumpx	1
Elastic properties draws (loop)	elasloop	1
α (for comparison factor)	compval	0.5
SIMPAT* realizations per CDP	simxloc (compact approach)	40
	simxloc (extended approach)	10
Revisit SIMPAT* realizations per CDP (only for extended approach)	simxloc2	4

As Figure 6.22 shows, the two gas-saturated channels were correctly defined by the areas with high values in the gas-sand probability map. Moreover, the zones with high values in all the group's probability maps were precise predictions of the

spatial arrangement of the corresponding group. Both approaches of the inversion methods gave the approximately the same results.

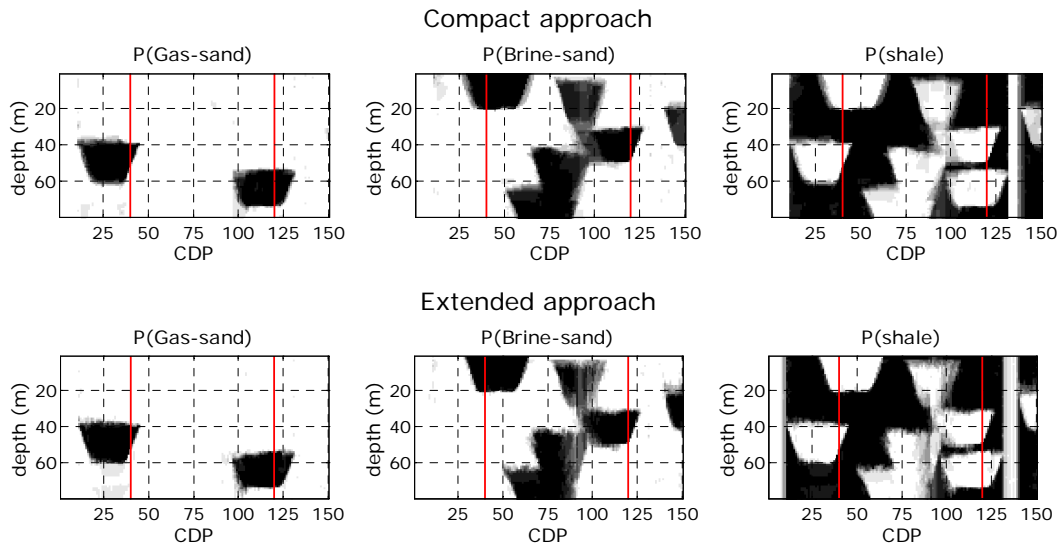


Figure 6.22: (Fourth test) Probability map for gas sand (left), brine sand (center), and shale (right) groups computed with 10 realizations of the proposed inversion's compact approach (top) and extended approach (bottom). Red vertical lines indicate the locations of the wells (CDP 40 and 120).

A variation of the fourth test, changing the well locations, was completed to show the value of including rock physics for the groups' definitions. The model, training image, seismic data and parameters for the inversion were the same as those used for the initial part of the fourth test. The new wells, WA and WB, were extracted from the input model (Figure 6.19) at CDPs 50 and 75, respectively. As is shown in Figure 6.23, wells WA and WB did not sample any of the gas-saturated channels. In this situation, where a group expected to be found in the reservoir was not sampled by the well data, rock physics can be used to extend the training data. From the information provided by the wells (WA and WB) and the knowledge that there can be gas in the reservoir, the gas-sand group was defined. Its elastic properties were computed with the V_p and ρ values from the wells, using the approximation to Gassmann's equations that do not require shear-wave data (Mavko *et al.*, 1995). In a real situation, if S-wave velocities are available, the original

Gassmann's equations must be used. Figure 6.23 presents the original and extended (with gas sand) distributions of elastic properties for each group.

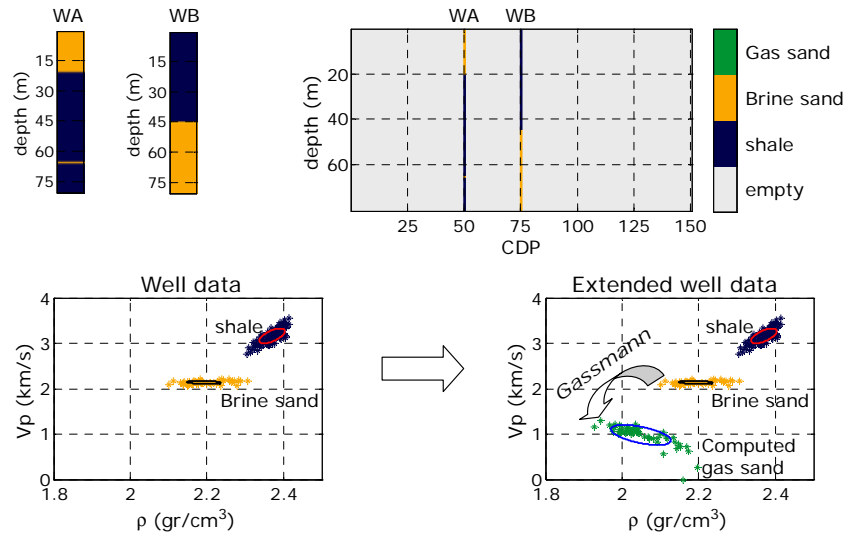


Figure 6.23: Well-log data used for the variation of the fourth test (moved wells), extracted from CDP 50 (WA) and 75 (WB) of the model shown in Figure 6.19: group-index logs (left) and plot of V_p and ρ log values, color-coded by the group index (right).

The probability maps for each group computed with 10 realizations of the compact and extended approaches are presented in Figure 6.24. Even without sampling any of the gas-saturated channels, their correct locations were clearly defined by areas with high values in the gas-sand-group probability map. Although the results obtained with both of the inversion approaches were similar, the gas-channel located around CDP 110 was slightly better defined in the probability map resulting from the extended-approach inversions. The brine-saturated channel centered on CDP 110, between 20 and 40 meters deep, was the object more difficult to identify in the probability maps. It was located on top of one of the channels saturated with gas, which at the seismic wavelength used was controlling the seismic amplitudes. In spite of being shadowed, the channel in discussion could be clearly discerned in the probability map computed with the extended approach.

As was mentioned before, the probability maps are excellent results for the initial

stages of reservoir development. They are a way to obtain an idea about the solution, but they are not the complete solution. It is always convenient to inspect some of the realizations individually, as well as the behavior of the value selected for measuring the misfit between the input data and the synthetic output. In the proposed inversion technique, the level of similarity between seismic traces ($trzsim$ in equation 5.5) was obtained with a function of the absolute value of the difference between samples. A variable named $enstrzsim$ was introduced (equation 5.7) in the extended approach to obtain a single estimate of the degree of matching in an ensemble of seismic traces. Increasing the number of traces compared to the total inverted was the natural way to extend $enstrzsim$ for defining a global estimate of the quality of fitting (in l_1 -norm sense). The new quantity, gL , is given by

$$gL = \sum_{trz=1}^{all\ traces} \exp\left(-\sum_{j=1}^{ns} |syn_{trz}(j) - dat_{trz}(j)|\right), \quad (6.1)$$

where, $syn_{trz}(j)$ and $dat_{trz}(j)$ are the values of the j^{th} sample of the synthetic output and input trace trz , respectively.

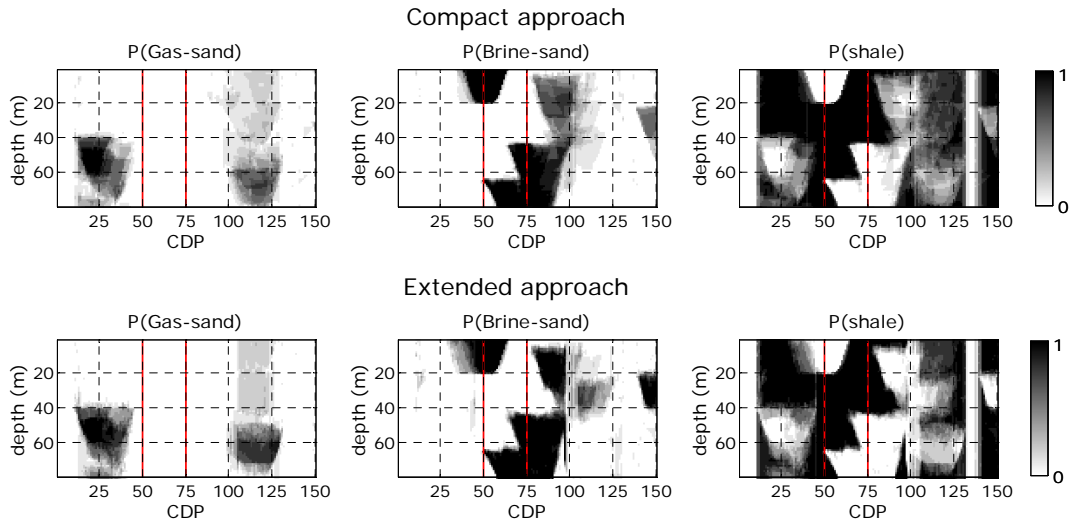


Figure 6.24: (Fourth test – variation of well locations) Probability map for gas-sand (left), brine-sand (center), and shale (right) groups computed with 10 realizations of the proposed inversion's compact approach (top) and extended approach (bottom). Red vertical lines indicate the well locations (CDP 50, 75).

Figure 6.25 shows four realizations (six iterations using the compact approach) of the spatial distribution of the groups, the corresponding residuals, and gL for each iteration. Figure 6.26 presents the same type of results obtained using the extended approach. In all the realizations shown, the brine-saturated channels located in the central range of CDPs, were very similar to the true model. Those channels were sampled by the wells. Comparing the results from both approaches shows that, although with the extended approach the borders of the channels were less continuous, the obtained residuals were smaller, or equivalently, the final values of gL were greater. This observation shows the ability of the extended approach to match the input data, creating some small irregularities in the geologic bodies.

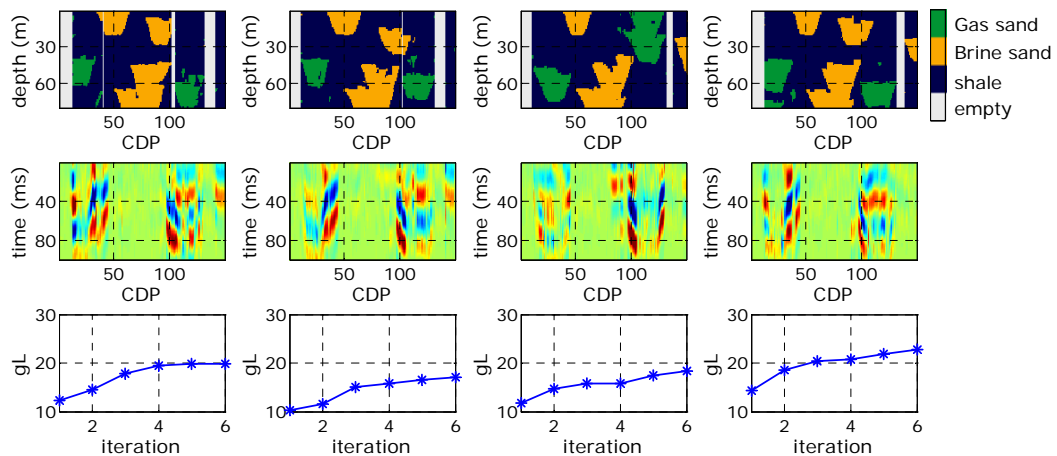


Figure 6.25: Results of the inversion (*compact approach*) of the seismic data generated from the fourth test model, with the given wells at CDP 50 and 75. Each column corresponds to a particular solution. Rows top to bottom: realizations of group indices, residuals (scaled to the input data), and gL for each iteration of the solution.

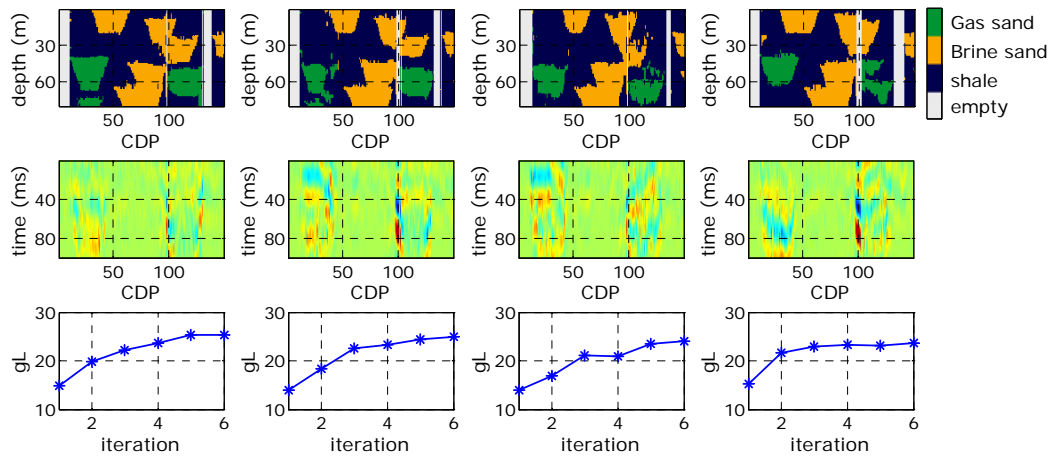


Figure 6.26: Results of the inversion (*extended approach*) of the seismic data generated from the fourth test model, with the given wells at CDP 50 and 75. Each column corresponds to a particular solution. Rows top to bottom: realizations of group indices, residuals (scaled to the input data), and gL for each iteration of the solution.

6.7 Test 5: Starting with an initial guess

The fifth test was designed to show the capability of the proposed inversion technique to start the search of solutions with an initial guess (initial model). In some situations, amplitudes or some other characteristics (attributes) of the seismic data clearly reveal a geological feature, such as a channel. That information can be incorporated into the inversion process through an initial model. Unlike other inversion methods, the initial model for the proposed technique neither is a requirement, nor needs to have all the cells filled. The aim is to start the inversion with an idea about the spatial arrangement of the groups, only in the areas of the reservoir where the user has high confidence. The main advantage of starting with an initial guess is to help the inversion to reach a stable value of gL , i.e. the point that the changes introduced for additional iterations are small.

As an option, the initial model can be generated based on a result from another inversion technique. To exemplify that idea, Figure 6.27 shows some of the states of the solution grid during the first iteration with the extended approach. The input well data, training image, seismic data, and parameters for the inversion were the same as those used in the second test. The initial model, shown with the wells added as the

first state in Figure 6.27, was built from the acoustic impedances obtained with the model-based inversion result (Figure 6.3). The values of acoustic impedance below the 15th percentile of the complete distribution of values were changed by the group index of sand. In this case, the well-log data revealed that low impedances were associated with the presence of sands. Only the lower 15th percentile was selected to show the intention of retaining only the zones with high confidence in the results. However, the smaller uncertainty regions are not always associated with extreme values. The initial model was considered soft data, i.e. the initial values can be changed during the inversion, as can be seen in the results of Figure 6.27. Again, the motivation of the fifth test was more to show the capability of starting with an initial model than make any comparison with results previously obtained.

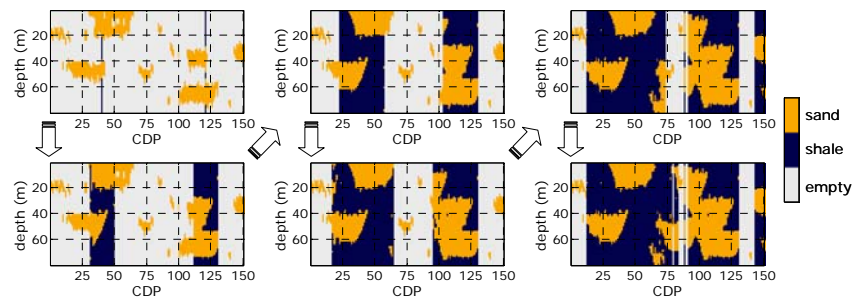


Figure 6.27: (Fifth test) Initial stage of the solution grid with only the information from the wells, four intermediates, and the result of a first iteration obtained using the proposed inversion's extended approach.

6.8 Conclusions

The results of the five tests presented validated both approaches of the inversion technique introduced in the previous chapter. For all tests, a probability map or *E-type* for each defined group was the main result shown. Those maps can provide critical information for reservoir development, especially during the initial stages.

The results of first test, in which the true model was used as training image to guarantee the completeness of the pattern database, validated the proposed inversion method as well as the implementation of the two approaches. The second and third tests showed that excellent predictions of the groups in the reservoir could be

obtained in situations that are more complicated, i.e. using a training image different from the true model, but representative of its geological framework, and with partial overlap in the elastic properties of the groups. Comparing these results to those of a type of pattern-based geostatistical simulation not constrained to seismic information demonstrated the value of including seismic data to reduce uncertainty when predicting the arrangement of groups in a reservoir.

In the fourth test, a strategy for including fluid predictions in the solutions of the new inversion technique was introduced. Additionally, a method was presented to generate a training image that accounts for fluid variations without altering the initial geological concept. Seismic data were generated for a model that included gas-saturated sands, and results were inverted with two different locations of the given wells, in one case drilling into the gas sands, and in the other, missing them. The brine-saturated channels could easily be differentiated from the gas-saturated channels in the probability maps obtained from the inversion; in particular, slightly better-defined channels were obtained in the extended approach. This demonstrated the value of the inversion technique for extending the well-log data using rock physics in the situation where none of the channels saturated with gas were sampled.

The fifth test showed the capability of the proposed inversion technique to start the search of solutions with an initial guess or initial model, derived for example from the interpretation of a seismic attribute or the result of another inversion method. The initial model for the proposed inversion technique is not a requirement, nor must all the cells be filled. The goal is to make it possible to start the inversion process with some prior idea about the spatial arrangement of the groups, but only in the areas of the reservoir where the user has high confidence, as an attempt to reduce the number of iterations needed to obtain a solution.

Although some observations about the results provided by the two inversion approaches were made, more tests need to be completed before we can define properly the situations that favor the application of each one. In general, the borders of the channels were better defined in the compact approach results. On the other hand, the extended approach results showed a trend of obtaining smaller residuals.

Chapter 7

Inversion method: Real data application

“I have been impressed with the urgency of doing. Knowing is not enough; we must apply. Being willing is not enough; we must do.”

(Leonardo da Vinci)

7.1 Abstract

This chapter shows the applicability to real situations of the inversion technique presented in Chapter 5. The data set used was provided by Chevron. The rocks in the studied reservoir were deposited in a clastic marine environment located on the continental slope, where turbidites are the main type of reservoir rock. Two wells, a near-offset 2D seismic section that intersects both well locations (extracted from a 3D volume), and the training image were the data used in this work. Three groups (sand, overbank, shale) were defined based on the geological information, training image and well-log data. In terms of hydrocarbon production, the studied area was in its first stages of development; hence, the well-log control was scarce. Defining the main facies distributions was a critical task at the time the work was completed. Based on that, the results of the seismic inversion are mainly presented as probability maps for each defined group. The solutions obtained using the two proposed

inversion approaches, including all the available information, are presented. Additionally, the results of the inversion using only one well at a time are shown. The way in which the implemented algorithms handle the common situation of data with different sampling intervals or grids is also described in this chapter.

7.2 Introduction

A new inversion method was presented in Chapter 5, and the results of testing it using synthetic data were shown in Chapter 6. This chapter presents the first application of both proposed inversion approaches to real data. The data set used for this work was provided by Chevron. The rocks in the stratigraphic sequence analyzed were deposited in a clastic marine environment located on the continental slope. Well-logs from two wells, a near-offset 2D seismic section intersecting the well locations, and the training image, all provided by Chevron, were the input data for the inversion. Figure 7.1 shows the gamma ray (GR), P-wave-velocity (Vp), and density (ρ) logs of the two wells. In this work, all depths were referred to the top of the studied reservoir.

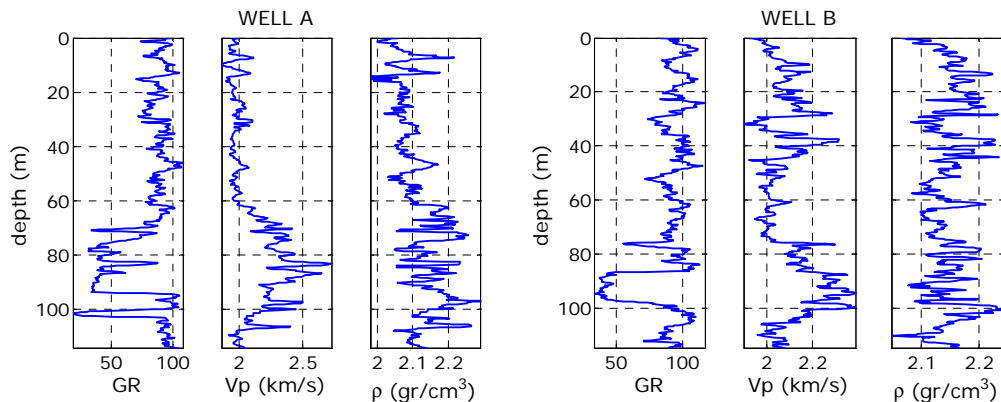


Figure 7.1: Gamma ray (GR), P-wave velocity (Vp), and density (ρ) logs from the two wells used in the study.

Figure 7.2 shows the 3D geological model from which the training image was constructed. As can be noticed, it was composed of three facies: sand, overbank, and shale. The geological model had 150 and 130 cells in the horizontal (x and y)

directions, and 20 cells in the vertical (z) direction. The horizontal dimensions (x - y) of each cell were 100-by-100 meters. Vertically, the twenty cells of the model covered the 112 meters of reservoir (5.6 meters for each cell). The 2D training image needed for the inversion was generated by extracting all the cross-sections parallel to the direction of the seismic data. Four of the cross-sections (x - z planes) that constitute the training image are shown in Figure 7.2.

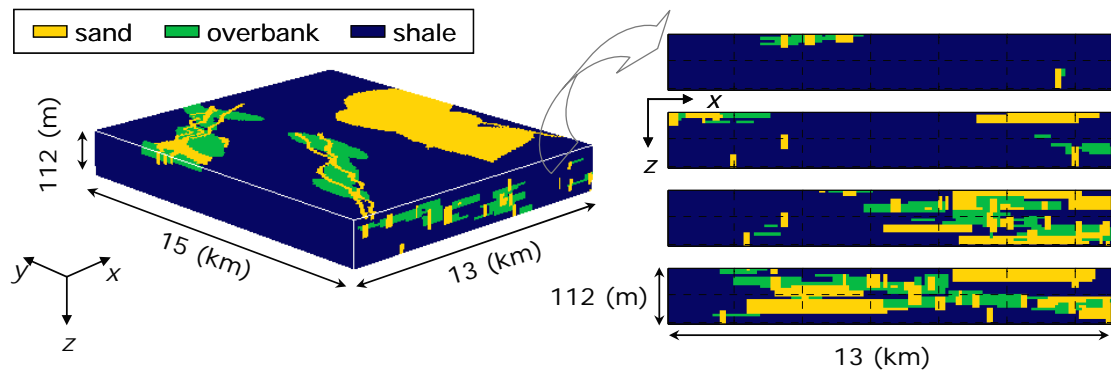


Figure 7.2: 3D geologic model used to build the training image, and four cross-sections, part of the training image, extracted parallel to the face of the model with a length of 13 km. The complete training image was formed from the cross-sections (x - z planes) at all y values.

7.3 Data preparation

The 2D seismic section for the inversion was extracted from the provided 3D near-offset seismic volume such that it intersected the locations of the two wells used. The approximate distance between traces in the original seismic volume was 25 meters. To match the resolution of the available training image, only one of every four traces were retained. Additionally, the main structural-geologic component was removed from the seismic data, flattening the reflection associated with the base of the studied reservoir. Figure 7.3 presents the 2D seismic section used as input for the inversion, indicating the locations of the two wells. The separation between traces (CDPs) was approximated as 100 meters, which coincides with the training image horizontal cell size.

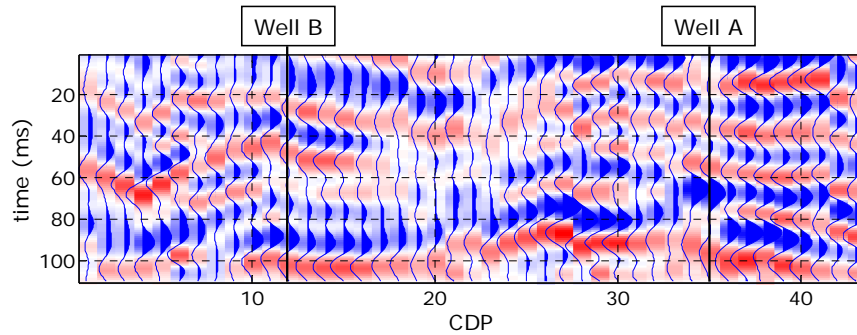


Figure 7.3: 2D near-offset seismic data extracted from the Chevron's seismic volume, showing the locations of the used well.

Based on the available information about the type of depositional environment, the 3D geological model and the well-logs, each depth of each well was classified as one of the three possible groups: sand, overbank, shale. Figure 7.4 shows the logs of the two wells included in the study, color-coded with the assigned group index. The original sampling depth interval of the well-logs was 0.145 meters. It was slightly changed to 0.2 meters by a linear regression between consecutive depth levels, to facilitate the link between the depth-sampling rate of the well-logs and the training image. That small modification in depth sampling did not introduce noticeable changes in the well-logs.

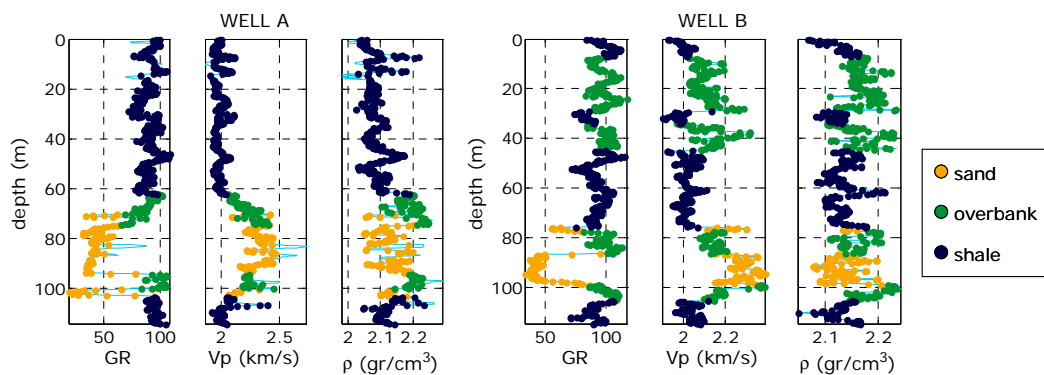


Figure 7.4: Well-logs of the two wells used in the study, color-coded by the group index assigned to each depth level.

7.4 Inversion

Both proposed approaches of the inversion method were used. Before proceeding with the inversion, some decisions were made about how to conciliate the different sampling rates of the input data. The cell size of the simulation or solution grid was defined to be the same as the cell size in the training image, i.e. 100 meters in x and 5.6 meters in z . Obviously, the training image and the solution grid need to have the same sampling interval and the same scale; otherwise, constructing a solution using the training image loses any meaning. In the horizontal direction, the traces of the input 2D seismic section were spaced 100 meters apart; therefore, all data were sampled at the same rate in the x -axis. In the vertical direction, the depth-sampling interval of the input well-logs was 0.2 meters; that is, 28 times smaller than the cell size in z of the solution grid.

The implementation of both inversion approaches uses three grids simultaneously: the simulation grid for the group indices (the solution itself), and one grid for each of the elastic properties (V_p , ρ). The pseudo-wells of group indices to populate the simulation grid are proposed by the geostatistical technique included in the algorithm. The elastic grids are randomly filled, conditioned to the proposed pseudo-wells of group indices; thus a proportionality factor must be computed to define the number of cells of the elastic grids correspond to a single cell of the simulation grid. That factor gives the number of V_p and ρ values to be drawn for every cell in the solution grid. By dividing the depth-sampling interval of the training image by that of the well-logs, a proportionality factor of 28 was obtained. For the case studied, the dimensions of the solution grid were 20 by 43 (z by x). The elastic grids had 560 cells in the vertical direction and 43 cells in the horizontal direction (CPDs).

7.4.1 Pre-processing

The mean, variance and covariance to define the bivariate Gaussian distributions for representing the elastic properties of each group were computed from the well-log data. The obtained values are shown in Table 7.1. Figure 7.5 shows the plot of

the well-log values of P-wave velocity as function of density, color-coded by the assigned group index. For each group, an ellipse computed with mean, variance and covariance of the data points is included. In addition, Figure 7.5 presents a realization of 300 pairs of V_p - ρ drawn from each group. As can be seen, the distribution of points drawn from the defined distributions certainly resembled the original values from the logs. Consequently, in this case, describing the elastic properties of each group with a bivariate Gaussian distribution was a good assumption.

Table 7.1: Parameters to specify the bivariate Gaussian distribution of each group's elastic properties, computed using wells A and B.

<i>group</i>	<i>Mean V_p (km/s)</i>	<i>Variance V_p (km/s)</i>	<i>Mean ρ (gr/cm³)</i>	<i>Variance ρ (gr/cm³)</i>	<i>Covariance</i>
Sand	2.275	8.038	2.129	1.369	0.727
Overbank	2.153	7.335	2.177	1.058	1.615
Shale	2.002	2.392	2.108	1.311	0.971

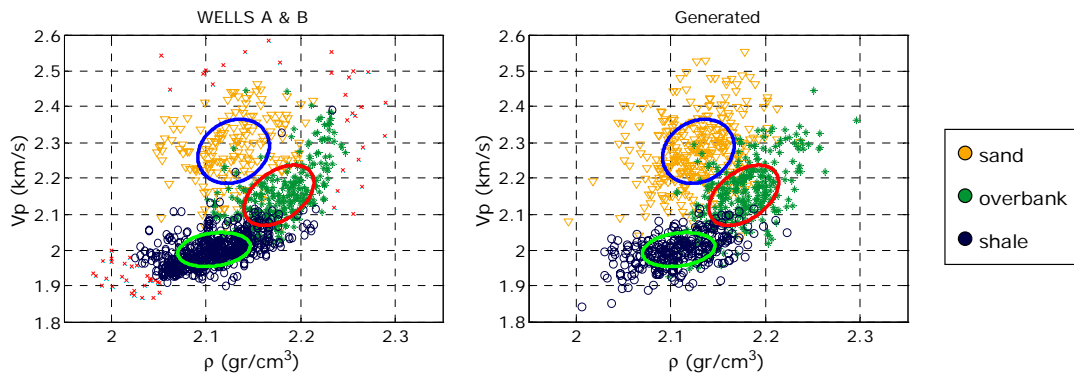


Figure 7.5: V_p - ρ values, color-coded by group index from well logs (left) and drawn (300 points per group) (right) from the bivariate Gaussian with mean, variance, and covariance computed from the well logs and represented by the ellipses.

To perform the forward modeling, a wavelet was needed. In the inversion method, the reflectivity series for the convolution is obtained from the V_p and ρ (impedance) values drawn conditioned to the SIMPAT* simulated pseudo-wells of group indices. The wavelet, which is the other element to convolve, is assumed to be

known (input data for the inversion). Hampson and Russell software was used to extract the wavelet from the seismic data, accounting for the match with both available wells. Figure 7.6 shows the used wavelet in the time and frequency domains. With the dominant frequency of the extracted wavelet (40 Hz), the approximate mean wavelengths for the defined groups, sand, overbank, and shale, were 57, 54, 50 meters, respectively.

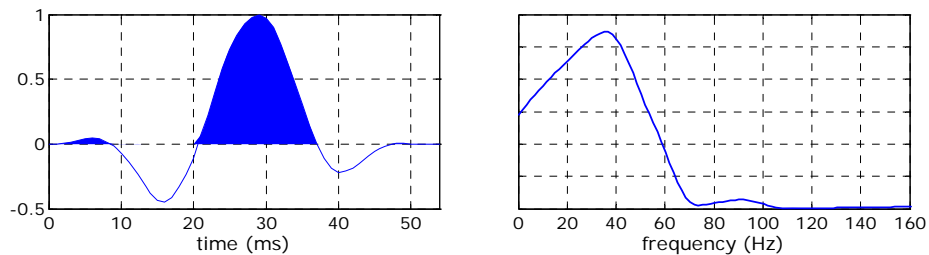


Figure 7.6: Amplitude as function of time (left) and amplitude spectrum (right) of the wavelet extracted from the seismic data and used for the convolution in the inversion.

As was mentioned before, the solution grid had 20 cells in the vertical direction (5.6 meters each cell), and the number of samples of each well-log was 560, with a depth sampling interval of 0.2 meters. Although the elastic properties were simulated at the well-logs' resolution, i.e. 560 samples for each pseudo-well, the group index needed to be at the resolution of the solution grid (20 cells vertically). Therefore, the group-index well logs were upsampled before starting the inversion. The 112 meters sampled by the logs were split in 28 intervals of 5.6 meters each. The group index assigned to each of those intervals was the most repeated in the corresponding range of depths. Figure 7.7 shows the original well logs of group indices and their upsampled versions. Additionally, Figure 7.7 presents the input seismic traces at the well locations, the synthetic seismic traces computed (convolution) with the original V_p and ρ logs, and a set of synthetic traces generated with 30 realizations of pseudo-well elastic properties. Each V_p and ρ pseudo-well was created by drawing 28 values from the bivariate Gaussian distributions of the corresponding group. The good match between the input seismic and the synthetic

traces computed with the well logs validated the wavelet used as well as the tie between the wells and the seismic (time-depth). The good match between the input seismic data and the synthetics generated from the realizations of the V_p and ρ pseudo-wells provided evidence of reproducing the input traces, which was needed to proceed with the inversion.

As part of the pre-processing step, the pattern database was built. The training image was scanned with a 5-by-5 template, at three grid levels. The resulting number of patterns for the first grid level was 11733, with 16044 for the second level, and 6816 for the third level. For each pattern in the database, an *associated pattern* was also retained. As was described when the inversion technique was presented, the solutions are constructed by pasting the associated pattern corresponding to the selected pattern. By definition, all associated patterns had the same number of horizontal cells as the template, and at the first grid level, the patterns and the associated patterns are the same. On the other hand, the numbers of cells in z of the associated patterns for the second and third grid levels were 9 and 17, respectively.

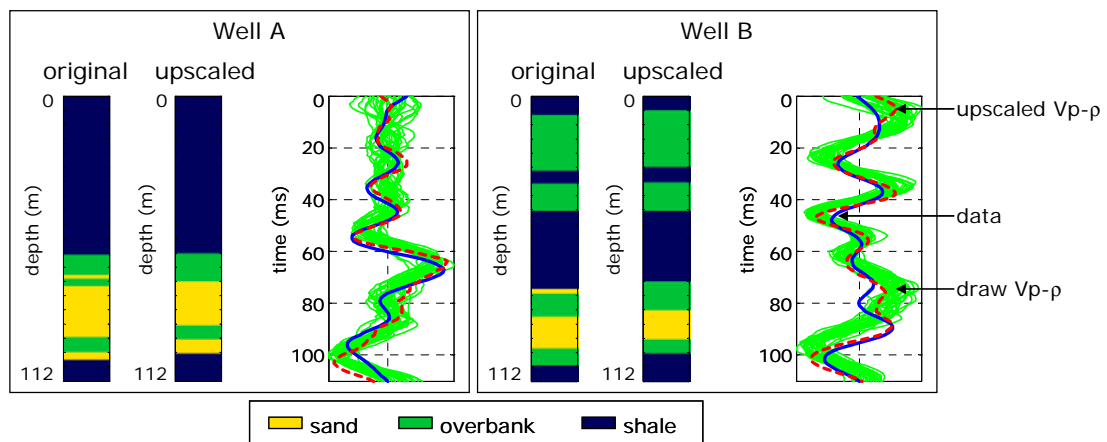


Figure 7.7: For Well A (left) and Well B (right), group-index well logs with the original (0.2 meters) and upscaled (5.6 meters) sampling depth interval, synthetic seismic traces computed from 30 V_p and ρ pseudo-well realizations (green), synthetic trace from original logs (red), and real seismic data trace (blue).

7.4.2 Inversion

The input seismic section was inverted using both approaches of the proposed technique. Table 7.2 presents the values of the input parameters. As can be seen, the number of iterations to be completed for obtaining a solution or realization was defined as seven. That decision was made by analyzing the residuals, in particular the behavior of gL (defined in equation 6) in some tests. The total number of SIMPAT* simulations at every CDP was the same for both approaches. In the compact approach, 96 independent SIMPAT* realizations of pseudo-logs of group indices were generated at every visited CDP. For the extended approach, the number of independent SIMPAT* realizations was 16, with each one updated six times, giving a total of 96.

Table 7.2: Values of the input parameters used for the real seismic data inversion.

<i>Parameter description</i>	<i>Reference name</i>	<i>Value</i>
Grid levels (g+1)	grdlev	[3 2 1]
Template size	(ztsiz, xtsiz)	(5, 5)
Skipped CDP	jumpx	1
Elastic property draws (loop)	elasloop	400
α (for comparison factor)	compval	0.7
SIMPAT* realizations per CDP	simxloc (compact approach)	96
	simxloc (extended approach)	16
Revisit SIMPAT* realizations per CDP (only for extended approach)	simxloc2	6
Iterations to obtain a solution	itersol	7

Ten solutions with each of the proposed inversion's approaches were computed. To illustrate the quality of the input data reproduction, Figure 7.8 presents the input seismic profile, the synthetic seismic data computed with three solutions of the compact approach, and the corresponding residuals. All seismic profiles shown were scaled to the same value to allow visual comparisons. The overall characteristics

(main amplitudes and structure) of the input seismic data were approximately reproduced for the solutions. However, the set of high-amplitude reflections in the last 10 traces (from CDP 38) was not completely recovered. The positions of the reflections were reproduced, but the amplitudes in the solutions tended to be smaller.

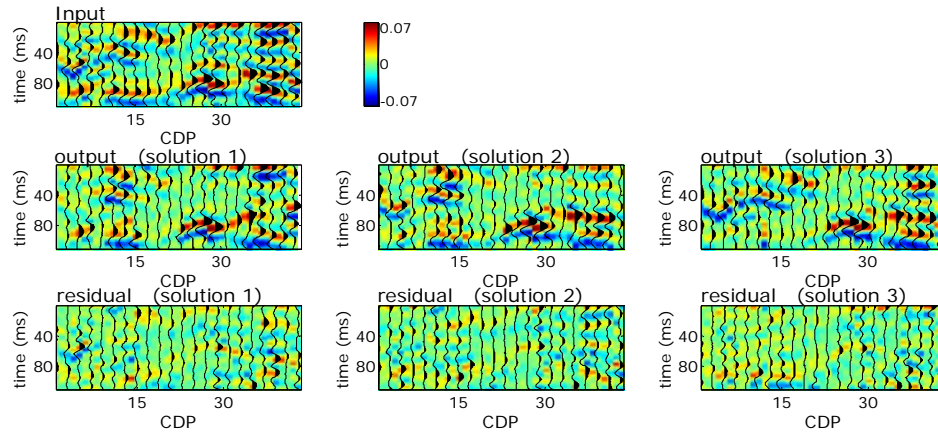


Figure 7.8: Input seismic data (top), output synthetic data (middle row) of three solutions obtained with compact approach, and the residual or difference sample-by-sample between input and output data (bottom row). All plots are scaled to the same value.

Figure 7.9 and Figure 7.10 show four solutions obtained after seven iterations of the proposed compact and extended approaches, respectively. Figure 7.11 presents the probability maps for the three groups computed with 10 solutions of the compact and extended approaches of the proposed inversion technique. In general, the probability maps obtained from both of the approaches were similar. Few zones of the solution grid –basically the ones sampled by the wells– were consistently identified as sand. A lateral extension of the overbank group seen in the wells, especially from Well A, can be identified in the probability map of that group.

To make a quantitative comparison between the results obtained with the two inversion approaches, Figure 7.12 shows the values of the degree of fitting, gL , for all iterations of the 10 solutions. In general, after seven iterations a stable value of gL seemed to be reached in all solutions. As can be noticed, the solutions obtained with the extended approach better reproduced (globally and in l_1 -norm sense) the

input seismic data. This result demonstrated that the implementation of the extended approach satisfies the objective of its creation, which was the search for solutions with small residuals even breaking or combining patterns horizontally, if needed.

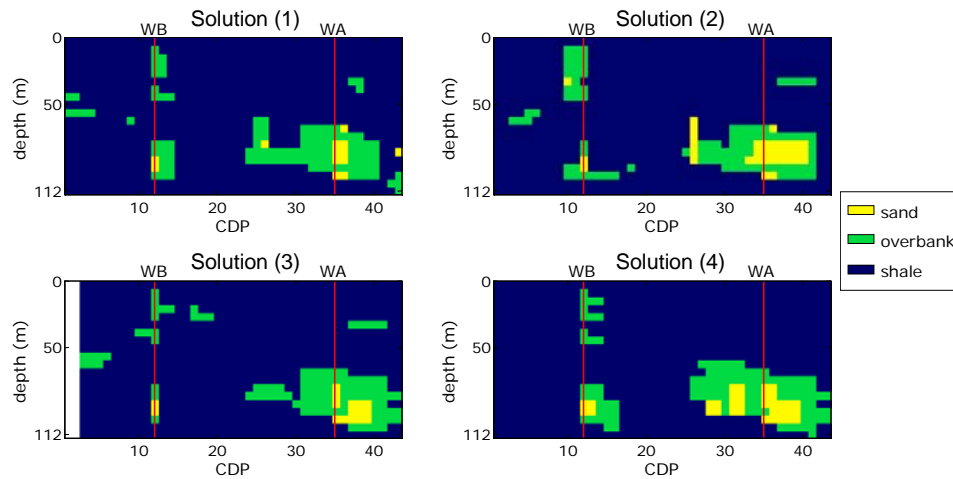


Figure 7.9: Four solutions (seven iterations each one) obtained using the compact approach. Red vertical lines indicate the locations of the wells used as input data (CDP 12 and 35).

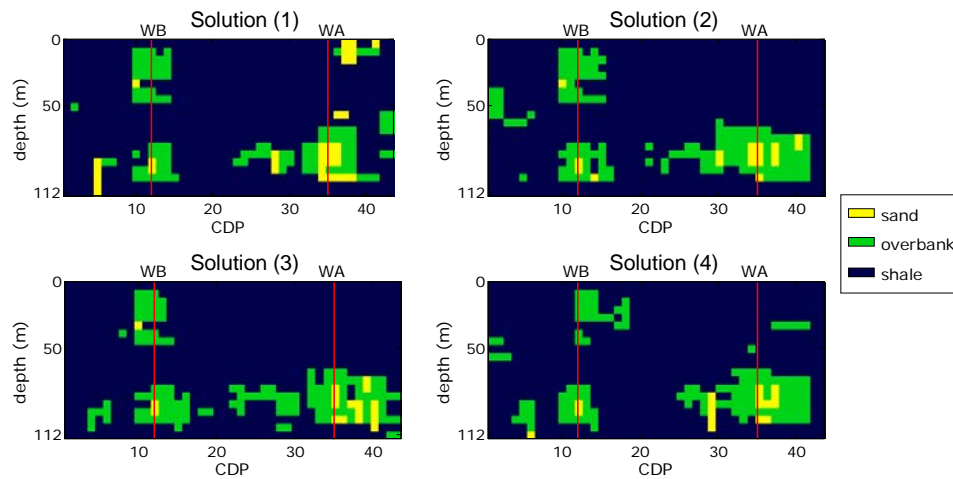


Figure 7.10: Four solutions (seven iterations each one) obtained using the extended approach. Red vertical lines indicate the locations of the wells used as input data (CDP 12 and 35).

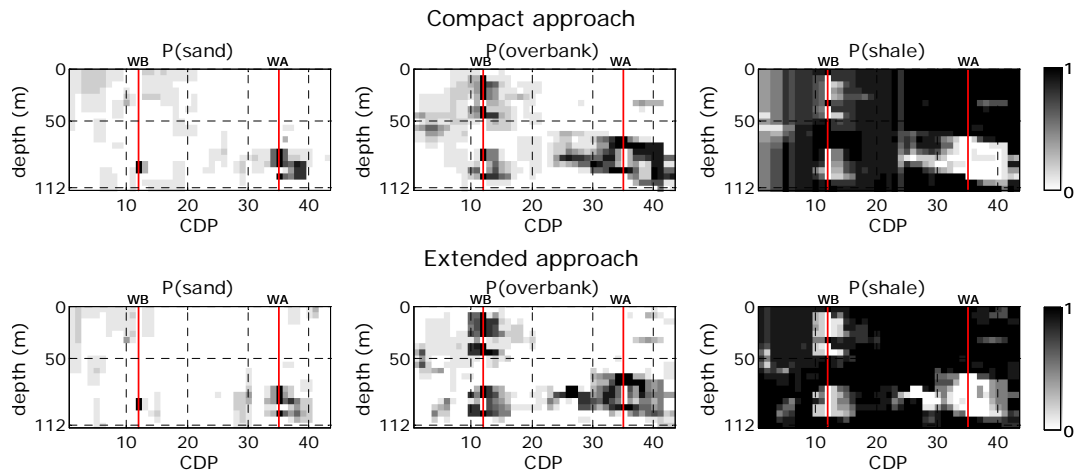


Figure 7.11: Probability map for sand (left), overbank (center), and shale (right) groups computed with 10 realizations of the proposed inversion’s compact (top) and extended (bottom) approaches. Red vertical lines indicate the locations of the wells used as input data (CDP 12 and 35).

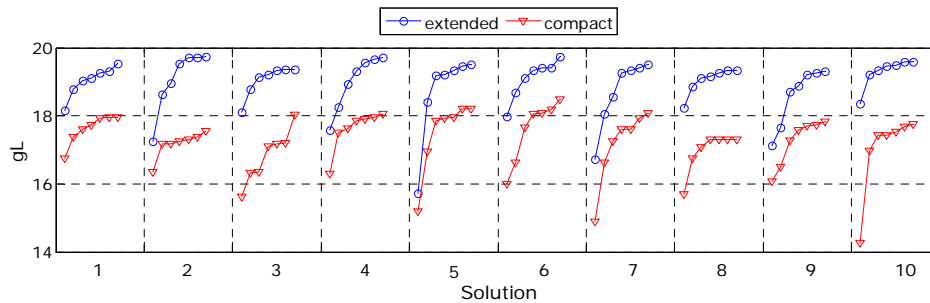


Figure 7.12: Values of the degree-of-fitting parameter, gL , for the seven iterations of the 10 solutions obtained with the proposed inversion’s compact (red triangles) and extended (blue circles) approaches.

7.4.3 Single well inversions

Since only two wells are available, the results of any attempt of cross-validation or “blind” test certainly would not have strong support. Figure 7.3 shows the results of the inversion of the seismic section in that case. The training image and input parameters were the same as previously described. In both cases, 10 solutions (seven iterations each one) of the inversion’s two approaches were computed.

In the first test, Well B was used as the unique input well-log data; consequently, the parameters to define the Gaussian distribution of elastic properties for each group

were computed with V_p and ρ logs of Well B. Figure 7.13 presents the probability maps obtained from the solutions of the two approaches. Comparing with the probability maps using both wells as input data (Figure 7.11), their resemblance can be easily noticed. The main difference was the thickness of the overbank body that crossed the Well A location. The group indices at CDP 35 were extracted from the solutions to be compared with Well A. As Figure 7.14 demonstrates, most of the realizations remarkably predicted the main sand body present in Well A around depths of 70 and 100 meters.

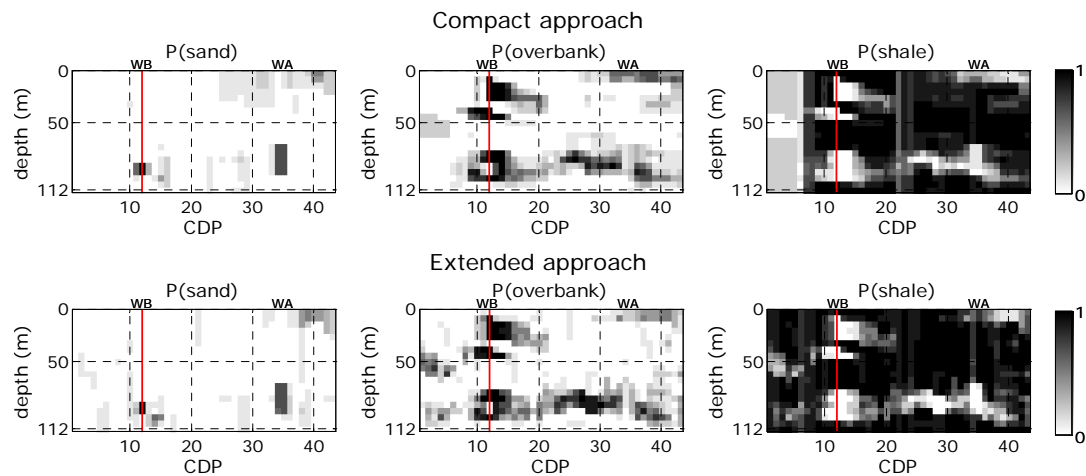


Figure 7.13: Probability map for sand (left), overbank (center), and shale (right) groups computed with 10 realizations of the proposed inversion’s compact (top) and extended (bottom) approaches. Red vertical line indicates the location of Well B (CDP 12), used as input data.

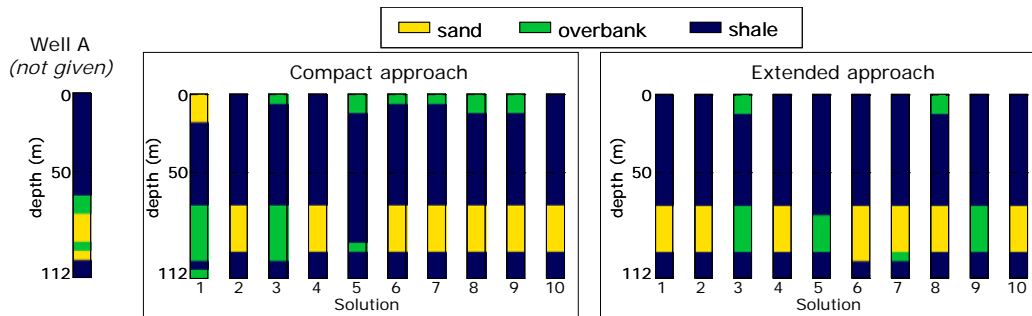


Figure 7.14: Solutions at the Well A location (CDP 35) obtained with the inversion’s compact (left) and extended (right) approaches. Only Well B was used as input data for the inversion.

The second test consisted of inverting the input seismic section, pretending that only the information from Well A was available. Hence, the Gaussian distributions of elastic properties were defined using V_p and ρ logs from Well A. The obtained probability maps are presented in Figure 7.15. In this case, the sand-overbank body in the deepest part of Well A barely extends horizontally from the well location. Moreover, in most of the solutions, that was the only non-shale zone in the whole simulation grid.

The group-indices of the solutions at CDP 12 were compared with Well B. As Figure 7.16 reveals, in the best case the solutions from both inversion approaches predicted a thin (approximately six meters thick) overbank group at the range of depths where a sand-overbank sequence approximately 28 meters thick was present in Well B. In an attempt to explain the causes of the obtained mismatch, the elastic properties of each well were analyzed separately.

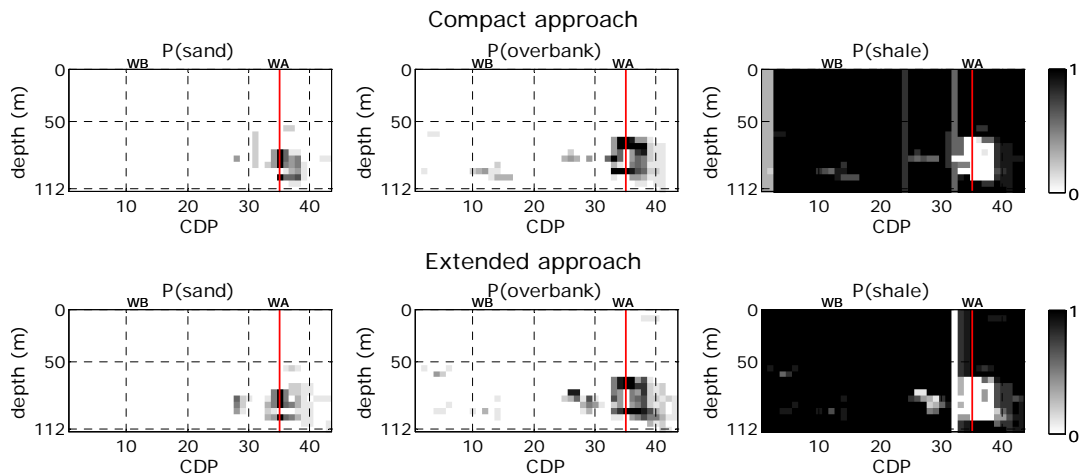


Figure 7.15: Probability map for sand (left), overbank (center), and shale (right) groups computed with 10 realizations of the proposed inversion's compact (top) and extended (bottom) approaches. Red vertical line indicates the location of Well A (CDP 35), used as input data.

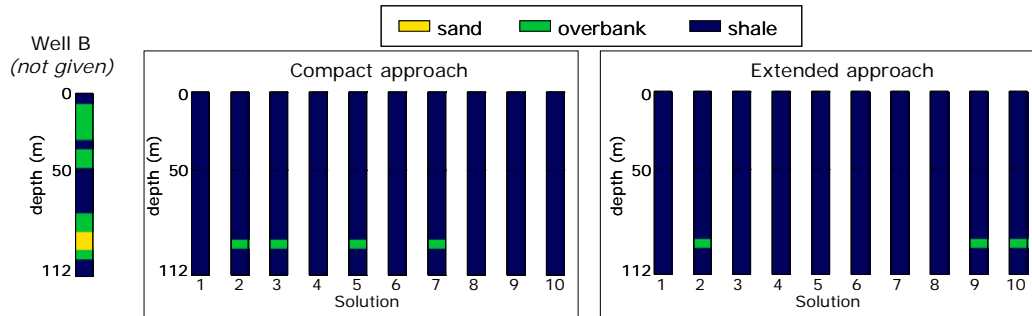


Figure 7.16: Solutions at the Well B location (CDP 12) obtained with the inversion’s compact (left) and extended (right) approaches. Only Well A was used as input data for the inversion.

Figure 7.17 presents the cross-plots between V_p and ρ well-log values, color-coded by the group indices, for Well A and Well B separately. The ellipses included in the plots were defined with the mean, variance and covariance of the Gaussian distributions computed for each group. As can be seen, the sand and shale points in Well A had slightly more dispersion and smaller mean values than in Well B, but overall, they were similar. In contrast, the complete distribution of points of the overbank group observed in Well A appeared to be shifted down (V_p , ρ) in Well B.

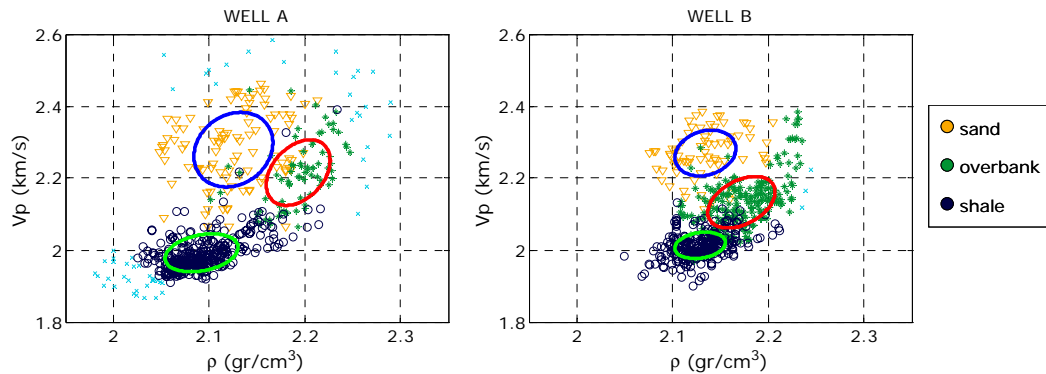


Figure 7.17: V_p - ρ values, color-coded by the group index from Well A (left) and Well B (right). The ellipses were computed with each group mean, variance, and covariance.

For testing the hypothesis that the non-satisfactory results from the inversion with only Well A as input data was mainly caused by the incorrect definition of the elastic property distributions (especially for the overbank group), a new test was

performed. For the new inversion, Well A was used as the unique hard data during the inversion. However, although Well B was not used for constraining the inversion, the mean, variance and covariance of its V_p and ρ logs were used to characterize the elastic properties of each group. The probability maps for each group obtained from the inversion's extended approach are presented in Figure 7.18. As can be seen, in this case the high values in the probability map for the overbank group depicted a shape more consistent with the results obtained when both wells were used as input data.

Figure 7.19 shows the group-indices of the 10 solutions computed with the extended approach at CDP 12, and the Well B group-indices log. Even though the sand around depths of 90 meters was not predicted in any of the solutions, a zone with the overbank group was proposed in most of the realizations. In fact, the solutions at the exact location of Well B must not be taken as the criterion for validating the inversion results. What is more important is to analyze or compare the general trends of the shapes of the geological bodies, which in this case were reasonably consistent whether including both wells, only Well B, or only Well B defining the elastic properties distributions with Well A data.

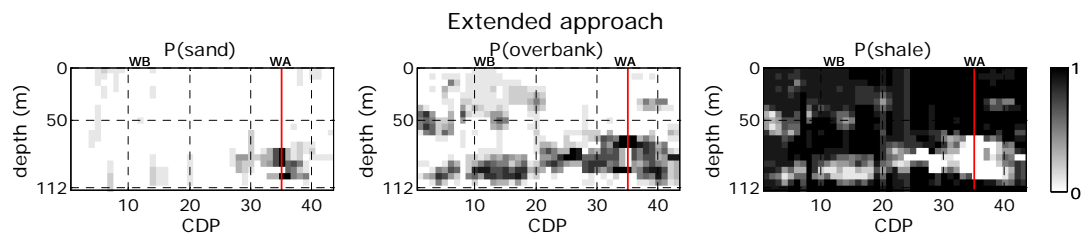


Figure 7.18: Probability map for sand (left), overbank (center), and shale (right) groups computed with 10 realizations of the proposed inversion's extended approach. Red vertical line indicates the location of Well A (CDP 35), used as input data. Mean, variance and covariance to define the elastic properties of each group were computed using Well B information.

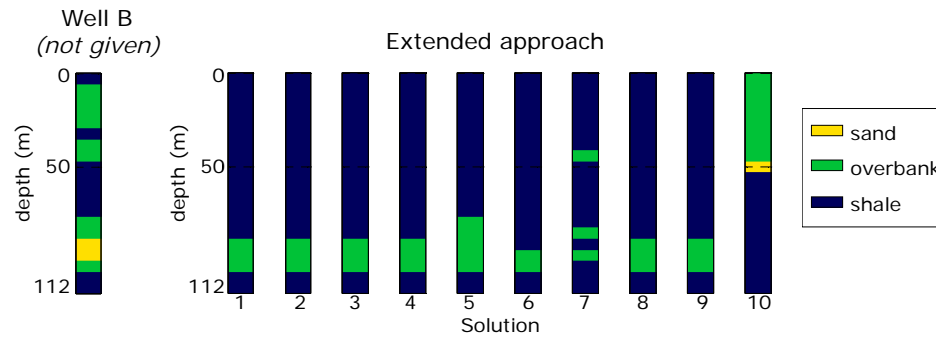


Figure 7.19: Solutions at the Well B location (CDP 12) obtained using Well A as input data for the inversion. Mean, variance and covariance to define the elastic properties of each group were computed using Well B information.

7.5 Conclusions

The applicability of the proposed inversion's compact and extended approaches to real case studies was demonstrated. Moreover, to tackle one common difficulty found when dealing with real data, a practical method to combine information with different sampling intervals in the proposed inversion technique was presented.

Results for the specific real seismic data inverted were presented. Based on the provided geologic information, the training image and the logs of the two wells used, three groups were defined: sand, overbank, and shale. Ten solutions obtained with seven iterations of the proposed inversion's approaches were generated. The probability maps (E-type) for each group were computed with the solutions of the compact and extended approaches of the inversion. The obtained probability from each approach showed similar characteristics. Few sand zones were obtained in the realizations, restricted mainly to the regions sampled for the wells. In the majority of the solutions, the two overbank bodies sampled by Well B were laterally extended about two CDPs from the well; still, the main overbank body shown in the probability maps was located around Well A.

The inversion was also performed using only one well at a time as input data. When Well B was the unique well information given, the probability maps obtained notably resembled the probability maps computed from the solutions using both wells as input data. In particular, the pseudo-logs extracted from the 10 generated

solutions at the CDP corresponding to the Well A location, remarkably reproduced the main sand body observed in Well A. On the other hand, the solutions obtained using only Well A consistently showed basically only shale for the five CDP locations around the well. Analyzing independently the information from each well, a displacement in the elastic properties of the overbank group between wells was detected. This behavior in elastic properties may be due to changes in composition of the overbank sampled at each well. An additional test using Well A for constraining the solutions (groups) but using the distributions of elastic properties defined with V_p and ρ logs of the Well B, was performed. The solutions of that test, particularly in terms of the shape of the main overbank body, resembled the solutions obtained when both wells were used as input data. This final result did not invalidate the solutions obtained using both wells; it only suggests that an additional group might be included.

References

- Arpat, B. G., 2005, Sequential simulation with patterns: Ph.D. dissertation, Stanford Univ.
- Arpat, B. G., and Caers, J., 2004, A multiple-scale, pattern-based approach to sequential simulation: Proceeding to the 2004 International Geostatistics Congress, Banff.
- Arpat, B., Caers, J. and Strebelle, S., 2002, Feature-based geostatistics: an application to a submarine channel reservoir: SPE Annual Conference and Technical Exhibition, San Antonio, SPE# 77426.
- Aki, K., and Richards, P. G., 1980, Quantitative seismology: theory and methods: W. N. Freeman & Co.
- Avseth, P., 2000, Combining rock physics and sedimentology for seismic reservoir characterization in North Sea turbidite systems: Ph.D. dissertation, Stanford Univ.
- Balch, A. H., 1971, Color sonagrams - A new dimension in seismic data interpretation: *Geophysics*, **36**, 1074-1098.
- Banchs, R. and Michelena, R., 2000, Well log estimates and confidence intervals by using artificial neural networks: 70th Ann. Internat. Mtg., Soc. of Expl. Geophys., Expanded Abstracts, 1430-1432.
- Batzle, M. and Wang, Z., 1992, Seismic properties of pore fluids: *Geophysics*, **57**, 1396-1408.
- Berryman, J. G., Berge, P. A., Bonner, B. P., 2002, Estimating rock porosity and fluid saturation using only seismic velocities: *Geophysics*, **67**, 391-404.
- Bortoli, L. J., Alabert, F. A., Haas, A., and Journel, A. G., 1993, Constraining Stochastic Images to Seismic Data, *in* A. Soares ed., *Geostatistics Tróia 1992*, proc. 4th Inter. Geostat. Congr., Kluwer Academic Publ., 325-337.
- Bosch, M., 1999, Lithologic tomography: From plural geophysical data to lithology estimation: *Journal of Geophysical Research*, **104**, 749-766.

- Bosch, M., and McGaughey, J., 2001, Joint inversion of gravity and magnetic data under lithological constraints: *The Leading Edge*, **20**, 877–881.
- Bosch, M., Meza, R., Jiménez, R., and Höning, C., 2005, Geostatistical inversion of gravity and magnetic data in 3D: 75th Ann. Internat. Mtg., Soc. of Expl. Geophys., Expanded Abstracts, 655-658.
- Caers, J., and Zhang, T., 2004, Multiple-point geostatistics: a quantitative vehicle for integration geologic analogs into multiple reservoir models, *in* Integration of outcrop and modern analog data in reservoir models: AAPG memoir 80, 383-394.
- Castagna, J. P., Batzle, M. L., and Eastwood, R. L., 1985, Relationships between compressional-wave and shear-wave velocities in clastic silicate rocks: *Geophysics*, **50**, 571-581.
- Castagna, J. P., Batzle, M. L., and Kan, T. K., 1993, Rock physics – The link between rock properties and AVO response, *in* J. P. Castagna and M. Backus, eds., *Offset-dependent reflectivity – Theory and practice of AVO analysis*: Soc. of Expl. Geophys., 135-171.
- Castro, S., Caers, J., and Mukerji, T., 2005, The Stanford VI reservoir: 18th Annual Report, Stanford Center for Reservoir Forecasting, Stanford University.
- Carbon, J., 2000, Facies architecture of Miocene fluvial-deltaic reservoirs in central Orinoco Belt (Eastern Venezuela basin): M.S. theses, U. Texas at Austin.
- Connolly, P., 1998, Calibration and inversion of non-zero offset seismic: 68th Ann. Internat. Mtg., Soc. of Expl. Geophys., Expanded Abstracts, 182-184.
- Connolly, P., 1999, Elastic impedance: *The Leading Edge*, **18**, 438-452.
- Deutsch C., and Journel, A., 1998, *GSLIB: Geostatistical Software Library*: Oxford University Press, 2nd edition.
- Domenico, S. N., 1976, Effect of brine-gas mixture on velocity in an unconsolidated sand reservoir: *Geophysics*, **41**, 882-894.
- Duffaut, K., Alsos, T., Landro, M., Rogno, H. and Al-Najjar, N. F., 2000, Shear-wave elastic impedance: *The Leading Edge*, **19**, 1222-1229.
- Dvorkin, J. and Gutierrez, M., 2001, Textural sorting effect on elastic velocities, Part II: Elasticity of a bimodal grain mixture: 71st Ann. Internat. Mtg., Soc. of Expl. Geophys., Expanded Abstracts, 1764-1767.
- Engelmark, F., 2000, Using converted shear waves to image reservoirs with low-impedance contrast: *The Leading Edge*, **19**, 600-603.
- Florez, J., 2005, Integrating geology, rock physics, and seismology for reservoir-quality prediction: Ph.D. dissertation, Stanford Univ.
- Goodway, B., Chen, T. and Downton, J., 1997, Improved AVO fluid detection and lithology discrimination using Lamé petrophysical parameters; “ $\lambda\rho$ ”, “ $\mu\rho$ ”, & “ λ/μ fluid stack”, from P and S inversions: 67th Ann. Internat. Mtg., Soc. of Expl. Geophys., Expanded Abstracts, 183-186.

- Gonzalez, E. F., Mukerji, T. and Mavko, G., 2000, Facies identification using P-to-P and P-to-S AVO attributes: 70th Ann. Internat. Mtg., Soc. of Expl. Geophys., Expanded Abstracts, 98-101.
- Gonzalez, E. F., Mukerji, T., Mavko, G. and Michelena, R. J., 2003, Near and far offset P-to-S elastic impedance for discriminating fizz water from commercial gas: *The Leading Edge*, **22**, 1012-1015.
- Gray, D., 2002, Elastic inversion for Lamé parameters: 72th Ann. Internat. Mtg., Soc. of Expl. Geophys., Expanded Abstracts, 213-216.
- Guardiano, F., and Srivastava, R., 1993, Multivariate geostatistics: Beyond bivariate moments, *in* A. Soares ed., *Geostatistics Tróia 1992*, proc. 4th Inter. Geostat. Congr., Kluwer Academic Publ., 133-144.
- Gutierrez, M., 2001, Rock physics and 3-D seismic characterization of reservoir heterogeneities to improve recovery efficiency: Ph.D. dissertation, Stanford Univ.
- Haas, A. and Dubrule, O., 1994, Geostatistical inversion - A sequential method of stochastic reservoir modeling constrained by seismic data: *First Break*, **12**, 561-569.
- Hearst, J. R., Nelson, P. H., Paillet, F. L., 2000, *Well logging for physical properties*: McGraw-Hill, 2nd edition.
- Hirsche, K., Boerner, S., Kalkomey, C. and Gastaldi, C., 1998, Avoiding pitfalls in geostatistical reservoir characterization: A survival guide: *The Leading Edge*, **17**, 493-504.
- Jin, S., Cambois, G. and Vuillermoz, C., 2000, Shear-wave velocity and density estimation from PS-wave AVO analysis: Application to an OBS dataset from the North Sea: *Geophysics*, **65**, 1446-1454.
- Kalkomey, C. T., 1997, Potential risks when using seismic attributes as predictors of reservoir properties: *The Leading Edge*, **16**, 247-251.
- Kelly, M., Skidmore, C. and Cotton, R., 2000, P-P and P-S angle stack inversion: 70th Ann. Internat. Mtg., Soc. of Expl. Geophys., Expanded Abstracts, 222-223.
- Kennett, B., 1980, Seismic waves in a stratified half space – II. Theoretical seismograms: *Geophysical Journal of the Royal Astronomical Society*, **61**, 1-10.
- Kennett, B., 1985, *Seismic wave propagation in stratified media*: Cambridge University Press.
- Landro, M., Duffaut, K. and Rogno, H., 1999, Well calibration of seabed seismic data: 69th Ann. Internat. Mtg., Soc. of Expl. Geophys., Expanded Abstracts, 860-863.
- Larsen, J., Margrave, G. and Lu, H. X., 1999, AVO analysis by simultaneous P-P and P-S weighted stacking applied to 3-C-3-D seismic data: 69th Ann. Internat. Mtg., Soc. of Expl. Geophys., Expanded Abstracts, 721-724.
- Mallick, S., 2001, Hybrid inversion, elastic impedance inversion, and prestack waveform inversion; 71st Ann. Internat. Mtg: Soc. of Expl. Geophys., 706-709.

- Margrave, G. F., Stewart, R. R. and Larsen, J. A., 2001, Joint PP and PS seismic inversion; *The Leading Edge*, **20**, 1048-1052.
- Matteucci, G., 1996, Seismic attribute analysis and calibration: A general procedure and a case study: 66th Ann. Internat. Mtg., Soc. of Expl. Geophys., Expanded Abstracts, 373-376.
- Mavko, G., Chan, C. and Mukerji, T., 1995, Fluid substitution: Estimating changes in Vp without knowing Vs: *Geophysics*, **60**, 1750-1755.
- Mavko, G., Mukerji, T., and Dvorkin, J., 1998, *The rock physics handbook*: Cambridge University Press.
- Michelena, R. J., Donati, M. S., Valenciano, A., and D'Agosto, C., 2001, Using multicomponent seismic for reservoir characterization in Venezuela: *The Leading Edge*, **20**, 1036-1041.
- Mukerji, T., Jørstad, A., Mavko, G., and Granli, J., 1998, Near and far offset impedances: Seismic attributes for identifying lithofacies and pore fluids: *Geophysical Research Letter*, **25**, 4557-4560.
- Mukerji, T., Avseth, P., Mavko, G., Takahashi, I., and Gonzalez, E. F., 2001, Statistical rock physics: Combining rock physics, information theory, and geostatistics to reduce uncertainty in seismic reservoir characterization: *The Leading Edge*, **20**, 313-319.
- Oldenburg, D. W., Scheuer, T., and Levy, S., 1983, Recovery of the acoustic impedance from reflection seismograms: *Geophysics*, **48**, 1318-1337.
- Possato, S., Saito, M., Curtis, M. P., and Martinez, R. D., 1983, Interpretation of three-dimensional seismic attributes contributes to stratigraphic analysis of Pampo oil field: 53rd Ann. Internat. Mtg., Soc. of Expl. Geophys., Expanded Abstracts, session: S16.2.
- Ramos, A. C. B., and Castagna, J. P., 2001, Useful approximations for converted-wave AVO: *Geophysics*, **66**, 1721-1734.
- Ronen, S., Hoskins, J., Schultz, P. S., Hattori, M., and Corbett, C., 1994, Seismic-guided estimation of log properties, part 2: Using artificial neural networks for nonlinear attribute calibration: *The Leading Edge*, **13**, 674-678.
- Russell, B. H., 1988, Introduction to seismic inversion methods: Soc. of Expl. Geophys. Course notes from SEG Continuing Education course.
- Stewart, R. R., Gaiser, J. E., Brown, R. J., and Lawton, D. C., 2003, Converted-wave seismic exploration: Applications: *Geophysics*, **68**, 40-57.
- Strebelle, S., 2000, Sequential Simulation Drawing Structures from Training Images: Ph.D. dissertation, Stanford Univ.
- Taner, M. T., 2001, Seismic attributes: *Recorder*, **26**, 48-56.
- Taner, M. T., Koehler, F., and Sheriff, R. E., 1979, Complex seismic trace analysis: *Geophysics*, **44**, 1041-1063.

- Takahashi, I., 2000, Quantifying information and uncertainty of rock property estimation from seismic data: Ph.D. dissertation, Stanford Univ.
- Tarantola, A., 2005, Inverse problem theory and methods for model parameter estimation: Society for Industrial and Applied Mathematics.
- Tonn, R., 1992, Statistical approach to correlate reservoir parameters and 3-D seismic attributes, 62nd Ann. Internat. Mtg., Soc. of Expl. Geophys., Expanded Abstracts, 272-274.
- Tran, T., 1994, Improving variogram reproduction on dense simulation grids: Computers and Geosciences, **20**, 1161-1168.
- Valenciano, A., and Michelena, R., 2000, Stratigraphic inversion of poststack P-S converted waves data: 70th Ann. Internat. Mtg., Soc. of Expl. Geophys., Expanded Abstracts, 150-153.
- Veire, H., and Landro, M., 2001, Joint inversion of PP- and PS-seismic data: 71st Ann. Internat. Mtg., Soc. of Expl. Geophys., Expanded Abstracts, 861-864.
- Wu, Y., 2000, Estimation of gas saturation using P-to-S converted waves; 70th Ann. Internat. Mtg., Soc. of Expl. Geophys., Expanded Abstracts, 158-161.
- Zhang, T., 2006, Multiple point geostatistics: Filter-based local training pattern classification for spatial pattern simulation: Ph.D. dissertation, Stanford Univ.
- Zhu, F., Gibson, R. L., Atkins, J., and Yuh, S. H., 2000, Distinguishing fizz gas from commercial gas reservoirs using multicomponent seismic data: The Leading Edge, **19**, 1238-1245.